# Thin film flows in curved tubes




Nawinda Chutsagulprom
Linacre College
University of Oxford

A thesis submitted for the degree of
*Master of Science*
Michaelmas 2010

## Acknowledgements

I would like to thank my supervisor, Dr. Sarah Waters and Dr. James Oliver, for their help, support, and most of all, their patience. I would also like to thank all occupants of DH9 and DH10 for helpful discussions. I also gratefully acknowledge the financial support of the Thai Royal Government.

# Abstract

The main motivation of this thesis comes from a desire to understand the behaviours of blood flow in the vicinity of atheroma. The initiation and development of atherosclerosis in arteries are normally observed in the areas of low or oscillating wall shear stress, such as on the outer wall of a bifurcation and the inside of the bends.

We start by building on the background to the areas related to our models. We focus on the models of fluid flow travelling through a curved tube of uniform curvature because most arteries are tapered and curved. The flow of an incompressible Newtonian fluid in a curved tube is modelled. The derivation of the corresponding equations of the motion is presented. The equations are then solved for a steady and oscillatory driving axial pressure gradient. In each case, the flow is governed by different dimensionless parameters. The problem is solved for a variety of parameter regimes by using asymptotic technique as well as numerical method.

Some aspects of thin-film flows are studied. The well-known thin film equation is derived using lubrication theory. The stability of a thin film in a straight tube and the effects of a surfactant droplet on a liquid film are presented. The moving contact line problem, one of the controversial topics in fluid dynamics, is also discussed.

The leading-order equations governing thin-film flow over a stationary curved substrate is derived. Various approaches and the application of flow on particular substrates are shown.

Finally, we model two-layer viscous fluids using lubrication approximation. By assuming the thickness of a lower liquid layer is much thinner than that of the upper liquid layer, the equation governing the liquid-liquid interface is derived. The steady-state and trasient solutions of the evolution equation is computed both analytically and computationally.

# Contents


**1 Introduction** **1**
1.1 Introduction . . . 1
1.2 The Cardiovascular system . . . 2
1.2.1 The heart . . . 2
1.2.2 The blood vessels . . . 4
1.3 Arteries . . . 4
1.3.1 Cellular components . . . 5
1.3.1.1 Endothelial cells . . . 5
1.3.1.2 Smooth muscle cells . . . 6
1.3.2 Arterial structure . . . 6
1.3.2.1 Tunica intima . . . 6
1.3.2.2 Tunica media . . . 6
1.3.2.3 Tunica adventitia . . . 7
1.3.3 Mechanical forces . . . 7
1.3.3.1 Pressure, circumferential tension and stress . . . 8
1.3.3.2 Wall shear stress and blood flow . . . 8
1.3.3.3 Hemodynamics . . . 9
1.4 Atherosclerosis . . . 10
1.4.1 Development of atherosclerosis . . . 10
1.4.1.1 Early stage . . . 10
1.4.1.2 Late stage . . . 11
1.4.2 Remodelling . . . 12
1.4.3 Plaque rupture . . . 13
1.4.4 Thrombosis . . . 14
1.4.5 Treatment . . . 14
1.5 Thesis outline . . . 15

**2 Flows in curved tubes** **17**
2.1 Introduction . . . 17
2.2 Governing equations and parameters . . . 19
2.2.1 Parameter descriptions . . . 21
2.3 Fully developed steady flow in a weakly curved tube . . . 23
2.3.1 Small $D$ . . . 23
2.3.2 Intermediate $D$ . . . 25
2.3.3 Large $D$ . . . 26
2.4 Fully developed unsteady flow in a weakly curved tube . . . 30
2.4.1 Purely oscillatory flows: sinusoidal flows . . . 30

2.4.1.1 Low-frequency pressure gradient ( $\alpha \ll 1$ ) . . . . . 31
2.4.1.2 High-frequency pressure gradient ($\alpha \gg 1$) . . . . . 32
2.4.2 Oscillatory flows with non-zero mean pressure gradient: oscillatory flows . . . . . 36
2.5 Conclusion . . . . . 40

**3 Thin-film flows** **44**
3.1 Derivation of thin liquid film equation . . . . . 44
3.1.1 Nondimensionalisation and scaling . . . . . 46
3.2 Thin film stability . . . . . 47
3.2.1 Thin film stability . . . . . 47
3.2.2 Thin film stability in an axisymmetric elastic tube . . . . . 50
3.2.3 Two thin liquid films . . . . . 51
3.3 The Marangoni effect . . . . . 51
3.4 Moving contact line . . . . . 57
3.4.1 Navier slip condition . . . . . 58
3.4.2 Precursor film . . . . . 58
3.5 Conclusion . . . . . 59

**4 Thin liquid film on curved substrates** **60**
4.1 Introduction . . . . . 60
4.2 Derivation of the master thin-film equation . . . . . 60
4.2.1 Governing equations and boundary conditions . . . . . 62
4.2.2 Nondimensionalization and scaling . . . . . 63
4.2.3 Substrate curvature . . . . . 66
4.2.3.1 Small curvature . . . . . 66
4.2.3.2 Nearly constant curvature . . . . . 66
4.2.3.3 Large curvature . . . . . 66
4.3 Examples of film flows on curved substrates . . . . . 67
4.4 Conclusion . . . . . 70

**5 A two-layer viscous fluids model** **71**
5.1 Two thin-film flows models . . . . . 71
5.1.1 Introduction to the problem . . . . . 71
5.1.2 The governing equations and the boundary conditions . . . . . 72
5.1.3 Nondimensionalisation and scaling . . . . . 73
5.1.4 Derivation of averaged equations . . . . . 74
5.1.5 The evolution equation governing the fluid behaviours at the interface 76
5.2 Linear stability analysis . . . . . 77
5.3 Numerical schemes . . . . . 78
5.3.1 Transient solutions . . . . . 78
5.3.2 Steady state solutions . . . . . 80
5.3.3 Numerical results . . . . . 81
5.4 Conclusion . . . . . 86

**6 Conclusions and Future work** **89**
6.1 Summary and discussion . . . . . 89
6.2 Further work . . . . . 92

**A MATLAB code for the two-layer thin-film model in Chapter 5.** **94**

**B MATLAB code for the inviscid Burgers equation.** **99**

**C MATLAB code for the steady-state solutions in Chapter 5.** **102**

**Bibliography** **104**

# List of Figures


1.1 The heart consisting of four chambers: right atria, right ventricle, left atria and left ventricle (*http://www.phaaustralia.com.au/content/what-pulmonary-arterial-hypertension*). . . . . 3
1.2 Anatomy of the aorta *http://www.daviddarling.info/encyclopedia/A/aorta.html* 5
1.3 Anatomy of arterial wall (Holzapfel & Ogden, 2003). . . . . 7
1.4 Pressure, tension and stress in arterial wall. . . . . 8
1.5 Diagram showing atherosclerotic plaque (*http://www.riversideonline.com*). . 11
1.6 Diagram showing the atheroma plaque (*http://medinfo.ufl.edu*). . . . . 12
1.7 Diagram showing the negative and positive remodelling. . . . . 13

2.1 Diagram showing the the primary and secondary flows in the curved tube. O, and I denote outer and inner of the bend respectively. . . . . 18
2.2 Streamlines of multiple steady state solutions for $D = 5000$; (a) Two-vortex solution, (b) four-vortex solution. Reproduce from (Yanase et al., 1989). . . 18
2.3 The curvilinear co-ordinate system. . . . . 19
2.4 The sketch of axial velocity contours and secondary flow streamlines for small $D$ (a) $w_0$, (b) $\psi_0$, (c) $w_1$. . . . . 24
2.5 This diagram showing the streamlines (dashed lines) and the contours of constant axial velocity component (solid lines): (a) D=96, $w_m$=23.4, $\psi_m = 0.95$, (b) D=303.58, $w_m = 60, \psi_m = 3.83$,(c) D=605.72, $w_m = 98.5, \psi_m = 6.81$ where $w_m$ and $\psi_m$ are the maximum axial velocity and streamline function respectively. O and I denote the outer and inner of the bend respectively. Reproduced from McConalogue & Srivastava (1968). . . . . 26
2.6 The plot of the flux ratio $Q_c/Q_s$ against $D$, the dotted line satisfies the Dean's series up to $D = 96$, and the continuous line satisfies equation $Q_c/Q_s = 16D^{-1}\int_0^1 rw_0\,dr$. Reproduced from McConalogue & Srivastava (1968). . . . 27
2.7 Bifurcation diagram for various Dean number. The continuous line represents the stable solutions, and the dot-dashed line represents unstable solutions. The first turning point is when $D = 956$, and the second turning point is when $D = 2494$. Reproduced from Daskopoulos & Lenhoff (1989). . . . . 30
2.8 The diagram showing the time evolution of the secondary streamlines of the perturbed four-vortex solution at $D = 1000$. Reproduced from Yanase et al. (1989). . . . . 31
2.9 The diagram showing the secondary core flow at large $\alpha$, small $R_s$ . . . . . 35
2.10 Sketch of the flow for large $\alpha$, and large $R_s$. . . . . 36

2.11 Sketch of three distinct classes of stable solutions and unstable solution branches are not presented when $\delta$ is greater than 0.7 (the critical value). The vertical axis (not to scale) denotes the value of a solution property on a Poincaré section at time intervals of $2\pi$. Reproduced from Siggers & Waters (2008). . . . . 36
2.12 The streamlines (above) and the axial velocity contours (below) for $R_s = 300$, $\alpha = 20$ at time $t = 0, \pi/3, 2\pi/3$. The solid curves represent the solutions for $\delta = 0$, and dotted curves for $\delta = 0.3$. Reproduced from (Siggers & Waters, 2008). . . . . 37
2.13 Plots of secondary streamlines (left) and axial velocity contours (right) of the fluid flow driven by the oscillatory pressure gradient in which the steady component of the pressure gradient $D$ is much smaller than the secondary streaming Reynolds number $R_s$; (a) $R_s = 10$, (b) $R_s = 150$ and (c) $R_s = 1800$. I and O denote the inside and outside of the bend respectively. Reproduced from Blennerhassett (1976). . . . . 39
2.14 Illustration of secondary streamlines (left) and axial velocity contours (right) of the oscillatory flow. Here, (a) $D = 40$, (b) $D = 160$ for $R_s = 30$. I and O denote the inside and outside of the bend respectively. Reproduced from Blennerhassett (1976). . . . . 40
2.15 The S-shaped portion of the plot between of the flow rate ratio and $D$ at fixed $R_s = 100$ . . . . . 40
2.16 Illustration of secondary streamlines (left) and axial velocity contours (right) of the oscillatory flow. I and O denote the inside and outside of the bend respectively. (a) lower branch, (b) middle branch and (c) upper branch show the contours of streamline function and axial velocity on the S-shaped portion of the curve at fixed $R_s = 100, D = 244$. Reproduced from Blennerhassett (1976). . . . . 41
2.17 Illustration of secondary streamlines (above) and axial velocity contours (below) of the oscillatory flow for $D = 0, R_s = 50, \alpha = 10$. Solid lines, $\gamma = 0$; dotted lines, $\gamma = 0.1$; dashed lines, $\gamma = 0.3$ I and O denote the inside and outside of the bend respectively. Reproduced from Siggers & Waters (2008). 42
2.18 Illustration of secondary streamlines (above) and axial velocity contours (below) of the oscillatory flow for $D = 5000, R_s = 50, \alpha = 10$. Solid lines, $\gamma = 0$; dotted lines, $\gamma = 0.1$; dashed lines, $\gamma = 0.3$ I and O denote the inside and outside of the bend respectively. Reproduced from Siggers & Waters (2008). 42

3.1 Schematic of a thin fluid film on the inclined substrate. . . . . 45
3.2 Thin film lining on a cylindrical tube. . . . . 48
3.3 Liquid droplets on spider's web *http://www.serenejourney.com/2009/09/have-a-look-at-what-youve-been-missing*. . . . . 49
3.4 Diagram showing how a liquid bridge is formed . . . . . 50
3.5 Tears of wine *http://wine-scamp.com/2007/09/05/quit-staring-at-my-legs*. . 52
3.6 Schematic illustrations of surfactant. . . . . 53
3.7 Diagram of two-dimensional surfactant droplet on a thin film layer above a rigid wall. . . . . 53

3.8 (a) Film thickness and (b) surfactant concentration profiles along the radial distance for ◯ $Pe$=0.5; △ $Pe$=1.0; □ $Pe$=10; ▽ $Pe$=100. The Bond number is held at constant at 0 at time $t = 0.5$. Reproduced from Gaver & Grotberg (1990). . . . . 54
3.9 Diagram showing the film thickness and surfactant concentration profiles for ◯ $B$=0.1; △ $B$=1; □ $B$=10. $Pe$=100 at time $t = 0.5$. . . . . 55
3.10 Streamlines of a velocity field (a) $t = 0.5$; (b) $t = 0.75$; (c) $t = 3.0$ for $Pe$=10.0, $B$=1.0. Reproduced from Gaver & Grotberg (1990). . . . . 56
3.11 Streamlines showing the effects of soluble surfactant, without the gravitational effects, at (a) $t = 200$ and (b) $t = 1000$. Reproduced from Halpern & Grotberg (1992a). . . . . 57
3.12 Diagram showing the precursor film advancing ahead of the fluid drop where $\theta$ is the apparent contact angle of the drop. . . . . 59

4.1 Schematic of a thin-liquid film over a stationary curved substrate. . . . . 61
4.2 A coating flow on an outside of a corner at time 300 s. Reproduced from Schwartz & Weidner (1995). . . . . 67
4.3 Schematic of a thin film evolution when the surface curvature is large. . . . 68
4.4 Torus sketch . . . . . 68
4.5 Evolution of thin flow on the outside of a torus for later time. $I$ and $O$ denote the inner and outer rim of the torus respectively. . . . . 69
4.6 Schematic of a thin-liquid film (dashed line) flowing inside the curved tube where I and O denote the inside and outside of the bend respectively. Reproduced from Jensen (1997). . . . . 70
4.7 Liquid forming a rivulet with zero contact angle. I and O denote the inside and outside of the bend respectively. . . . . 70

5.1 Sketch illustrating the two thin-film flows in the channel $0 < y < H$. . . . . 72
5.2 Schematic presentation of disturbance applied at the liquid-liquid interface. 78
5.3 Diagram showing the finite-diffence scheme of the film evolution equations . 79
5.4 The effects of the oscillation speed when the forcing is $M(t) = B\sin(\pi t)$, where (a) $B = 1$ (b) $B = 10$, where $\Gamma = 1$ and $h(x, 0) = 1 + 0.1\sin(\pi x)$ are held fixed. The colour strip denotes the interfacial height. The colour strip represents the height of the fluid-fluid interface. . . . . 82
5.5 The fluid-fluid interface profile when the oscillatory forcing is $M(t) = 100\sin(\pi t)$ at $t = 0$ , 0.12, 0.24, where (a) $\Gamma = 1$, (b) $\Gamma = 5$. . . . . 83
5.6 The fluid-fluid interface when the oscillatory forcing is (a) $M(t) = 100\sin(\pi t/5)$, and (b) $M(t) = 100\sin(\pi t/20)$ $\Gamma = 1$ and $h(x, 0) = 1 + 0.01\sin(\pi x)$. The colour strip represents the height of the fluid-fluid interface. . . . . 84
5.7 The interfacial profile, the progression of the transient solution towards the solution of the steady-state equation when $\Gamma = 1$ with $M = 10$ and the initial condition $h(x, 0) = 1 + 0.1\sin(\pi x)$. . . . . 85
5.8 Steady-state solutions for a film under the surface tension $\Gamma = 1$ and different values of shear stress forcing $M$, with $m = 1.065$ and $h(x, 0) = 1 + 0.1\sin(\pi x)$. 85
5.9 Steady-state solutions for a film under the surface tension $\Gamma = 1$, $M = 120$ with $m = 1.065$ and $h(x, 0) = 1 + 0.1\sin(\pi x)$. . . . . 86

5.10 The effect of the initial condition $h_0 = 1 + a\sin(\pi t)$ when (a) $a = 0.1$ (b) $a = 1$ at time $t = 0$ (red line), $3\pi/10$ (yellow line), $3\pi/5$ (green line), $\pi$ (blue line). $\Gamma = 1$ and $M(t) = 10\sin(\pi t)$. . . . . 87
5.11 The burgers equation. . . . . 88

6.1 The geometry of a plaque in a stright rigid vessel. . . . . 92

# Chapter 1

# Introduction

## 1.1 Introduction

Coronary heart disease (CHD) is a major cause of mortality. Myocardial infarction (heart attack) and angina (chest pain) are examples of coronary heart disease. In UK, coronary heart disease is the biggest killer: one in four men and one in six women die from the disease. Approximately 300,000 people have a heart attack each year (NHS, 2009).

Coronary heart disease, stroke and related diseases are precipitated by atherosclerosis. Atherosclerosis is a progressive disease in which cholesterol, lipids, white blood cells and other substances infiltrate the arterial wall leading to a narrower and stiffer arterial wall that restricts the blood flow. Ultimately atherosclerosis can result in occlusion of a vessel. Consequently, the loss of oxygen supply in the downstream blood flow can trigger a heart attack or stroke.

The causes of atherosclerosis are mainly dietary imbalances with high-fat content, lack of exercise, smoking and genetic heredity. These factors may damage the endothelial cells lining the intima layer of the arterial vessels. The injury to the endothelial cells results in an alteration in endothelial cell reactivity including an increase in endothelial permeability to lipoproteins and other constituents. This causes in a deposition of fats, cholesterol, waste products and other substances. This buildup is called a *plaque*. Once a plaque has formed, it may stimulate the arterial wall to generate growth factors and cytokines that promote an accumulation of lipid and support endothelial dysfunction. The final event in atherosclerosis is *thrombosis* in which the plaque ruptures and causes the clotting of blood within a blood vessel.

The purpose of this thesis is to model the blood flow in an artery with a fatty plaque attached on the arterial wall. It is found that the distribution of wall shear stress in arteries is crucially important in the analysis of atherosclerosis (Caro et al., 1971).

We discuss the biological background in this introductory chapter. In §1.2, an overall view of the cardiovascular system is given. In §1.3, we review the salient features of the arteries (in which atherosclerosis develops); structure and functions of arterial vessels. The development and treatment of atherosclerosis are described in §1.4. In §1.5, the thesis outline is presented.

## 1.2 The Cardiovascular system

The cardiovascular system is responsible for supplying oxygen to cells in the body as well as removing carbon dioxide and waste products. The major components of the cardiovascular system are the heart, blood and blood vessels. The heart pumps oxygen-rich blood through the network of blood vessels. Once blood reaches the tissues, the interchange between oxygen and carbon dioxide occurs. The blood subsequently travels back to the heart.

### 1.2.1 The heart

The heart consists of four chambers that are arranged in pairs: in the upper heart the chambers are called *atria*, and in the lower heart the chambers are called *ventricles*, as shown in Figure 1.1.

The right atrium receives blood from the superior vena cava and blood flows through a non-return valve to the right ventricle. The right ventricle then pumps the blood to the lungs. The blood within the lungs is oxygenated and returns to the left atrium via the pulmonary vein. The blood from the left atrium is pumped into the left ventricle, and oxygenated blood is then delivered to every part of the body via a network of vessels (the structure of main blood vessels are given in §1.2.3 ).

The valves in the heart permit blood to flow in a one-way direction between the chambers. Between the left atrium and the left ventricle the non-return valve is called the *mitral valve*, and between the right atrium and the right ventricle, the non-return valve is called the *tricuspid valve*. The opening and closing processes of the valves are controlled by the pressure difference across the valves. The direction of blood circulation in the heart is shown in Figure 1.1.

The cardiac cycle is the series of electrical and mechanical events that occur concurrently. The mechanical events–contraction, relaxation, and the resultant changes in blood flows–are initiated by the electrical events (Brown et al., 2006). Here, we describe the events on the left side of the heart only because similar events also occur on the right side of the heart. The cardiac cycle is initiated by the nervous tissue in the wall of the atrium called *sino-atrial node* (SA node). An electrical impulse spreads through the atria resulting in atrial contraction.

Due to the continuous blood flow from the pulmonary vein into the atrium, atrial pressure is slightly higher than ventricular pressure. Because of this pressure difference, the extra quantity of blood is forced to move slowly from the atrium to the ventricle through the mitral valve. When the SA node reaches threshold and fires, the atrium squeezes more blood into the ventricle.

When the ventricular pressure exceeds the atrial pressure, the mitral valve closes and the ventricular pressure continues to increase until it exceeds the aortic pressure. There is a brief period when the left ventricle is a closed chamber, all of its valves being closed ( *isovolumetric ventricular contraction* ). During isovolumetric ventricular contraction, the ventricular pressure continues to increases due to contraction, whereas the volume remains constant.

When the pressure in the ventricle exceeds the aortic pressure, the aortic valve is forced open and the ejection of blood begins. The amount of blood pumped out of each ventricle with each contraction is called the *stroke volume*. The ventricular volume decreases substantially as blood is rapidly pumped. The systole stage includes both the period of isovolumetric contraction and the ventricular ejection phase.

When the aortic valve closes the mitral valve is not yet open, because ventricular pressure exceeds atrial pressure, so no blood can enter the ventricle from the atrium. All valves are then closed again for a brief period known as *isovolumetric ventricular relaxation*.

When the ventricular pressure is less than the atrial pressure, the mitral valve opens and ventricular filling begins again. Thus, ventricular diastole includes both the period of isovolumetric ventricular relaxation and the ventricular filling phase.

At the same time as the ventricle is relaxing, the pressure in the left atrium is rising as blood continues to flow from the pulmonary veins. When the pressure in the atrium exceeds that of the ventricle the mitral valve reopens and ventricular filling begins again (Sherwood, 2003).

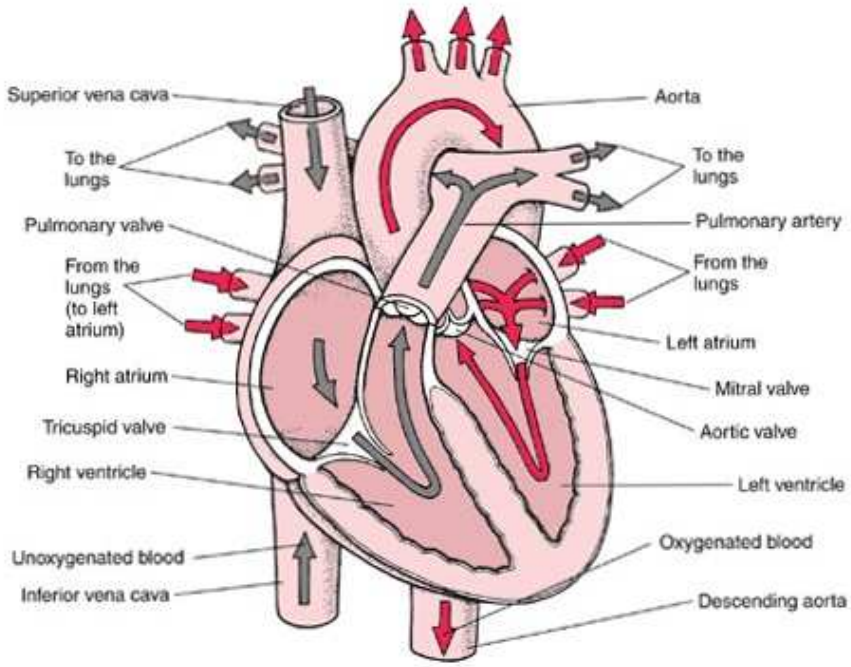



Figure 1.1: The heart consisting of four chambers: right atria, right ventricle, left atria and left ventricle (*http://www.phaaustralia.com.au/content/what-pulmonary-arterial-hypertension*).

The average adult has between 5-6 litres of blood. The blood circulates through a network of blood vessels to provide oxygen and nutrients to the cells in the human body, and helps in eliminating waste products from metabolism. About 45% of blood consists of red cells, white cells and platelets. The rest is fluid called *plasma* and consists of water and dissolved substrates.

There are three main types of blood cells:

- **Erythrocytes** (red cells) are disc shaped cells without cell nuclei in order to provide the maximum space for haemoglobin which is essential in oxygen-carbon dioxide exchange. They are formed in the bone marrow. They are the largest population of blood cells and there are 4.5-6 million per cubic millimeter of blood. The life span of red cells is around 120 days, and they are destroyed by phagocytic cells when they enter the spleen, liver and bone marrow via capillaries (Premkumar, 2003).
- **Leukocytes** (white cells) have a rather short life lasting from days to a few weeks.

The main function of leukocytes is to defend the body from foreign materials, for example, bacteria and various pathogens. They are classed as granular or agranular depending on whether or not they contain granules. There are three types for each: granulocytes (neutrophils, eosinophils and basophils), and agranulocytes (monocytes, T-cell lymphocytes, and B-cell lymphocytes). The granulocytes contain substances that produce allergic and inflammatory reaction (Premkumar, 2003). When monocytes enter tissue, they become macrophages, and help in fighting foreign material.

- **Thrombocytes** (platelets) are the smallest elements in blood. They are formed by large cells called megakaryocyte in the bone marrow. Platelets are responsible for the formation of blood clots at injury sites. This clot formation consists of calcium, vitamin K, and protein called fibrinogen. The life span of platelets is about 5-9 days (Premkumar, 2003).

### 1.2.2 The blood vessels

The blood vessels are a complex tube network in the human body. They are used to transport blood throughout the body. There are three types of blood vessels, as discussed below.

- **Arteries** are vessels carrying oxygenated blood from the heart to the body, except the pulmonary arteries which carry carbon-dioxide rich blood into the lungs. The blood pressure in arteries is time-varying resulting from the pumping of the heart. The pressure variation generates the pulse which is easily observed. Details of arteries will be discussed in §1.3.
- **Capillaries** are the smallest vessels, and are approximately 7 microns in diameter. Blood flows through arteries and these arteries branch into arterioles and further narrow into capillaries. Their thin walls are one cell thick composed of endothelium, a monolayer of endothelial cells. The exchange of gases, waste, and nutrient between blood and tissues takes place through these thin walls by diffusion (Sherwood, 2003).
- **Veins** are elastic vessels carrying waste-rich blood back to the heart, except the pulmonary veins that carry oxygenated blood from the lungs to the left atria. The range in size of veins is from 1 mm to 1-1.5 cm in diameter. Blood from capillaries draines into venules which are the smallest veins. Then several venules merge into larger veins, until the vena cava is reached and it then runs into the heart. Typically, the pressure in veins is relatively low compared to arteries. Venous walls are not as tough as those of arteries. This low-pressure condition in veins requires some adaptations to ensure that blood is returned to the heart. One is by having the large-diameter lumens. Another is valves inside the lumens to keep the blood flowing in one direction. Venous valves are most abundant in limbs veins in order to resist the gravity (Marieb & Hoehn, 2006).

## 1.3 Arteries

Arteries are relatively thick-walled, muscular blood vessels conveying oxygenated blood away from the heart, with the exemption of pulmonary arteries that carry deoxygenated blood from heart to the lungs. Once the blood is pushed out of the left ventricle, it enters the aorta, the largest artery with a diameter of roughly 2.5 cm. The aorta can be divided into three portions: ascending, arch, and descending.

The ascending aorta runs upward about 5 cm before curving at the aortic arch. The

right and left coronary arteries are the only branches of the ascending aorta. These two arteries are responsible for the delivery of oxygenated blood to the heart muscle. There are three arterial branches from the aortic arch: brachiocephalic artery, left common carotid artery, and subclavian artery. These three vessels supply blood to the upper half of the body.

The descending aorta runs downward, and becomes the abdominal aorta after it passes through the abdominal cavity. The abdominal aorta bifurcates into the iliac arteries which run into the bottom half of the body (Marieb & Hoehn, 2006).

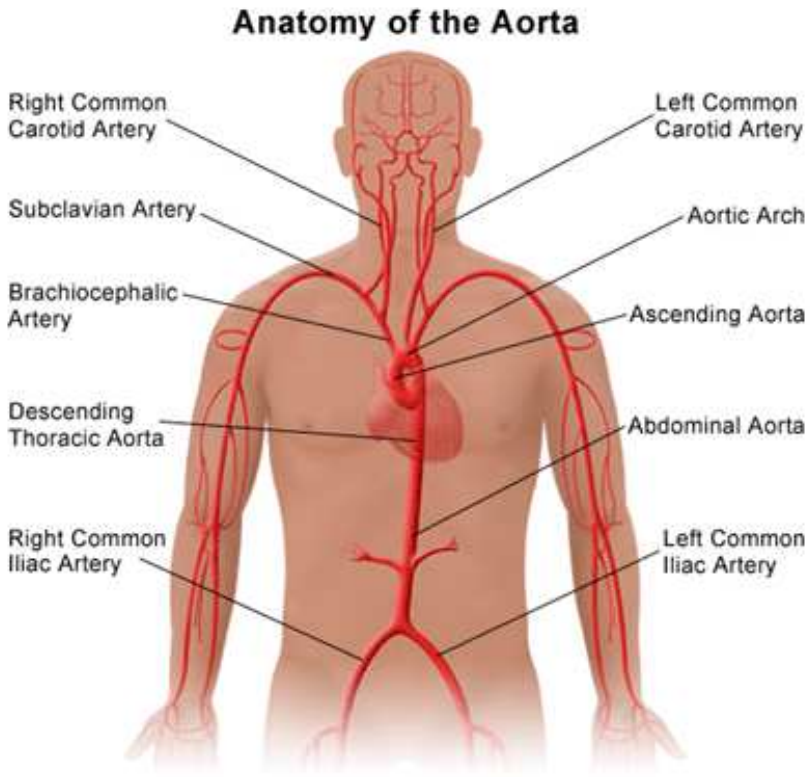



Figure 1.2: Anatomy of the aorta *http://www.daviddarling.info/encyclopedia/A/aorta.html*

### 1.3.1 Cellular components

#### 1.3.1.1 Endothelial cells

Endothelial cells are a monolayer of 1-2 $\mu$m thickness. They form a single cell layer inside vessels in the vascular system. They take part in several biological processes, for example, blood clotting, hormone metabolism and the development of new blood vessels from existing vessels, *angiogenesis*.

The endothelial cells filter the molecules that pass between the lumen and vascular wall. Different organs have different types of endothelium. They also play a vital role in controlling the vessel size when blood flows in the lumen. They release nitric oxide (NO) and endothelin to activate smooth muscle cells (discussed below) to dilate (*vasodilation process*) and contract (*vasocontraction process*) which results in changes in the vessel diameter (Vallance & Webb, 2000).

Endothelial dysfunction play an important role in the initiation and development of various vascular diseases by affecting the smooth muscle cells that generate vasodilation and vasocontraction to not function properly to the appropriate stimulus. This is an early marker of atherosclerosis, see §1.4.

#### 1.3.1.2 Smooth muscle cells

There are two distinct phenotypes of smooth muscle cells: contractile smooth muscle cells and synthetic smooth muscle cells. The contractile cell is rich in myofilaments, whereas the synthetic type contains large amounts of rough endoplasmic recticulum (RER). The former type responds to vasoactive substances which help to regulate vascular tone. The latter responds to cytokines (signaling molecules), the proliferation of the growth regulators, and secretes extracellular matrix components. This extracellular matrix, consisting mainly of collagen fibres, is the main component responsible for the elasticity and tensile strength of the arterial wall (Kádár & Glasz, 2001).

### 1.3.2 Arterial structure

Generally, arteries can be subdivided into two types: elastic and muscular arteries. Elastic arteries are the largest arteries which are situated near the heart, *e.g.* aorta, and their major branches, see Figure 1.2. These arteries are resposible for conducting blood from the heart to main sites within the body. Muscular arteries have smaller diameter and they branch from elastic arteries to supply blood to organs. Examples of this type of artery are the renal, splenic, hepatic arteries (Cliff, 1976). Both elastic and muscular arteries have the three distinct layers:

#### 1.3.2.1 Tunica intima

This is the innermost arterial layer consisting of one layer of endothelial cells. The intima is separated from the media by an internal elastic lamina, the outmost component of the intima, as shown in Figure 1.3. The internal elastic lamina consists of elastin so that the migration of the smooth muscle cells from the tunica media (§1.3.2.2) to the tunica intima takes place across the internal elastic lamina (Clark, 2004). For vessels larger than 1 mm in diameter, a subendothelial layer rich in collagen and elastic fibrils exists between the endothelial cells and the internal elastic lamina (Marieb & Hoehn, 2006; Junqueira & Carneiro, 2005).

#### 1.3.2.2 Tunica media

This is the middle arterial layer and is 2 mm thick. It contains 10-60 layers of smooth muscle cells surrounded by a network of collagen and elastins. Typically, this layer is the largest layer in arteries. The smooth muscle cells in tunica media are controlled by *vasomotor nerve fibres* of the nervous system, which affect either vasocontraction or vasodilation dependent upon the body activity. It is the most important layer in maintaining blood pressure and blood circulation (Marieb & Hoehn, 2006). Some of these smooth muscle cells are arranged circumferentially and others are organized helically. This arrangement causes the reduction in vessel diameter during the contraction phase. The opposite effect happens in relaxation phase (Premkumar, 2003).

The mechanical properties of the vessels are determined by the proportions of smooth muscle cells, collagen and elastins. For example, large arteries such as the aorta has a large proportion of elastin, which helps with the distribution of blood by propeling the blood toward periphery during diastole and retaining a continuous flow to the capillaries. The smaller arteries have relatively large amount of smooth muscle cells (Miller, 2006).

#### 1.3.2.3 Tunica adventitia

This is the outmost layer. It is separated from the media by the external elastic lamina, as shown in Figure 1.3. It consists largely of collagen fibres, together with nerve fibers, lymphatic and blood vessels (a so-called *vasa vasorum* or vessels of vessels). The large amount of collagen fibres helps to protect and reinforce the vessel. The collagen fibrils are arranged helically. They are important in strengthening the arterial walls. This layer is thickest in veins (Premkumar, 2003; Klabude, 2004; Marieb & Hoehn, 2006).

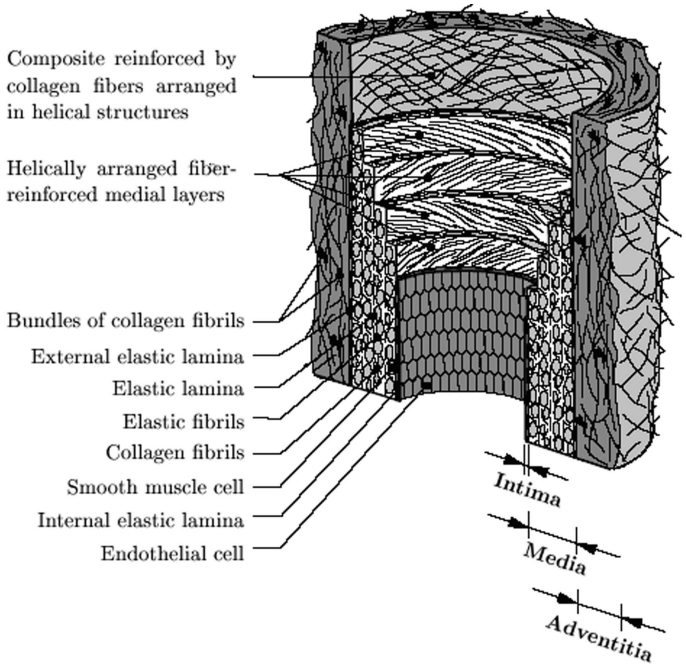



Figure 1.3: Anatomy of arterial wall (Holzapfel & Ogden, 2003).

### 1.3.3 Mechanical forces

The mechanical properties of an arterial wall are of great importance and play a role in the regulation of bloodstream. The structure of the arterial wall is characterized by a wide variability of material properties.

Since the tunica intima is very thin, consisting of a monolayer of endothelial cells, therefore, the arterial-wall mechanisms rely on the tunica media and the tunica adventitia. The structural arrangement of constituents in both the tunica media and the tunica adventitia is varying; smooth muscle cells in the tunica media are oriented circumferentially; collagen fibres in the tunica adventitia are oriented axially. This also suggests that the arterial wall is inhomogeneous and anistropic in which it is stiffer in circumferential and axial directions than a radial direction (Levy, 1999).

If the arterial wall was composed of elastin solely, an instantaneous deformation would be exhibited corresponding to an applied load. However, smooth muscle cells and collagen fibres all exist in an arterial wall and they are very stiff materials so they contribute to the strength of arterial walls.

Systematic variation in blood rheology is difficult *in vivo*. The researchers tend to use a simple approach to estimating the mechanical changes of blood vessels. Some of important vascular mechanisms are discussed below.

#### 1.3.3.1 Pressure, circumferential tension and stress

Blood pressure is the main determinant of vessel stretch. Blood pressure exerts forces on the vascular wall in a direction perpendicular to the endoluminal surface. These pressure forces are counterbalanced by the tangential forces in the longitudinal and circumferential directions from the vessel wall (Peterson et al., 1960; Lehoux & Tedgui, 2003). The relation between the force per unit length of the vessel (the circumferential wall tension), the intraluminal pressure and the vessel radius is given by (Lehoux & Tedgui, 2003),

$$T = Pr, \tag{1.1}$$

where $T$ is the circumferential wall tension, $P$ is the pressure and $r$ is the vessel radius, see Figure 1.4. The circumferential wall tension is caused by the contractile smooth cells and the collagen fibers. This circumferential tension is borne by the whole thickness of the vessel wall. Stress defines the average amount of force acting on a surface per unit area of a surface, and it can be applied in any direction: radial, circumferential or axial directions. Here, the circumferential stress, $\sigma$, exerted on the wall is defined by the tension in the equation (1.1) divided by the thickness of a wall $h$, *i.e.*

$$\sigma = \frac{Pr}{h}. \tag{1.2}$$

From (1.1), we know that the vascular tube which has a larger radius requires a larger wall tension to withstand a given blood pressure. Thus, the larger arteries usually have stronger walls.

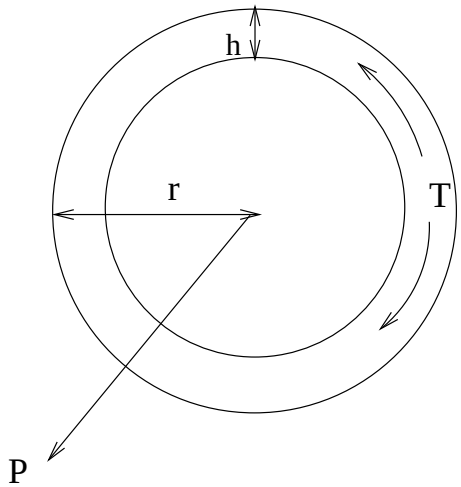



Figure 1.4: Pressure, tension and stress in arterial wall.

#### 1.3.3.2 Wall shear stress and blood flow

Poiseuille's law is usually applied to describe the flow characteristics in blood vessels due to its simplicity. The determinations of wall shear stress are subject to several assumptions (Katritsis et al., 2007): (1) blood behaves as a Newtonian fluid with a constant viscosity; (2) flow is steady and laminar; (3) the vessels are rigid-walled straight tubes with uniform circular cross-sectional area and are long in comparison to their diameter: and (4) blood does not slip at the vessel wall.

The blood velocity over a cross section normal to the flow direction has a parabolic shape in which the velocity is highest at the centre of the tube and zero at the walls due to the no-slip condition.

Shear stress results from blood flows by exerting a frictional force on the endothelial surface. Shear stress is equal to the product of the dynamic viscosity of blood and the velocity gradient in a direction perpendicular to a vascular wall for Newtonian fluid. In the case of Poiseuille flow, the wall shear stress, $\tau$, can be calculated analytically as (Lehoux & Tedgui, 2003),

$$\tau = \frac{4\mu Q}{\pi r^3} \tag{1.3}$$

where $Q$ is the volume flow rate, $\mu$ is the dynamic viscosity, and $r$ is the vessel radius.

Normally, the shear stress exerted by the fluid on the wall of large arteries is in the range 15-20 dynes/cm$^2$. However, during the systole, the shear stress can be up to 40 dynes/cm$^2$ (Ku et al., 1985; Malek et al., 1999). The variation in wall shear stress is caused by the intricate geometry of blood vessels and the variation in pressure. For example, the aortic arch which is an asymmetrically curved tube exhibits the high shear stress at the outside of the bend and the low shear stress at the inner wall under the steady flow assumption. This is due to the additional flow occuring across a cross section in a curved vessel. This flow is called *secondary flow*. The resultant combined primary and secondary flow patterns causes a bloodstream to have a screw-like motion which influences the distribution of the shear stress. This will be discussed in Chapter 2.

Once there is a change in shear stress, the endothelial cells recognize this change and subsequently send signals, such as nitric oxide, to vascular muscular cells to modify the vascular diameter (Shaaban & Duerinckx, 2000; Paszkowiak & Dardik, 2003). The change in wall shear stress can influence biological processes, for example, protein synthesis and secretion, gene expression and morphologic changes (Paszkowiak & Dardik, 2003).

#### 1.3.3.3 Hemodynamics

Hemodynamics is concerned with the physical principles governing the blood through the vascular system. This must be supported by a discussion of some physiological properties of blood and the interrelationship of blood flow rate, resistance and pressure.

Blood viscosity is principally determined by the percentage of blood that is made of a suspension of red blood cells, white blood cells and platelets in plasma. This cell suspension is called *hematocrit*. An increase in the presence of hematocrit increases blood viscosity and slows down the blood propagation velocities substantially. This blood nature makes it to be non-Newtonian fluid in the actual circulation. However, its non-Newtonian nature is merely relevant to the particular rheology such as in small arteries and capillaries where the diameter of arteries are relative to the size of cells. In medium to large arteries, such as aorta and coronary arteries, it has been well accepted that blood can be modelled as a viscous,

incompressible Newtonian fluid and the Navier-Stokes equations is usually considered to be a model for blood flow (Belloni, 1999).

The Bulk Flow Law is a basic law of hemodynamics. It is analogous to Ohm's law of electricity. It states that blood flow is directly proportional to the pressure difference, but inversely proportional to the resistance, *i.e.*

$$Q = \frac{\triangle P}{R} \tag{1.4}$$

where $Q$ is the flow rate, $\triangle P$ is the pressure difference between two points in a blood vessel and $R$ is the resistance.

Normally, resistance cannot be measured directly. It is obtained by measuring blood flow and pressure difference within a vessel. Resistance occuring in vessels throughout the body is varying. In case of Poiseuille flow, the resistance is given by

$$R = \frac{8\mu L}{\pi r^4}, \tag{1.5}$$

where $R$ is the resistance, $\mu$ is the dynamic viscosity, $L$ is the length of blood vessel and $r$ is the vessel radius.

Physically, the systemic arterioles provide the greatest resistance to blood flow. This contradicts to our intuition that the capillaries should contribute to the largest proportion of resistance because after all, the capillaries are much smaller. This can be explained by a series of vessel arrangement, since there are fewer arterioles in parallel than there are capillaries (Belloni, 1999).

## 1.4 Atherosclerosis

The term atherosclerosis is derived from the Greek *atheroma* meaning gruel and *sclerosis* meaning hardening. Atherosclerosis normally starts in an early childhood and the entent and severity increases with age. As mentioned in §1.3.1, endothelial dysfunction is an early marker of the initiation of atherosclerosis, which leads to the accumulation of a high concentration of cholesterol, in particular low-density lipoprotein (LDL) cholesterol, on the arterial wall. Atherosclerosis usually develops most in the carotid, coronary, and femoral arteries, and the abdominal aorta. It is rare to find atherosclerosis in other arteries. There is no particular reasons why the disease develops only in these arteries (Eckardstein, 2004).

Atherosclerosis tends to affect the intima of medium- and large-sized arteries. The initiation of the disease is associated with hypertension, inactivity, age, diabetes, smoking and male gender. These factors can activate the inflammation of endothelium cells on the intima layer. The pathogenesis of atherosclerosis has also been linked to the wall shear stress. Plaques are mostly found in the areas of low or oscillating wall shear stress such as on the outer wall of an arterial bifurcation and on the inside of the bends. This is because a decreased shear stress associates with a reduction of several vascular wall functions, including endothelial nitric oxide synthase production, vasodilatation and endothelial cell repair. Figure 1.5 shows the development of atherosclerotic plaque in a blood vessel.

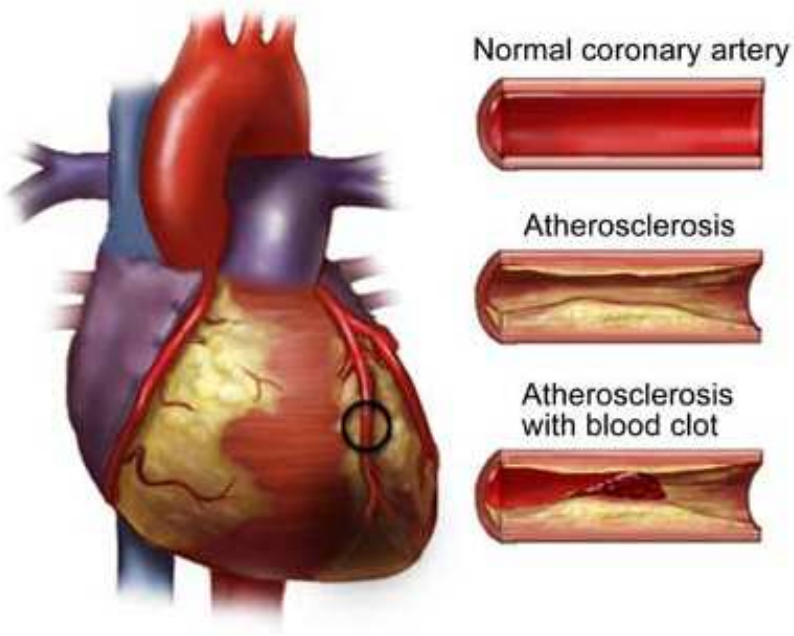



Figure 1.5: Diagram showing atherosclerotic plaque (*http://www.riversideonline.com*).

### 1.4.1 Development of atherosclerosis

#### 1.4.1.1 Early stage

The initiation of a plaque is caused by endothelial dysfunction. Endothelial dysfunction may result from high blood concentrations of free radicals and low-density lipoprotein (LDL) and low shear stress regions within the arterial wall such as arterial bifurcations. (Caro et al., 1971; Kádár & Glasz, 2001).

When endothelial cells are damaged, monocytes and T-cells present in blood adhere to the damaged area by vascular cell adhesion molecule-1 (VCAM-1). Later monocytes and T-cells enter into the intima stimulated by chemoattractant molecules; monocyte chemoattractic protein-1 (MCP-1) produced by endothelial cells and smooth muscle cells. Once monocytes are within the intima, they differentiate into macrophages (Stary et al., 1992; Libby et al., 1996; Bui et al., 2009).

Low-density lipoprotein (LDL) enters the intima through damaged endothelium and subsequently is oxidized by free radicals generated by nitric oxide (NO) from endothelial cells. At this stage, the low-density lipoprotein becomes oxidized LDL (oxLDL). The oxLDL binds to scavenging macrophages, giving rise to lipid-loaded macrophages. Macrophages continue to ingest modified LDL until they are not capable of any further ingestion, then they die by a process called *apoptosis*. This extracellular lipid (foam cells) contributes to the lipid-rich core or necrotic plaque, see Figure 1.6.

The oxLDL can also stimulate the release of monocyte chemoattractic protein-1 (MCP-1) from endothelial cells. Oxidized LDL can cause endothelial cell loss, which leads to the exposure of subendothelial tissue to blood in the lumen (Porth, 2006).

The activated macrophages also secrete chemoattractants and free radicals resulting in further oxidation of LDL. Additionally, macrophages generate proteolytic enzymes which contribute to fatty plaques (Warrell et al., 2005).

T-cells are present in artherosclerotic plaque in all stages of the process. They are activated by antigen-presenting cells such as macrophages, and they then differentiate becoming a T-helper 1 cell ($T_h1$). $T_h1$ secretes the pro-inflammatory cytokines that promote atherosclerotic lesion and plaque vulnerability by attracting more macrophages and T cells into the lesion (Warrell et al., 2005).

#### 1.4.1.2 Late stage

After the foam cells form, the plaque develops into a more complex lesion called a *fibrous plaque* or *atheroma*. In early stage, the foam cells release growth factor and cytokines that promote the migration of smooth muscle cells from media to intima. The smooth muscle cells change from contractile to synthetic type and subsequently they produce extracellular matrix. The extracellular matrix may bind to OxLDL or LDL, which helps in the formation of a fibrous cap on the vasucular wall ( see Figure 1.6 ). The fibrous cap of the plaque is the distinct layer composed of collagen. It covers the lipid core containing extracellular lipid derived from intracellular lipid released from cells that die. One of the factors for the plaque to rupture is the thickness of this fibrous cap (Eckardstein, 2004; Warrell et al., 2005).

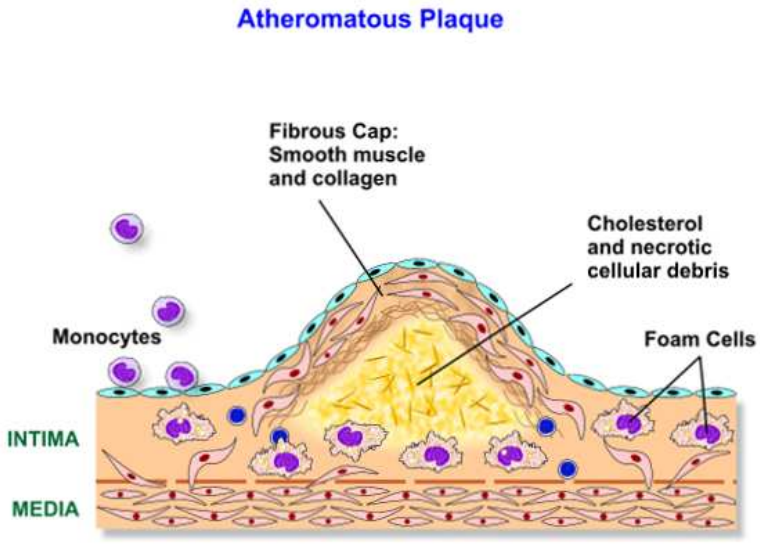



Figure 1.6: Diagram showing the atheroma plaque (*http://medinfo.ufl.edu*).

### 1.4.2 Remodelling

The structure of an arterial wall is sensitive to the hemodynamic forces exerted on it by blood flow and blood pressure. As plaques advance into late-stage lesions, blood vessels accommodate the changing hemodynamic forces by adapting their geometry in order to maintain the normal condition of the flow. For example, the intima may thicken in response to reduced wall shear stress in the low shear stress region and this results in the elevated flow velocity due to reduced lumen diameter and subsequently restore normal wall shear stress (Stary et al., 1992). The terminology of the changes of the blood vessels' geometry is *remodelling*. The mechanism of plaque remodelling is poorly understood due to the lack

of experimental models (Stary et al., 1992). There are two types of remodelling: positive remodelling and negative remodelling, see Figure 1.7.

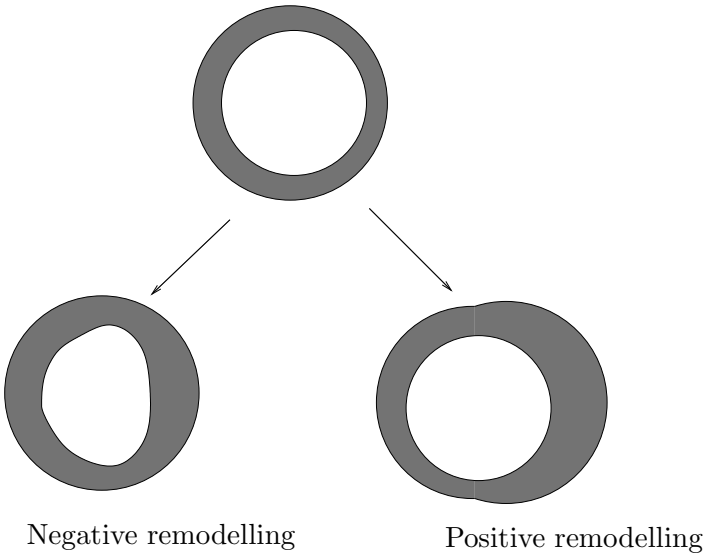



Figure 1.7: Diagram showing the negative and positive remodelling.

Positive remodelling is also referred to as outward or expansion remodelling. This remodelling preserves the lumen's diameter despite the presence of the plaque. Whilst negative remodelling appears as localized bulges into a lumen in an artery that is allowed to contract or collapse (Stary et al., 1992). It is reported that plaques that undergo positive remodelling have a larger lipid core, thinner fibrous cap, and less smooth muscle cells and collagens than those that undergo negative remodelling. Plaques with positive remodelling are considered to be *vulnerable* plaques , meaning they are prone to rupture. Plaques with negative remodelling tend to be relatively more stable with a small lipid core and a higher collagen density (Stary et al., 1992; Fuster et al., 2004; Thim et al., 2008). Calcified plaques are associated with inward remodelling.

Therefore, there exists a paradox in which positive remodelling may be beneficial in terms of protecting against luminal narrowing but also increases a likelihood of plaque rupture. In contrast, plaques with negative remodelling appear to be more stable but may be involved with higher grade occlusion.

It is suggested that positive remodelling and rupture plaques have similar underlying mechanisms due to the presence of macrophages and T-cells together with metalloproteinases (MMPs), a group of enzymes involving the extracellular matrix degradation. In experimental studies, MMP inhibition reduces the enlargement of an arterial wall and improve collagen matrix integrity which helps in stabilizing plaque (Varnava et al., 2002; Ward et al., 2000).

Both positive and negative remodellings can be observed over the length of the same artery. Positive remodelling occurs in an early stage of atherosclerotic plaque and some, but not all, develop as negative remodelling. It is also suggested negative remodelling may occur in early formation of plaque as it fails to adapt itself to be positive remodelling (Hirose et al., 2003).

Most clinical studies have shown that negative remodelling is more common in smokers, whilst positive remodelling is associated with hypercholesterolemia.

### 1.4.3 Plaque rupture

Plaque becomes susceptible to rupture due to a combination of biomechanical forces dependent upon (i) the size and consistency of the atherosclerotic core, (ii) the thickness of fibrous cap, and (iii) inflammation and repair within the cap.

The size of the lipid core is critical to the stability of a plaque. A plaque with a large lipid-core is subjected to an increased tensile circumferential stress, which increases the vulnerability of the plaque. The consistency of the core is also important. Usually the consistency depends upon a local temperature rise in the affected tissues and lipid composition. In normal arteries, temperature remains constant, whereas temperature in most plaques is higher than healthy blood vessels (Pasterkamp et al., 2000). At room temperature, the consistency of core is similar to a toothpaste. As the temperature increases, the liquid cholesteryl ester contained in the core becomes softer resulting in an unstable plaque.

Thickness, strength and stiffness of the fibrous cap varies over the plaque. A thin cap with reduced collagen content increases the tendency of a plaque to rupture. A lesion's shoulder, where macrophages enter and proliferate and are activated, is the thinnest region in the plaque, thereforee this is the region where a plaque tends to rupture. Collagen is the main component of a fibrous cap. A ruptured cap contains less collagen than an unimpaired cap. Coronary plaques with a fibrous cap thickness thinner than 65 $\mu$m are usually found in a patient dying from acute cardiac syndrome. Disrupted fibrous caps are usually heavily infiltrated by a high number of activated macrophages which results in the ongoing inflammation (Thim et al., 2008).

Haemodynamic forces may also trigger rupture of the vulnerable plaques. By Laplace's law, higher blood pressure induces a larger tension in the wall. If the wall components can not bear the load, the tension force is redistributed to the fibrous cap. This implies that the thinner the fibrous cap, the more likely the plaque is to rupture (Pasterkamp et al., 2000).

### 1.4.4 Thrombosis

Thrombosis is a process defining a blood clot (thrombus) within a blood vessel. Thrombosis within a lumen occurs for two different processes. One is when the endothelial surface erodes with no rupture of thrombotic plaque and a thrombus is formed to cover this eroded area. Endothelial erosion is usually associated with a severe atherosclerotic stenosis (a narrowing in blood vessel) (Pasterkamp et al., 2000). It is reported that plaque erosion is the leading cause of sudden cardiac death in premenopausal women (Voelker, 1998).

The second mechanism for thrombus formation is a plaque disruption. Here, there exists a crack in a fibrous cap allowing blood from lumen entering into a plaque's lipid core. It is reported that the incidence of occlusive thrombi due to plaque disruption is between 1.3 and 3 times that of endothelial erosion (Davies, 1998; Zaman et al., 2000).

Tissue factor is the primary cellular initiator of thrombosis. It is a glycoprotein that mediates activation of the coagulation cascade. In healthy arteries, tissue factor is present in the adventitia and is abundant in the lipid-rich core of the plaque (Toschi et al., 1997). Once a vessel injures, tissue factor becomes exposed to bloodstream and subsequently the coagulation cascade takes place, triggering the formation of a superimposed thrombus which induces platelet activation and fibrin formation.

An intraplaque thrombus consisting mainly of platelets forms and results in a plaque expansion. Ultimately an intraplaque thrombus grows and reseals a rupture site to prevent a luminal blood flowing into the plaque. A thrombus has now a larger component of densely

packed fibrin and platelets and is exposed to flowing blood in a lumen. Commonly, a propagated thrombus partially occludes the lumen, whilst a complete lumen occlusion is rare. At this stage, the distal embolization, the blockage of smaller downstream vessels, may occur (Pasterkamp et al., 2000).

It is found that high levels of tissue factor exposed to flowing blood increase the plaque thrombogenicity. Inhibition of tissue factor helps in reducing thrombus propagation (Mackman, 2004).

### 1.4.5 Treatment

There are various treatments to cure arterial disease dependent on the stage of the disease. At the early stage of the disease, cholesterol-lowering drugs would be suggested. This includes cholestyramine and cholestipol. These are usually taken with statin and niacin for effective results as statins can reduce the expression of MMP in a plaque. These oral medications stablilize plaques by decreasing plaque inflammation, foam cell number and activity, and by increasing the density of plaque collagen matrix. Aspirin is also known to prevent thrombosis (Brown, 2002).

For relatively severe coronary artery disease, surgical methods can be used for lumen reconstruction such as atherectomy, balloon angioplasty, stent placement and bypass grafting.

Atherectomy is a plaque-removal procedure. A catheter is inserted into the artery to the narrowing area and it shaves off strips of lipid-rich plaque. The plaque is subsequently collected at the laser tip of catheter.

Balloon angioplasty is a procedure to open narrowed blood vessels by applied force from an inflated balloon. This helps to expand the blood vessels. At later times, a small metal mesh tube called a stent may be inserted into the vessel. This provides inner support for the vessel wall.

Bypass grafting is a procedure used to divert blood around the blocked part of an artery by creating a bridge that bypasses the blockage area. Conventionally an artery from behind the breast bone, and veins from the legs are used to form the bridge (Brown, 2002).

However, prevention is the highest form of an atherosclerosis treatment. The weight reduction (for obese people), exercise, stop smoking and healthy diet consumption are all helpful to reduce LDL- and elevate HDL- cholesterol levels.

## 1.5 Thesis outline

As mentioned in §1.4, atherosclerotic plaques tend to be localized at sites of branching and artery curvature where flow patterns are complicated. The noninvasive methods for determining flow patterns *in situ* do not provide sufficient details to describe the complex flow patterns and precise localization of early lesions. Researchers postulated that fluid dynamics might play an important role in the initiation and development of atherosclerosis. Therefore, complete understanding of the relationship between the behaviours of blood flow, and symptoms has been required in order to provide insight into the sites at which plaques develop.

The overarching aim of this thesis is to model blood flow in arteries in the vicinity of an atherosclerotic plaque. We first contrived to model the two-dimensional, two-phase flows in a curved tube, in which an atherosclerotic lesion is approximated by a mathematically thin film. Unfortunately, we do not pursue this goal model in this thesis due to the incomplete

work. Instead, we consider the simpler model, *i.e.* two-layer viscous fluids in a rigid, straight channel is only conducted in this thesis. We should note that most materials in this thesis, Chapter 1-4, are the review associated with our aimed and unfinished model, the two-dimensional thin film flows in curved tubes.

With the idea of finding the correlations between observed *in situ* sites of plaques and the flow dynamics, the studies of flows in curved tubes are important as regards locations where plaques tend to occur. We then will review the modelling studies, numerical computations and experiments on steady and unsteady, two dimensional flows in a curved tube in Chapter 2.

Blood in small arteries is a non-Newtonian fluid. The viscosity of blood decreases with increasing in velocity gradient *i.e.* it is shear thinning. At high shear rates, such as in capillaries, the blood viscosity is reduced, thus facilitating blood flow. However, in medium- and large- arteries, this effect is irrelevant and so blood can be modelled as a Newtonian fluid. Therefore, throughout this thesis, we model blood as an incompressible, viscous, Newtonian fluid and an artery as a rigid-walled tube.

The governing equations of motion are determined from the continuity and the nonlinear Navier-Stokes equations for an incompressible viscous fluid. We then consider flows driven by (i) a steady pressure gradient and (ii) an oscillatory pressure gradient with zero and non-zero mean. In the case of flow driven by a steady pressure gradient, we classify three distinct regimes corresponding to the Dean number $D$, which characterizes the steady component of the pressure gradient. Asymptotic solutions are developed for small values of $D$. For intermediate and large values of $D$, the problems are normally solved computationally.

In addition to the dimensionless parameters $D$, the flow is parameterized by the Womersley number $\alpha$, the ratio of the unsteady inertia to the vicous effects, and a secondary streaming Reynolds number $R_s$ which characterizes the behaviour of the steady core flow in the case when an oscillatory axial pressure gradient drives the flow. Under a sinusoidal pressure gradient ($D = 0$) condition, solutions are found by using regular perturbation techniques. Whilst for unsteady pulsatile flows ($D \neq 0$), the flow behaviours are far more complex so the computation becomes an essential tool for the investigation.

As we treat the atherscleroticplaque as a thin film flow, so in Chapter 3, a number of different aspects of thin-film flow are investigated. The derivation of the lubrication equation of the thin liquid films in the presence of surface tension, gravity and surface tension gradient is presented in §3.1. Stability of thin film as well as the formation of unduloids or liquid bridges in a straight cylindrical tube are discussed in §3.2. Despite its irrelevance to our goal model, Marangoni flows are included due to its versatility in biological applications. A more practical rheology of plaque can take into account of contact line motion, therefore the study of moving contact line is essential. The moving contact line problem will be studied briefly in §3.4.

We then pursue the study of complex thin-film flows on curved substrates in Chapter 4. The leading-order equations governing flows on curved substrates are derived in §4.1. Following (Howell, 2003), three possible cases are identified dependent on the substrate curvature; (i) small (ii) large, but nearly constant, or (iii) large but not nearly constant. A literature review of this field, and examples of flow on curved substrates are studied in §4.2.

As we treat the system of plaque and blood flow as a bilayer Newtonian thin film, so the two dimensional bilayer immicible viscous fluids in a confined channel are modelled in Chapter 5. Lubrication theory is used to derive nonlinear coupled equations governing flows of both layers. The thickness of the lower layer is then assumed to be much thinner than that of the upper layer, from which the evolution equation of the fluid-fluid interface

is obtained. Linear stability analysis is performed in §5.2. The nonlinear stability of the steady state and transient flows are investigated computationally using appropriate initial conditions and a range of parameters for the solutions.

Note that the models we develop are not only practically useful in biology, but they may be applied in such various phenomena such as in paper lamination and other decorative uses, as well as coating process.

In chapter 6, general conclusions are presented and further work is suggested.

# Chapter 2

# Flows in curved tubes

## 2.1 Introduction

In this chapter, we review flows in curved tubes. In the previous chapter, we described how an atherosclerotic plaque is developed in an arterial wall. It is now known that the development of atherosclerotic plaques is associated with the distribution of arterial wall shear stress, in particular, the disease tends to develop in regions of low or oscillating wall shear stress as these are regions where several vascular wall functions reduce, for example, endothelial nitric oxide synthase and vasodilation. The examples of plaque-prone locations are walls of arterial bifurcations, branches, or junctions, where the vascular curvature is an important feature to determine flow behaviours in these particular areas (Caro et al., 1971).

Fluid flows in curved tubes have been studied extensively due to many applications in the real world, in particular, engineering and physiology. Flow in a curved tube is more complicated than flow in a straight tube due to the presence of the transverse components of velocity. Fluid particles travel along a tube driven by the axial pressure gradient. This pressure gradient acting on fluid particles is approximately uniform. The velocity of the fluid near the wall is much slower than velocity of fluid in the core due to the no-slip condition. Therefore, the fluid particles in the core experience a larger centrifugal force compared with the fluid particles near the wall. Consequently, the fluid in the centre of the tube will be forced to move to the outside of a bend. The fluid at the outside of the bend will then be forced to move towards the inside of the bend along the wall due to the lower pressure there (Pedley, 1980). Figure 2.1 shows an example of flow in a curved tube. The term primary flow refers to flow in the axial direction, whereas a secondary flow refers to flows in the cross section of the tube. The combination of these two flows causes the overall flows which exhibit a spiral type motion.

A secondary flow was primarily observed in the late $19th$ century by Thomson (1877) who studied the erosion of river bends. Nevertheless, the most fundamental theoretical approach in this area was by Dean (1928) who studied the steady motion of viscous fluid in a slightly curved circular tube by assuming that the dimensionless curvature ratio $\delta = a/R$ is small, corresponding to a weakly curved tube. Here, $a$ is the radius of the constant circular cross section, and $R$ is the radius of curvature of the planar centerline. He defined the non-dimensional parameter $K = 2\delta(Re)^2$, where $Re$ is the corresponding Reynolds number which describes the relative importance of inertia to viscosity in a straight tube. The parameter $K$ is known as the *Dean number* and used to characterize the steady component of the pressure gradient. Dean's calculation was restricted to small values of $K$ only.

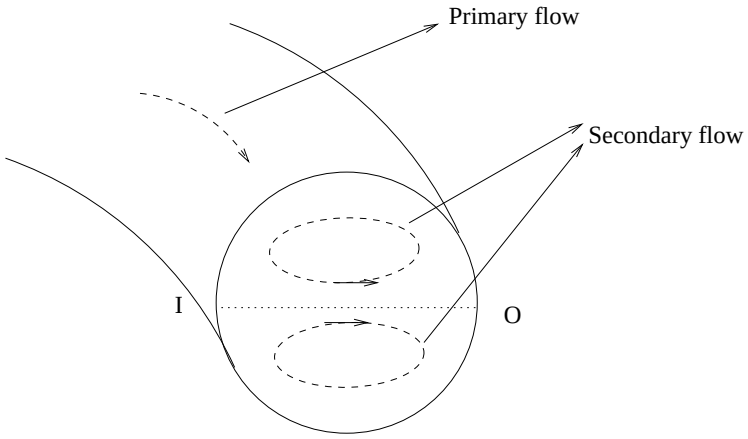



Figure 2.1: Diagram showing the the primary and secondary flows in the curved tube, where O, and I denote the outer and inner of the bend respectively.

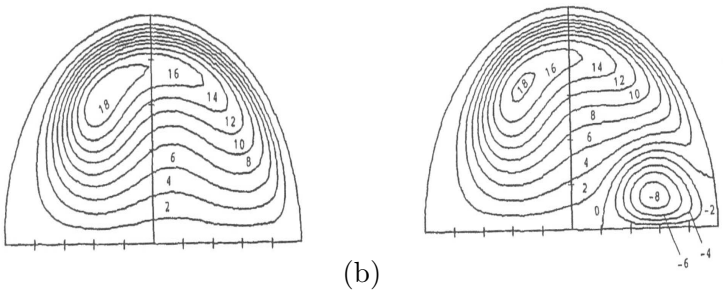



Figure 2.2: Streamlines of multiple steady state solutions for $D = 5000$; (a) Two-vortex solution, (b) four-vortex solution. Reproduced from Yanase et al. (1989).

There have since been numerous papers published that use numerical simulations to study more general solutions for larger values of the Dean number (McConalogue & Srivastava, 1968; Truesdell & Adler, 1970; Austin & Seader, 1973; Collins & Dennis, 1975). Numerical investigations have revealed the existence of saddle-node bifurcation in the flow profile when the axial pressure gradient is sufficiently high (Dennis & NG, 1982; Yanase et al., 1989; Daskopoulos & Lenhoff, 1989). This results in multiple steady-state solutions, *e.g.* illustrated in Figure 2.2 (Yanase et al., 1989).

Lyne (1971) was the first to consider oscillatory flow in which the axial pressure gradient varies sinusoidally in time with a certain frequency. This unsteady flow depends on the dimensionless parameters $\alpha$ and $R_s$, where $\alpha$ represents the dimensionless frequency of the flow and $R_s$ is the secondary-streaming Reynolds number based on the mean secondary flow. The secondary-streaming Reynolds number $R_s$ determines the behaviour of the steady secondary flow in the core. Lyne investigated the effect of varying $R_s$ for large $\alpha$ using matched asymptotic expansions. He considered solutions in two regions; an outer core region and an inner Stokes layer on the wall. His analysis will be presented later in §2.4.1. We will then follow the calculation of Zalosh & Nelson (1973), and Mullin & Greated (1980) for the unsteady flow driven by a low-frequency oscillatory pressure gradient.

The more general case of oscillatory flow in which the pressure gradient oscillates about

a non-zero mean has been treated in the work by Smith (1975) and Blennerhassett (1976) later in §2.4.2. Smith examined the flow behaviour in various regimes dependent on the size of the dimensionless parameters $D = 4K^{1/2}$ or $\alpha$, with $R_s = O(1)$. Blennerhassett followed Lyne's analysis in which there exists Stokes layer near the wall and the core flow depends on two parameters $D$ and $R_s$. However, the most crucial parts in Blennerhassett's work are his numerical results which will be presented. Siggers & Waters (2008) considered the unsteady flow with finite curvature in which the effects of Coriolis forces are present.

In this chapter, we will consider both steady and unsteady fully developed flows in a curved tube of circular cross section. The fluid is modelled as a viscous Newtonian fluid. The governing equations and conditions will be introduced in §2.2. In §2.3 the steady flows will be classified into three regimes corresponding to the size of the Dean number $D$. In §2.4, we will study the unsteady flow driven by a sinusoidal axial pressure gradient ($D = 0$), and an oscillatory axial pressure gradient ($D \neq 0$). The main sources of material in this chapter are the book by Pedley (1980), and the review paper by Berger et al. (1983).

## 2.2 Governing equations and parameters

Consider a rigid-walled curved tube with uniform circular cross-section with radius $a$. The tube centreline lies on a circle of radius $R$. We assume that the dimensionless curvature ratio $\delta = a/R$ is small, *i.e.* $\delta \ll 1$. The fluid is assumed to be an incompressible, viscous, Newtonian fluid with density $\rho$, and kinematic viscosity $\nu$.

We introduce the curvilinear coordinate system $(r, \theta, s)$, where $(r, \theta)$ are polar coordinates in the plane of cross section, and $s$ is the distance measured along the centreline. We denote by the unit vectors $(\mathbf{e}_r, \mathbf{e}_s, \mathbf{e}_\theta)$ the curvilinear-coordinate directions, as illustrated in Figure 2.3.

The velocity components are $\mathbf{u} = (u, v, w)$. We denote by $p$ and $t$ the pressure and time respectively. We first consider the flow driven by a steady axial pressure gradient $-\hat{G}$.

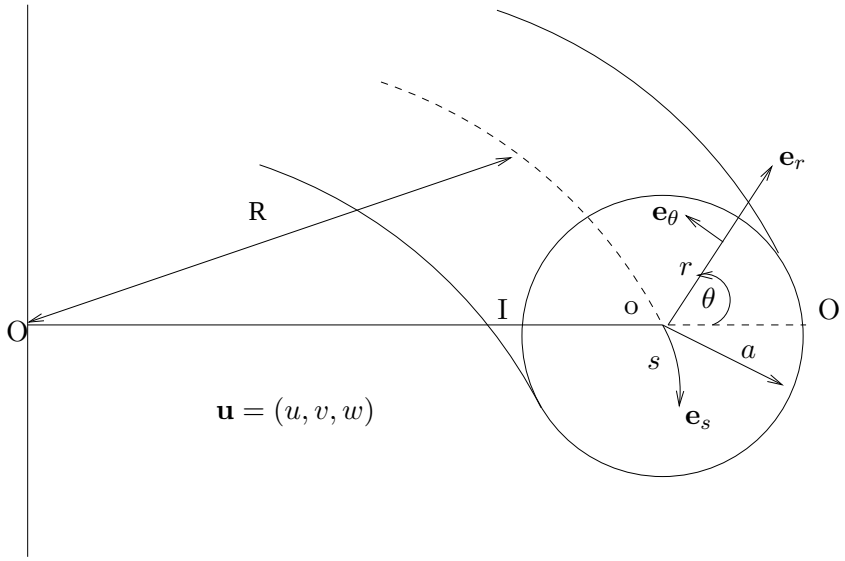



Figure 2.3: The curvilinear co-ordinate system.

Throughout this chapter, we will consider fully-developed flows so that the velocity field

$\mathbf{u}$ is independent of $s$. The dimensional governing equations then are (Waters, 2007):

$$\frac{\partial u}{\partial r}+\frac{u}{r}+\frac{1}{r}\frac{\partial v}{\partial \theta}+\frac{u\cos\theta-v\sin\theta}{R+r\cos\theta}=0, \tag{2.1}$$

$\mathbf{e}_r$:

$$\frac{\partial u}{\partial t}+u\frac{\partial u}{\partial r}+\frac{v}{r}\frac{\partial u}{\partial \theta}-\frac{v^2}{r}-\frac{w^2\cos\theta}{R+r\cos\theta}=-\frac{1}{\rho}\frac{\partial p}{\partial r}-\nu\left[\left(\frac{1}{r}\frac{\partial}{\partial\theta}-\frac{\sin\theta}{R+r\cos\theta}\right)\left(\frac{\partial v}{\partial r}+\frac{v}{r}-\frac{1}{r}\frac{\partial u}{\partial\theta}\right)\right], \tag{2.2}$$

$\mathbf{e}_\theta$:

$$\frac{\partial v}{\partial t}+u\frac{\partial v}{\partial r}+\frac{v}{r}\frac{\partial v}{\partial \theta}+\frac{uv}{r}+\frac{w^2\sin\theta}{R+r\cos\theta}=-\frac{1}{r\rho}\frac{\partial p}{\partial\theta}+\nu\left[\left(\frac{\partial}{\partial r}+\frac{\cos\theta}{R+r\cos\theta}\right)\left(\frac{\partial v}{\partial r}+\frac{v}{r}-\frac{1}{r}\frac{\partial u}{\partial\theta}\right)\right], \tag{2.3}$$

$\mathbf{e}_s$:

$$\begin{aligned}&\frac{\partial w}{\partial t}+u\frac{\partial w}{\partial r}+\frac{v}{r}\frac{\partial w}{\partial\theta}+\frac{w}{R+r\cos\theta}(u\cos\theta-v\sin\theta)=\frac{R\hat{G}}{\rho(R+r\cos\theta)}\\&+\nu\left[\left(\frac{1}{r}\frac{\partial}{\partial r}\right)\left(r\frac{\partial w}{\partial r}+\frac{rw\cos\theta}{R+r\cos\theta}\right)+\frac{1}{r}\frac{\partial}{\partial\theta}\left(\frac{1}{r}\frac{\partial w}{\partial\theta}-\frac{w\sin\theta}{R+r\cos\theta}\right)\right].\end{aligned} \tag{2.4}$$

Note that (2.1) is the continuity equation, and (2.2)–(2.4) are the momentum equations in $\mathbf{e}_r-$, $\mathbf{e}_\theta-$ and $\mathbf{e}_s-$directions respectively.

Let the typical velocity scale by $U_0=\nu/a$. We then non-dimensionalise via (Pedley, 1980)

$$r'=\frac{r}{a},\qquad t'=\frac{\nu}{a^2}t,\qquad p'=\frac{a^2p}{\rho\nu^2},\qquad \mathbf{u}'=\frac{a\mathbf{u}}{\nu}, \tag{2.5}$$

where primes denote dimensionless variables.

The full dimensionless governing equations are (dropping primes):

$$\frac{\partial u}{\partial r}+\frac{u}{r}+\frac{1}{r}\frac{\partial v}{\partial\theta}+\frac{\delta u\cos\theta-\delta v\sin\theta}{h}=0, \tag{2.6}$$

$\mathbf{e}_r$:

$$\frac{\partial u}{\partial t}+u\frac{\partial u}{\partial r}+\frac{v}{r}\frac{\partial u}{\partial\theta}-\frac{v^2}{r}-\frac{\delta w^2\cos\theta}{h}=-\frac{\partial p}{\partial r}-\left(\frac{1}{r}\frac{\partial}{\partial\theta}-\frac{\delta\sin\theta}{h}\right)\left(\frac{\partial v}{\partial r}+\frac{v}{r}-\frac{1}{r}\frac{\partial u}{\partial\theta}\right), \tag{2.7}$$

$\mathbf{e}_\theta$:

$$\frac{\partial v}{\partial t}+u\frac{\partial v}{\partial r}+\frac{v}{r}\frac{\partial v}{\partial\theta}+\frac{uv}{r}+\frac{\delta w^2\sin\theta}{h}=-\frac{1}{r}\frac{\partial p}{\partial\theta}+\left(\frac{\partial}{\partial r}+\frac{\delta\cos\theta}{h}\right)\left(\frac{\partial v}{\partial r}+\frac{v}{r}-\frac{1}{r}\frac{\partial u}{\partial\theta}\right), \tag{2.8}$$

$\mathbf{e}_s$:

$$\begin{aligned}\frac{\partial w}{\partial t}+u\frac{\partial w}{\partial r}+\frac{v}{r}\frac{\partial w}{\partial\theta}+\frac{\delta w}{h}(u\cos\theta-v\sin\theta) &= \frac{\hat{G}a^3}{h\rho\nu^2}+\frac{1}{r}\frac{\partial}{\partial r}\left(r\frac{\partial w}{\partial r}+\frac{\delta rw\cos\theta}{h}\right)\\&+\frac{1}{r}\frac{\partial}{\partial\theta}\left(\frac{1}{r}\frac{\partial w}{\partial\theta}-\frac{\delta w\sin\theta}{h}\right).\end{aligned} \tag{2.9}$$

The function $h(r,\theta)=1+\delta r\cos\theta$ is $1/R$ times the distance from the centre of curvature of the centreline (at a particular $s$) to the projection on the plane containing the centreline of a general point $(r,\theta,s)$.

In order that the centrifugal force terms are formally of the same order as the viscous and inertial terms in the limit $\delta \to 0$, the axial velocity is rescaled by taking

$$w \to \frac{w}{\sqrt{2\delta}}. \tag{2.10}$$

In the weakly curved tube limit, $\delta \ll 1$, the governing equations reduce to

$$\frac{\partial u}{\partial r} + \frac{u}{r} + \frac{1}{r}\frac{\partial v}{\partial \theta} = 0, \tag{2.11}$$

$\mathbf{e}_r$:

$$\frac{\partial u}{\partial t} + u\frac{\partial u}{\partial r} + \frac{v}{r}\frac{\partial u}{\partial \theta} - \frac{v^2}{r} - \frac{w^2\cos\theta}{2} = -\frac{\partial p}{\partial r} - \frac{1}{r}\frac{\partial}{\partial \theta}\left(\frac{\partial v}{\partial r} + \frac{v}{r} - \frac{1}{r}\frac{\partial u}{\partial \theta}\right), \tag{2.12}$$

$\mathbf{e}_\theta$:

$$\frac{\partial v}{\partial t} + u\frac{\partial v}{\partial r} + \frac{v}{r}\frac{\partial v}{\partial \theta} + \frac{uv}{r} + \frac{w^2\sin\theta}{2} = -\frac{1}{r}\frac{\partial p}{\partial \theta} + \left(\frac{\partial v}{\partial r} + \frac{v}{r} - \frac{1}{r}\frac{\partial u}{\partial \theta}\right), \tag{2.13}$$

$\mathbf{e}_s$:

$$\frac{\partial w}{\partial t} + u\frac{\partial w}{\partial r} + \frac{v}{r}\frac{\partial w}{\partial \theta} = D + \left(\frac{\partial^2 w}{\partial r^2} + \frac{1}{r}\frac{\partial w}{\partial r} + \frac{1}{r^2}\frac{\partial^2 w}{\partial \theta^2}\right), \tag{2.14}$$

where $D = \sqrt{2\delta}\hat{G}a^3/\mu\nu$ is the Dean number.

We can also consider an axial pressure gradient that varies sinusoidally in time, given by $\hat{G} + \alpha^2 W\cos\alpha^2 t$, where $W$ is a dimensionless velocity amplitude that would be driven by a pressure gradient in a straight tube containing an inviscid fluid. The parameter $\alpha^2 = \omega a^2/\nu$, with $\omega$ the frequency of oscillation. By (2.11), we can introduce a streamfunction $\psi(r,\theta)$ such that

$$u = \frac{1}{r}\frac{\partial \psi}{\partial \theta}, \qquad v = -\frac{\partial \psi}{\partial r}. \tag{2.15}$$

Substituting (2.15) into (2.12) and (2.13) and eliminating the pressure terms, we obtain

$$\alpha^2\frac{\partial \nabla^2\psi}{\partial \tau} + \frac{1}{r}\left(\frac{\partial \psi}{\partial \theta}\frac{\partial}{\partial r} - \frac{\partial \psi}{\partial r}\frac{\partial}{\partial \theta}\right)\nabla^2\psi - w\left(\sin\theta\frac{\partial w}{\partial r} + \frac{\cos\theta}{r}\frac{\partial w}{\partial r}\right) = \nabla^4\psi, \tag{2.16}$$

where $\tau = \alpha^2 t$, and

$$\alpha^2\frac{\partial w}{\partial \tau} + \frac{1}{r}\left(\frac{\partial \psi}{\partial \theta}\frac{\partial w}{\partial r} - \frac{\partial \psi}{\partial r}\frac{\partial w}{\partial \theta}\right) = D + \alpha^3\sqrt{2R_s}\cos\tau + \nabla^2 w. \tag{2.17}$$

The dimensionless parameters are:

- **The Dean number** $D = \sqrt{2\delta}G = \sqrt{2\delta}\hat{G}a^3/\nu\mu$ where $\hat{G}$ is the dimensional pressure gradient.
- **The Womersley number** $\alpha = a\sqrt{\omega}/\sqrt{\nu}$, where $\omega$ is a frequency of oscillation.
- **The secondary streaming Reynolds number** $R_s = \delta W^2\nu/\omega a^2$.

These dimensionless parameter descriptions will be presented in the following section. Equations (2.16) and (2.17) must be solved subject to the no-slip boundary conditions

$$\psi = \frac{\partial \psi}{\partial r} = w = 0 \qquad \text{at} \qquad r = 1. \tag{2.18}$$

### 2.2.1 Parameter descriptions

1. **Dean number** $D$
   This dimensionless parameter characterizes the steady component of the pressure gradient. There are various definitions of the Dean number. Originally, Dean used

$$K = 2\delta \left( \frac{aW_0}{\nu} \right)^2 = 2\delta (Re)^2 \tag{2.19}$$

   where $W_0$ is the maximum velocity in a straight tube and $Re$ the corresponding Reynolds number of the straight tube flow.
   The parameter $\kappa$ has also been used, mainly in experimental work (White, 1929). It is defined such that

$$\kappa = \delta \left( \frac{aW_0}{\nu} \right) = \sqrt{\delta}(Re) \tag{2.20}$$

   *i.e.* $\kappa = (K/2)^{1/2}$. McConalogue & Srivastava (1968) defined the Dean number by

$$D = \sqrt{2\delta} G = \frac{\sqrt{2\delta}\hat{G}a^3}{\nu\mu}, \tag{2.21}$$

   where $G$ is the dimensionless mean pressure gradient, and $\hat{G}$ is the dimensional pressure gradient in which $\hat{G}a^2/\mu$ is four times the peak velocity in Poiseuille flow in a straight tube driven by the same pressure gradient $\hat{G}$. Therefore,

$$D = 4\sqrt{2\delta} Re = 4\sqrt{K}. \tag{2.22}$$

   The Dean number $K$ is suitable for only small $K$ because it depends on the mean velocity which corresponds to the mean pressure gradient in Poiseuille flow. To investigate higher values of the Dean number, it is better to use $D$ because the mean velocity profile deviates too much from the Poiseuille flow profile.

2. **Womersley number** $\alpha$
   The dimensionless parameter expresses the relationship between the unsteady inertia (flow frequency) and the viscous effects.

$$\alpha = a\sqrt{\frac{\omega}{\nu}}, \tag{2.23}$$

   where $\omega$ is a frequency of oscillation.

   The value $\alpha^2$ can be interpreted as a ratio of the frequency of the oscillations of the pressure gradient compared with the viscous rate of diffusion across the boundary layer. Therefore, for small $\alpha$, the viscous effect is large compared to the frequency of the driving oscillatory pressure gradient resulting in viscous flow throughout a tube. For large $\alpha$, the viscosity effect is small compared to the frequency. Therefore, the effect of viscosity is confined in a thin layer around the boundary.
   As mentioned earlier, for large $\alpha$ there are two flow regions in the tube; a boundary layer region on the wall where the viscous effects are important, a potential flow region away from the wall where the viscous effects are negligible leading to a faster flow. The boundary layer has thickness $(\nu/\omega)^{1/2}$. Therefore, $\alpha$ represents the ratio of the radius of the tube to the boundary layer thickness for the half period.

3. **Secondary streaming Reynolds number $R_s$**
   This is the Reynolds number for the secondary flow, which is given by

$$R_s = \frac{\delta W^2 \nu}{\omega a^2}, \tag{2.24}$$

   where $W$ is the dimensionless velocity amplitude that would be driven by a pressure gradient in a straight tube containing an inviscid fluid. It determines the behaviour of the steady secondary flows that are generated in the cross section of the tube when the fluids are driven by the oscillatory pressure gradient. See more details in §2.4.

## 2.3 Fully developed steady flow in a weakly curved tube

We are first interested in the simple case in which the fluid is driven by only a steady constant pressure gradient along the pipe. Setting $\partial\psi/\partial t$, $\partial w/\partial t$ and $R_s$ equal to zero in (2.16) and (2.17), the reduced equations become

$$\frac{1}{r}\left(\frac{\partial\psi}{\partial\theta}\frac{\partial}{\partial r} - \frac{\partial\psi}{\partial r}\frac{\partial}{\partial\theta}\right)\nabla^2\psi - w\left(\sin\theta\frac{\partial w}{\partial r} + \frac{\cos\theta}{r}\frac{\partial w}{\partial\theta}\right) = \nabla^4\psi, \tag{2.25}$$

$$\frac{1}{r}\left(\frac{\partial\psi}{\partial\theta}\frac{\partial w}{\partial r} - \frac{\partial\psi}{\partial r}\frac{\partial w}{\partial\theta}\right) = D + \nabla^2 w. \tag{2.26}$$

We impose the no-slip boundary conditions such that

$$w = \psi = \frac{\partial\psi}{\partial r} = 0 \qquad \text{on} \qquad r = 1. \tag{2.27}$$

We now consider the solutions in three regimes; $D \ll 1, D = O(1)$ and $D \gg 1$.

### 2.3.1 Small $D$

The original work was by Dean who found the solutions analytically using the method of successive approximation. First we assume $D \ll 1$. By inspecting equations (2.25) and (2.26), we can see that the leading-order term for the axial velocity is $O(D)$ and for the streamfunction is $O(D^2)$. So if $D$ is zero, $w$ and $\psi$ must also be zero. We set

$$w \sim D\sum_{n=0}^{\infty} D^{2n} w_n(r,\theta), \tag{2.28}$$

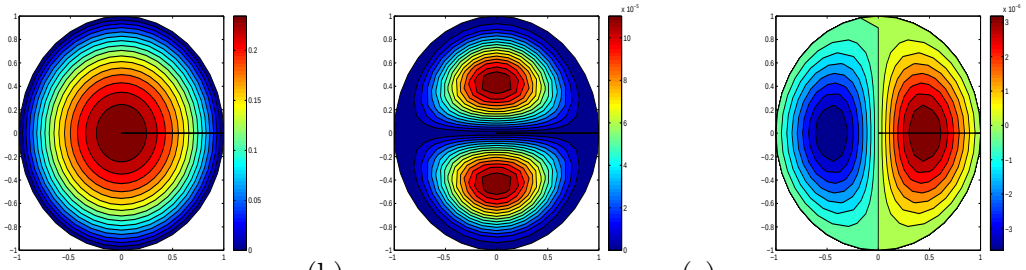
$$\psi \sim \sum_{n=1}^{\infty} D^{2n}\psi_n(r,\theta). \tag{2.29}$$

Note that if $D$ is zero, then the axial velocity and the streamfunction are both zero. Substitution of (2.28) into (2.26), it gives

$$\nabla^2 w_0 = -1. \tag{2.30}$$

Solving (2.30) subject to the no-slip condition, we obtain

$$w_0 = \frac{1}{4}(1 - r^2). \tag{2.31}$$



(a) (b) (c)

Figure 2.4: The sketch of axial velocity contours and secondary flow streamlines for small $D$ (a) $w_0$, (b) $\psi_0$, (c) $w_1$.

The leading order axial velocity is just a Poiseuille flow in a straight tube. By plugging (2.31) into (2.25) and using the expression (2.29), the leading order equation of the streamfunction is then

$$\nabla^4 \psi_1 = \frac{1}{4} r(r^2 - 1) \sin\theta, \tag{2.32}$$

which has a solution

$$\psi_1 = \frac{\sin\theta}{9 \times 8^3} r(4 - r^2)(1 - r^2)^2. \tag{2.33}$$

Equation (2.26) at $O(D^3)$ gives

$$\nabla^2 w_1 = \frac{1}{9 \times 8^3} \left( -r + \frac{9}{4} r^3 - \frac{3}{2} r^5 + \frac{1}{4} r^7 \right) \cos\theta. \tag{2.34}$$

We find that

$$w_1 = \frac{\cos\theta}{45 \times 8^5} r(1 - r^2)(19 - 21r^2 + 9r^4 - r^6). \tag{2.35}$$

**Physical discussion**

The secondary streamlines and the contours of constant axial velocity in cross sectional tube are illustrated in Figure 2.4.

The leading-order secondary flow corresponding to $\psi_1$ consists of a pair of vortices rotating in the opposite direction to one another. They are symmetrical about the line between $\theta = 0$ and $\theta = \pi$. The secondary flow in the central region is directed outward to the outside of the bend (from left to right in Figure 2.4) and replaced by the fluid moving inwards along the wall.

The axial velocity is driven by centrifugal force due to the tube curvature. The no-slip condition causes the axial velocity in the vicinity of the tube centre to be higher than that near the wall. Thus, the fluid at the core experiences a larger centrifugal force ($(\rho w^2)/R$, $w$ is the axial velocity, $\rho$ is the fluid density, $R$ is the curvature radius) compared with the fluid near the wall. This results in *outward centrifuging* in which the fluid moves from the centre to the outside of the bend. The fluid near the outer wall is forced to move inward along the wall of the tube because the pressure at the inner wall is lower than at the outer wall.

The other main feature that Dean was interested in is the relationship between the volume flux ($Q_c$) and the mean pressure gradient. Dean calculated the axial velocity solutions

up to $O(D^9)$ and found that (Berger et al., 1983)

$$\begin{aligned} Q_c &= \int_0^{2\pi}\int_0^1 wr\,dr d\theta \\ &= \frac{\pi D}{8}\left[1 - 0.0306\left(\frac{D}{96}\right)^4 + 0.0120\left(\frac{D}{96}\right)^8 + O(D)^{12}\right], \end{aligned} \tag{2.36}$$

where $\pi D/8 = Q_s$ is the volume flux of the Poiseuille flow in a straight tube. From (2.36), we see that the volume flux in a curved tube has been reduced compared with that in a straight tube. The factor in a square bracket represents a flux decrease due to the curvature. The series (2.36) is sometimes called the *Dean series*. Dean stated that this series is valid up to $D = 96$. By expanding Stokes series, Van Dyke subsequentially extended the Dean series to 24 terms, and confirmed that this series hold without any serious error up to $D = 96$.

Resistance to flow in a curved tube has also been discussed broadly. Many authors examined the curved-flow resistance through the dimensionless *friction factor*, $\lambda$, given by

$$\lambda = \frac{\gamma_c}{\gamma_s} = \frac{Q_s}{Q_c}. \tag{2.37}$$

where $\gamma_c$, $\gamma_s$ are the resistance in curved and straight tubes respectively. White (1929) set up an experiment to examine the resistance in curved and straight tubes. He measured the head loss in both tubes and calculated the resistance coefficients. He calculated the deviation of the resistance-coefficient curve in a curved tube from the resistance-coefficient curve in a straight tube. His results are consistent with the Dean series. In his experiment, he also noticed that turbulent flow through a curved tube does exist with the higher critical Reynolds number than in a straight tube. For example, White found that for $a/R = 1/50$, a laminar flow is retained up to $Re = 6000$, which is more than twice that would be obtained for a straight tube. Both analytical and empirical results show that flows in the curved tube are much more stable than that in the straight tube.

One particular interest for physiologists is the wall shear stress in curved tubes, as it determines prone sites for the development of atherosclerotic plaques. The axial wall shear stress, $\tau_s$, at $r = 1$ is given by

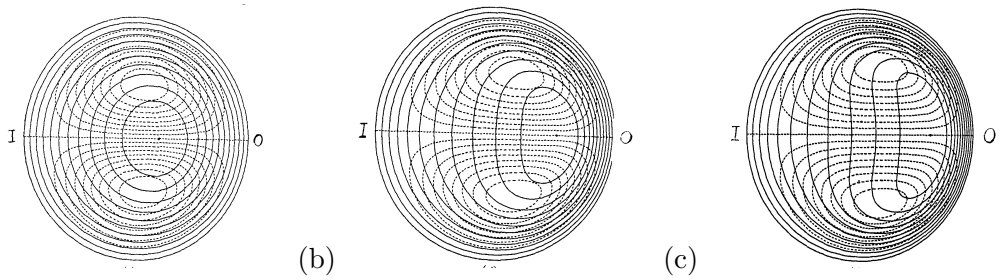
$$\tau_s = -\frac{\partial w}{\partial r} = \frac{1}{2}D + \frac{D^3\cos\theta}{30\times 8^4} + O(D^5) \qquad \text{as} \qquad D \to 0, \tag{2.38}$$

and the azimuthal wall shear stress, $\tau_\theta$, is given by

$$\tau_\theta = -\frac{\partial v}{\partial r} = \frac{D^2\sin\theta}{384} + O(D^4) \qquad \text{as} \qquad D \to 0. \tag{2.39}$$

Hence, the axial wall shear stress increases on the outside of the bend and decreases on the inside.

Siggers & Waters (2005) examined the flow in a curved tube by allowing the tube to have a finite curvature. This case is especially relevant to flow in blood vessels, in particular for the aorta. They introduced a Coriolis effect which is the main contribution to wall shear stress, in addition to the centrifugal forces. The flow behaviour is governed by two dimensionless parameters: the dimensionless curvature ratio $\delta = a/R$ where $a$ is the radius of the constant circular cross section, and $R$ is the radius of curvature of the planar centerline, and the Dean number $D$. The solutions $w$ and $\psi$ are expanded asymptotically in




(a) (b) (c)

Figure 2.5: This diagram showing the streamlines (dashed lines) and the contours of constant axial velocity component (solid lines): (a) D=96, $w_m$=23.4, $\psi_m = 0.95$, (b) D=303.58, $w_m = 60, \psi_m = 3.83$,(c) D=605.72, $w_m = 98.5, \psi_m = 6.81$ where $w_m$ and $\psi_m$ are the maximum axial velocity and streamline function respectively. O and I denote the outer and inner of the bend respectively. Reproduced from McConalogue & Srivastava (1968).

terms of $D$ and $\delta$. They found that the maximum values of the axial velocity and streamlines move toward the outside of the bend as $D$ increases. In contrast, as $\delta$ increases, they move toward the inside of the bend. The results were verified numerically.

The authors were particularly interested in the effect of finite curvature on the wall shear stress. For $\delta$ less than a certain critical value which is in terms of $D$, they showed that the maximal value of $\tau_s$ is attained at the outside of the bend and decreases as $\delta$ increases; however, above the critical value of $\delta$, the maximal value of $\tau_s$ is attained at the inside of the bend and increases for increasing $\delta$. Another feature of their results is the maximal value of $\tau_\theta$. The positions where the maximum value of $\tau_\theta$ is obtained moves toward the inside of the bend as $\delta$ increases, and toward the outside as $D$ increases. Comparing the magnitudes of $\tau_s$ and $\tau_\theta$, it is found that $\tau_s$ is everywhere greater than $\tau_\theta$ for small $D$.

### 2.3.2 Intermediate $D$

In the range of $D$ between 100 and 1000, work has been done by solving the full nonlinear equations (2.16) and (2.17) with various numerical approaches. However, in this section, we review only the two main work done by McConalogue & Srivastava (1968) and Collins & Dennis (1975) because work done by other researchers (Greenspan, 1973; Truesdell & Adler, 1970) has a same flow patterns.

McConalogue & Srivastava (1968) expanded $\psi$ and $w$ in terms of Fourier series, and then solved (2.16) and (2.17) numerically for a particular Dean number from 96 to 605.72 by using an iterative method. Collins & Dennis (1975) found the solutions by using a finite-difference scheme for the range of $D$ between 96 and 5000. The results obtained by McConalogue & Srivastava (1968), and Collins & Dennis (1975) have been agreed for particular values of $D$. Collins & Dennis (1975) suggested a flow model for larger $D$ in which the solution of $w$ consists of an inviscid core with an infinitesimally thin boundary layer near a wall. They also investigated the solutions for $D \to \infty$, which will be discussed in §2.3.3.

Figure 2.5 shows the plots of the streamline function $\psi$ and axial velocity contours $w$ for three values of the Dean number $D$. Ten lines for $w$ and eight lines for $\psi$ were drawn mechanically by using CALCOMP Plotter. The maximum value of $w$, $w_m$, is shifted from the centre of the cross-section to the outside of the wall as $D$ increases. The boundary layers appear to develop at the outer wall at high intermediate Dean number due to the high shear.

Consequently, the centrifugal force which drives the secondary flow has a greater value on the outer wall. McConalogue & Srivastava (1968) found that the ratio between the flux in a curved tube ($Q_c$) and the flux in a straight tube ($Q_s$) is proportional to $1/D$ for large $D$ based on the Fourier series method, as shown in Figure 2.6.

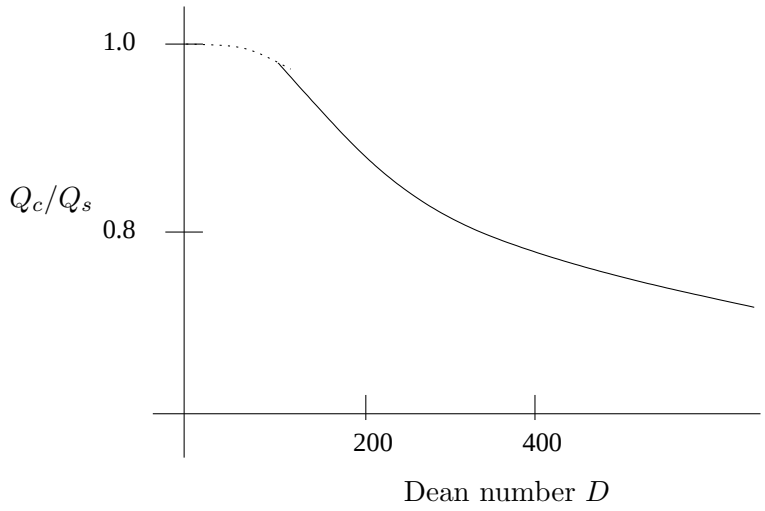



Figure 2.6: The plot of the flux ratio $Q_c/Q_s$ against $D$, the dotted line satisfies the Dean's series up to $D = 96$, and the continuous line satisfies equation $Q_c/Q_s = 16D^{-1}\int_0^1 rw_0\,dr$. Reproduced from McConalogue & Srivastava (1968).

### 2.3.3 Large $D$

There have been numerous theories developed for flows at large Dean number. A clearer picture is emerging of how the fluid flows in this range of Dean number, but we still have not obtained a comprehensive characterization of the flow because different results have been obtained. Mostly, the problem has been solved numerically by discretizing the equations (2.25) and (2.26) using the finite-difference method, and then various methods have been employed for solving the discretized problem such as the spectral method.

The numerical results by Collins & Dennis (1975) suggested that the structure of the solution for large $D$ is that of an inviscid core surrounded by a boundary layer. For large $D$, we assume that the axial velocity and the streamline function at the boundary are scaled (Pedley, 1980)

$$w \sim D^{\alpha}, \qquad \psi \sim D^{\beta} \tag{2.40}$$

and that the boundary-layer thickness is of $O(D^{-\gamma})$.
In the core, the inertial terms balance the pressure gradient terms in (2.26), which gives

$$\alpha + \beta = 1. \tag{2.41}$$

In the boundary layer, the inertial terms in (2.25) and (2.26) must balance the viscous terms and centrifugal terms. The balance from (2.25) gives

$$\beta + 4\gamma = 2\beta + 3\gamma = 2\alpha + \gamma, \tag{2.42}$$

and from (2.26) gives

$$\alpha + 2\gamma = \alpha + \beta + \gamma, \tag{2.43}$$

so that $\beta = \frac{1}{3}, \gamma = \frac{1}{3}, \alpha = \frac{2}{3}$. Thus, we define the scaled variables

$$w = D^{2/3}\bar{w}, \qquad \psi = D^{1/3}\bar{\psi}, \tag{2.44}$$

and a radial coordinate for boundary layer

$$\zeta = D^{1/3}(1 - r). \tag{2.45}$$

At leading order the flow in the core is governed by

$$\bar{w}\left(\sin\theta\frac{\partial\bar{w}}{\partial r} + \frac{\cos\theta}{r}\frac{\partial\bar{w}}{\partial\theta}\right) = 0, \tag{2.46}$$

$$\frac{1}{r}\left(\frac{\partial\bar{\psi}}{\partial\theta}\frac{\partial\bar{w}}{\partial r} - \frac{\partial\bar{\psi}}{\partial r}\frac{\partial\bar{w}}{\partial\theta}\right) = 1. \tag{2.47}$$

To solve (2.46) and (2.47), we need to transform polar coordinates $(r, \theta)$ to Cartesian coordinates $(x, y)$ . The relation between these two sets of variables with $x$ and $y$ expressed in terms of $r$ and $\theta$ is

$$x = r\cos\theta, \qquad y = r\sin\theta, \tag{2.48}$$

whereas

$$r^2 = x^2 + y^2, \qquad \theta = \tan^{-1}\frac{y}{x}. \tag{2.49}$$

By the chain rule, we have

$$\frac{\partial}{\partial y} = \frac{\partial}{\partial r}\frac{\partial r}{\partial y} + \frac{\partial}{\partial\theta}\frac{\partial\theta}{\partial y} = \sin\theta\frac{\partial}{\partial r} + \frac{\cos\theta}{r}\frac{\partial}{\partial\theta}. \tag{2.50}$$

We then have

$$\frac{\partial\bar{w}}{\partial y} = 0, \tag{2.51}$$

which gives

$$\bar{w} = w_c(r\cos\theta), \tag{2.52}$$

where $w_c$ is an arbitrary function. Substitution of (2.52) into (2.47) gives

$$\bar{\psi} = \frac{r\sin\theta}{w_c'(r\cos\theta)}. \tag{2.53}$$

In the boundary layer, the leading-order equations are given by

$$\frac{\partial^2\bar{w}}{\partial\zeta^2} + \frac{\partial\bar{\psi}}{\partial\theta}\frac{\partial\bar{w}}{\partial\zeta} - \frac{\partial\bar{\psi}}{\partial\zeta}\frac{\partial\bar{w}}{\partial\theta} = 0, \tag{2.54}$$

$$\frac{\partial^4\bar{\psi}}{\partial\zeta^4} + \left(\frac{\partial\bar{\psi}}{\partial\theta}\frac{\partial}{\partial\zeta} - \frac{\partial\bar{\psi}}{\partial\zeta}\frac{\partial}{\partial\theta}\right)\frac{\partial^2\bar{\psi}}{\partial\zeta^2} = \sin\theta\bar{w}\frac{\partial\bar{w}}{\partial\zeta}. \tag{2.55}$$

The no-slip boundary conditions (2.27) are unchanged, *i.e.*

$$\bar{\psi} = \frac{\partial\bar{\psi}}{\partial\zeta} = \bar{w} = 0 \qquad \text{on} \qquad \zeta = 0. \tag{2.56}$$

The matching condition is given by

$$\frac{\partial \bar{\psi}}{\partial \zeta} \to 0, \qquad \bar{w} \to w_c(\cos\theta) \qquad \text{as} \qquad \zeta \to \infty. \tag{2.57}$$

Integrating equation (2.55) once with respect to $\zeta$ and applying (2.57), we obtain

$$\frac{\partial^3 \bar{\psi}}{\partial \zeta^3} + \frac{\partial \bar{\psi}}{\partial \theta}\frac{\partial^2 \psi}{\partial \zeta^2} - \frac{\partial \bar{\psi}}{\partial \zeta}\frac{\partial^2 \bar{\psi}}{\partial \zeta \partial \theta} = -\frac{1}{2}\sin\theta[w_c^2(\cos\theta) - \bar{w}^2]. \tag{2.58}$$

Ito (1987) found the approximate solution to the boundary layer equations (2.54) and (2.55) by defining the definite region of boundary layer and integrating the boundary layer equations across the boundary layer. This method is called *the Pohlhausen momentum integral method*. Ito was able to calculate the function $w_c(\cos\theta)$ and found that the thickness of the boundary layer remains roughly constant until $\theta = \pi$ where the thickness increases sharply. This result was confirmed by the numerical results of Collins & Dennis (1975), and of Siggers & Waters (2005) for finite curvature.

Ito (1987) also found that the friction factor $\lambda$ is proportional to $D^{1/2}$ which agrees well with Adler (1934), Mori & Nakayama (1965), and Collins & Dennis (1975). This result is in contrast to the result of Van Dyke (1978) in which he found $\lambda \propto D^{1/4}$. Van Dyke (1978) described the discrepancy between his analytical results and the numerical results from other authors as being due to the inadequacy of mesh refinement for large $D$. However, there is an interesting insight here. If both scalings for $\lambda$ are correct, it means that the solution for large $D$ is non-unique.

Dennis & NG (1982) used a similar numerical method to McConalogue & Srivastava (1968) for large D to establish the existence of a four-vortex solution for $D > D_c$, where $D_c = 956$, as can be seen in Figure 2.7. A four-vortex flow was also observed experimentally by flow visualization in a semicircular tubes. This comfirmed the existence of multiple steady-state solutions for large $D$.

The stability characteristics of the two- and four-vortex solutions were first considered by Daskopoulos & Lenhoff (1989). The two-vortex solutions are the primary solutions and are unconditionally stable, whereas the four-vortex solutions which can be observed computationally suggests that they are stable.

However, based on the discussion of generic properties of flow bifurcation by Benjamin (1978), Daskopoulos & Lenhoff postulated that there must be at least one additional family of solutions that is unstable and this family of solutions joins up with the stable four-vortex solutions at the bifurcation point at $D \approx 956$, *i.e.* a saddle-node bifurcation forms. To prove their hypothesis, they restricted to symmetric disturbances only. The orthogonal collocation technique was chosen and the solutions were in terms of Fourier Series due to the periodic problem. The unstable four-vortex solutions were shown. On the branch of stable four-vortex solutions, the vortex is approximately constant across the parameter space, whereas on the branch of unstable four-vortex solution, the vortex shrinks and tends to deform to stable two-vortex solutions. In addition, Daskopoulos & Lenhoff (1989) found two further unstable branches of solutions which appear at $D \approx 2494$. Figure 2.7 illustrates the bifurcation of multiple branches of steady-state solutions with the streamlines for each type shown. Daskopoulos & Lenhoff also attempted to find the next turning point up to $D \approx 35000$, but there seems to be no sign of the next one. Their work is beneficial in some aspects but they noted that their analysis is not physically applicable due to their assumption of symmetrical disturbances.

Yanase et al. (1989) filled the gap of Daskopoulos & Lenhoff (1989) by examing the stability of steady-state flows in reaction to both symmetrical and asymmetrical disturbances by means of the spectral method. They solved for $956 \leqslant D \leqslant 10000$, and found that the two-vortex solutions are always stable, whereas the four-vortex solutions are unstable in response to both symmetrical and asymmetrical disturbances. Their unstable four-vortex solutions subject to symmetrical disturbances corresponds to one of three branches of unstable four-vortex solutions in Figure 2.7. Yanase et al. (1989) investigated the time evolution of the four-vortex flows subject to asymmetric disturbances, as illustrated in Figure 2.8. At the early stage, the symmetric four-vortex solution is developed and subsequently changes into asymmetric four-vortex solution. Finally, the flow turns into stable two-vortex flow.

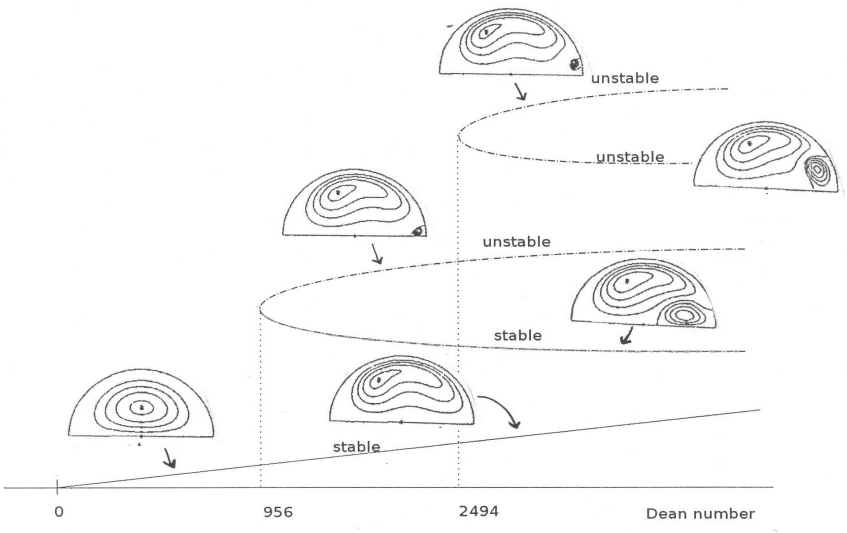



Figure 2.7: Bifurcation diagram for various Dean number. The continuous line represents the stable solutions, and the dot-dashed line represents unstable solutions. The first turning point is when $D = 956$, and the second turning point is when $D = 2494$. Reproduced from Daskopoulos & Lenhoff (1989).

Siggers & Waters (2005) considered steady flows in tubes with finite curvature for large $D$ both numerically and asymptotically. Their main focus is on the values of wall shear stress, both $\tau_\theta$ and $\tau_s$, which are a key feature to determine sites where atherosclerosis develops. Following Ito's analysis for large $D$, asymptotic solutions are found by means of Pohlhausen momentum integral method. They verified the singular point at $\theta = \pi$ where the thickness of boundary layer becomes large and the boundary layer approximation breaks down. This phenomenon is independent of the values of $\delta$.

According to Figure 2.7, the secondary streamlines of solutions on the lowest branch have only two vortices, whereas solutions on other branches have four vortices. Siggers & Waters (2005) investigated the two stable branches only, and found that the critical Dean number $D_c$ increases significantly as $\delta$ increases, from $D_c \approx 956$ at $\delta = 0$ to $D_c \approx 1510$ at $\delta = 0.3$. By comparing the stable two-vortex branch and the stable four-vortex branch, the solutions of $\tau_\theta$ and $\tau_s$ take similar values on both branches, except at $\theta = 0$ on the stable two-vortex branch, $\tau_s$ is globally maximum, whilst on the stable four-vortex branch, $\tau_s$ has a local minimum there with the value of approximately half that on the stable two-vortex

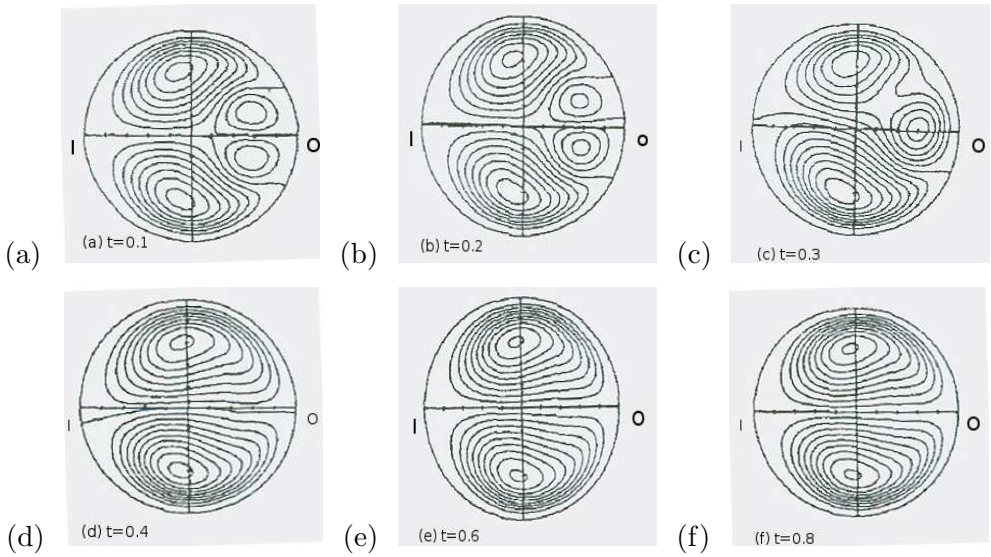



Figure 2.8: The diagram showing the time evolution of the secondary streamlines of the perturbed four-vortex solution at $D = 1000$. Reproduced from Yanase et al. (1989).

branch. An increase in $\delta$ decreases the maximum values of $\tau_\theta$ and $\tau_s$, leading to a decrease in the variation of the overall wall shear stress.

## 2.4 Fully developed unsteady flow in a weakly curved tube

### 2.4.1 Purely oscillatory flows: sinusoidal flows

The unsteady viscous flow in a curved tube was first considered by Lyne (1971). Lyne investigated oscillatory flows with zero mean pressure gradient *i.e.* when $D = 0$ in (2.17). Solutions to the governing equations (2.16) and (2.17) can be found corresponding to the size of the Womersley number $\alpha$, and the secondary streaming Reynolds number $R_s$.

As explained in §2.2.1, $\alpha^2$ is a ratio of the frequency of the oscillations of the pressure gradient compared with the viscous rate of diffusion across the boundary layer. Therefore, if $\alpha$ is small, the viscosity dominates the oscillatory pressure gradient effects. In contrast, if $\alpha$ is large, the viscosity is small compared to the frequency and so the viscous effects are confined to the boundary layer adjacent to the tube wall.

For large $\alpha$, we will rely heavily on Lyne's analysis together with some inferences from Pedley (1980). Lyne considered flows when $\alpha$ becomes sufficiently large that the centrifugal force generates a secondary flow in the Stokes layer as well as in the core. The steady streaming flow in the core is governed by the parameter $R_s$. Mullin & Greated (1980) investigated intermediate values of $\alpha$, and found that the direction of the streamline patterns is outward centrifuging for $0 \leq \alpha \leq 10$ , and becomes inward centrifuging for $\alpha$ greater than 10. They concluded that the development of a reverse secondary flow and Stokes boundary layer gradually take place when $\alpha \gg 10$ .

#### 2.4.1.1 Low-frequency pressure gradient ( $\alpha \ll 1$ )

In the case where the flow is driven by an oscillatory pressure gradient with a small frequency $\alpha$, the viscous effect becomes dominant everywhere. By balancing the viscous term and the

oscillatory pressure gradient term in (2.17) and expanding the the axial velocity in terms of powers of $\alpha$ (assuming that $R_s = O(1)$), we write

$$w \sim \alpha^3 w_0 + \alpha^4 w_1 + \alpha^5 w_2 + \cdots, \tag{2.59}$$

so that

$$\psi \sim \alpha^6 \psi_0 + \alpha^7 \psi_1 + \alpha^8 \psi_2 + \cdots. \tag{2.60}$$

Substituting (2.59)–(2.60) into (2.16)–(2.17) implies that

$$\nabla^2 w_0 = -\sqrt{2R_s}\cos\tau, \tag{2.61}$$

$$\nabla^2 w_1 = 0, \tag{2.62}$$

$$\nabla^2 w_2 = \frac{\partial w_0}{\partial \tau}. \tag{2.63}$$

The leading-order axial flow (corresponding to $w_0$) is driven by the interaction between the viscous effects and the oscillating pressure gradient, whereas the third-order axial flow (corresponding to $w_2$) is driven by the interaction between the viscous and inertial effects. Applying the no-flux boundary condition $w_0 = w_1 = w_2 = 0$ on $r = 1$ gives

$$w_0 = \frac{1}{4}\sqrt{2R_s}(1 - r^2)\cos\tau, \tag{2.64}$$

$$w_1 = 0, \tag{2.65}$$

$$w_2 = \frac{1}{64}\sqrt{2R_s}(3 - r^2)(1 - r^2)\sin\tau. \tag{2.66}$$

The leading-order axial flow $w_0$ is in fact a (quasi-steady) Poiseuille flow (parabolic in shape) as a result of the balance between the viscous term and the oscillatory pressure gradient term. The solutions of $w_2$ arises from the interaction of the time-derivative inertial term and the viscous term. $w_0$ and $w_2$ are out of phase, and so, for $\pi/2 \le \tau \le \pi$ and $3\pi/2 \le \tau \le 2\pi$, the leading-order axial velocity is slowed down by the effect of inertia from $w_2$ which acts as to delay the fluid.

Similarly, for a streamfunction, we obtain the expressions

$$\nabla^4 \psi_0 = -w_0 \left( \sin\theta \frac{\partial w_0}{\partial r} + \frac{1}{r}\cos\theta \frac{\partial w_0}{\partial \theta} \right), \tag{2.67}$$

$$\nabla^4 \psi_1 = -w_0 \left( \sin\theta \frac{\partial w_1}{\partial r} + \frac{1}{r}\cos\theta \frac{\partial w_1}{\partial \theta} \right) - w_1 \left( \sin\theta \frac{\partial w_0}{\partial r} + \frac{1}{r}\cos\theta \frac{\partial w_0}{\partial \theta} \right), \tag{2.68}$$

$$\begin{aligned} \nabla^4 \psi_2 = & -w_0 \left( \sin\theta \frac{\partial w_2}{\partial r} + \frac{1}{r}\cos\theta \frac{\partial w_2}{\partial \theta} \right) \\ & -w_1 \left( \sin\theta \frac{\partial w_1}{\partial r} + \frac{1}{r}\cos\theta \frac{\partial w_1}{\partial \theta} \right) - w_2 \left( \sin\theta \frac{\partial w_0}{\partial r} + \frac{1}{r}\cos\theta \frac{\partial w_0}{\partial \theta} \right). \end{aligned} \tag{2.69}$$

All of the terms in these expansions results from the interaction between the viscous effects and the centrifugal force. By solving (2.67)–(2.69) subject to the boundary conditions

$$\psi_i = \frac{\partial \psi_i}{\partial r} = 0 \qquad \text{on} \qquad r = 1 \qquad \text{for} \qquad i = 0, 1, 2, \tag{2.70}$$

we obtain

$$\psi_0 = \frac{1}{16 \times 144} R_s r (1 - r^2)^2 (1 - \frac{1}{4} r^2) \sin\theta (1 + \cos 2\tau), \tag{2.71}$$

$$\psi_1 = 0, \tag{2.72}$$

$$\psi_2 = \frac{1}{2} R_s \left( -\frac{25}{6} r + 7r^3 - \frac{10}{3} r^5 + \frac{1}{2} r^7 \right) \sin\theta \sin 2\tau. \tag{2.73}$$

Since

$$u = \frac{1}{r}\frac{\partial \psi}{\partial \theta}, \tag{2.74}$$

the leading-order radial velocity $u$ is positive on the outside of the bend (near $\theta = 0$), and negative on the inside (near $\theta = \pi$). Thus, for a small $\alpha$, the streamline patterns are similar to the steady flow for small Dean number in the sense that the fluid flows from the inside to the outside of the bend.

#### 2.4.1.2 High-frequency pressure gradient ($\alpha \gg 1$)

At large $\alpha$, the core flow is surrounded by a Stokes layer of dimensionless thickness of $O(1/\alpha)$ on the boundary $r = 1$. By the no-slip conditions, the centrifugal force decreases as it moves toward the wall boundary, whilst the pressure gradient force remains unchanged. Therefore, the centrifugal term will balance with inertia and viscous terms in the Stokes layer. This interaction in the Stokes layer results in an oscillatory secondary motion, primarily consisting of a $\theta-$component of velocity, $v$. As the centrifugal-force term is proportional to $w^2$ and $w$ oscillates at the fundamental frequency, so a $\theta-$component of velocity, $v$, will contain an oscillation with both double the fundamental frequency, and a mean flow (see (2.87) ). This mean flow can not tend to zero at the edge of the Stokes layer due to the no-slip conditions, and therefore it drives a non-zero mean secondary motion (steady streaming) outside the Stokes layer. The flow outside the Stokes layer is characterized by the secondary streaming Reynolds number $R_s$.

The effect of viscosity can be neglected in the core, so the balance between the $t-$derivative inertial term and the oscillatory pressure gradient term in (2.17) gives

$$w = \alpha\sqrt{2R_s}\sin\tau. \tag{2.75}$$

By balancing the inertial term and the centrifugal term in (2.16), we find that an appropriate expansion for $\psi$ is given by

$$\psi \sim \psi_0 + \frac{1}{\alpha}\psi_1 + \frac{1}{\alpha^2}\psi_2 + \cdots. \tag{2.76}$$

In the Stokes layer, Lyne (1971) introduced the new variables $\eta, \Psi, W$ such that

$$\eta = \frac{\alpha}{\sqrt{2}}(1 - r), \qquad \Psi = \alpha\psi, \qquad W = \frac{1}{\alpha}w, \tag{2.77}$$

and sought the asymtotic solutions of the form

$$W = W_0 + O(\alpha^{-1}), \qquad \Psi = \Psi_0 + O(\alpha^{-1}). \tag{2.78}$$

Therefore, the matching condition for the axial velocity is given by

$$\lim_{\eta\to\infty}(\alpha W_0 + W_1 + \cdots) = w\big|_{r=1}. \tag{2.79}$$

Matching the streamline function requires

$$\lim_{\eta\to\infty}(\frac{1}{\alpha}\Psi_0 + \frac{1}{\alpha^2}\Psi_1 + \cdots) = \psi_0\big|_{r=1}, \tag{2.80}$$

and matching the azimuthal velocity requires

$$\lim_{\eta\to\infty}\left(\frac{1}{\sqrt{2}}\frac{\partial\Psi_0}{\partial\eta}\right) = -\frac{\partial\psi_0}{\partial r}\big|_{r=1}. \tag{2.81}$$

The no-slip boundary conditions are imposed on $\eta = 0$ and the solutions must match the core flow as $\eta \to \infty$, *i.e.*

$$W_0 = 0, \Psi_0 = \frac{\partial\Psi_0}{\partial\eta} = 0 \qquad \text{on} \qquad \eta = 0, \tag{2.82}$$

$$W_0 \to \sqrt{2R_s}\sin\tau \qquad \text{as} \qquad \eta\to\infty. \tag{2.83}$$

At leading order of the Stokes-layer equations (2.17) and (2.16) become

$$\frac{1}{2}\frac{\partial^2 W_0}{\partial\eta^2} - \frac{\partial W_0}{\partial\tau} = -\sqrt{2R_s}\cos\tau, \tag{2.84}$$

$$\frac{1}{2}\frac{\partial^4\Psi_0}{\partial\eta^4} - \frac{\partial^3\Psi_0}{\partial\eta^2\partial\tau} = \sqrt{2}\sin\theta W_0\frac{\partial W_0}{\partial\eta}. \tag{2.85}$$

The solution of (2.84) that satisfies (2.82)–(2.83) is given by

$$W_0 = \sqrt{2R_s}[\sin\tau - e^{-\eta}\sin(\tau-\eta)]. \tag{2.86}$$

Substituting (2.86) into (2.85) and solving subject to the boundary conditions in (2.82), we find that

$$\begin{aligned}\Psi_0 = {} & \sqrt{2}R_s\sin\theta\left[\frac{5}{8} - \frac{1}{4}\eta - \frac{1}{8}e^{-2\eta} - \frac{1}{\sqrt{2}}e^{-\eta}\cos\left(-\eta+\frac{\pi}{4}\right)\right.\\ & +\frac{1}{8\sqrt{2}}(9-5\sqrt{2})\cos\left(2\tau+\frac{\pi}{4}\right) - \frac{1}{8\sqrt{2}}e^{-2\eta}\cos\left(2\tau-2\eta+\frac{\pi}{4}\right)\\ & \left.-\frac{1}{\sqrt{2}}e^{-\eta}\cos\left(2\tau-\eta+\frac{\pi}{4}\right) + \frac{5}{8}e^{-2\eta}\cos\left(2\tau-2\eta+\frac{\pi}{4}\right)\right]\\ & +B(\theta)\eta^2 + C(\theta)\eta^3,\end{aligned} \tag{2.87}$$

where $B(\theta)$ and $C(\theta)$ are arbitrary functions of $\theta$.

By the matching method, $B(\theta)$ and $C(\theta)$ are both equal to 0, so that, as $\eta\to\infty$, $\Psi_0$ is given by

$$\Psi_0 \sim \sqrt{2}R_s\sin\theta\left[\frac{5}{8} - \frac{1}{4}\eta + \frac{1}{8\sqrt{2}}(9-5\sqrt{2})\cos\left(2\tau+\frac{\pi}{4}\right)\right], \tag{2.88}$$

$$\frac{\partial\Psi_0}{\partial\eta} \to -\frac{R_s\sin\theta}{2\sqrt{2}}. \tag{2.89}$$

The mean flow expression for $\Psi_0$ does not tend to zero at the edge of the Stokes layer. It drives a secondary flow in the core, as follows.

In the core, the governing equations are given by

$$\frac{\partial\nabla^2\psi_0}{\partial\tau} = 0, \tag{2.90}$$

$$\frac{\partial\nabla^2\psi_1}{\partial\tau} = 0, \tag{2.91}$$

$$\frac{\partial\nabla^2\psi_2}{\partial\tau} = \nabla^4\psi_0 + \frac{1}{r}\left(\frac{\partial\psi_0}{\partial r}\frac{\partial}{\partial\theta} - \frac{\partial\psi_0}{\partial\theta}\frac{\partial}{\partial r}\right)\nabla^2\psi_0. \tag{2.92}$$

Since $\nabla^2\psi_0$ is independent of $t$, $\psi_0$ can be expressed as

$$\psi_0 = \psi_0^{(u)}(r,\theta,\tau) + \psi_0^{(s)}(r,\theta), \tag{2.93}$$

where $\psi_0^{(s)}$ is steady part and $\psi_0^{(u)}$ is periodic with zero mean and satisfies

$$\nabla^2\psi_0^{(u)} = 0, \tag{2.94}$$

and matching to (2.89) leads to $\psi_0^{(u)} = 0$ because the $\tau$-dependent term in (2.89) is small and becomes effective at higher order in $\alpha^{-1}$ only. Now at the leading order of (2.92), $\psi_0^{(s)}$ satisfies

$$\nabla^4\psi_0^{(s)} + \frac{1}{r}\left(\frac{\partial\psi_0^{(s)}}{\partial\theta}\frac{\partial}{\partial r} - \frac{\partial\psi_0^{(s)}}{\partial r}\frac{\partial}{\partial\theta}\right)\nabla^2\psi_0^{(s)} = 0, \tag{2.95}$$

which is to be solved subject to the boundary conditions

$$\psi_0^{(s)} = 0, \qquad \frac{\partial\psi_0^{(s)}}{\partial r} = \frac{1}{4}R_s\sin\theta \qquad \text{on} \qquad r = 1. \tag{2.96}$$

which are derived by matching with (2.89).

Lyne let $\psi_0^{(s)} = R_s\chi_0$ where $\chi_0$ satisfies

$$\frac{1}{R_s}\nabla^4\chi_0 + \frac{1}{r}\left(\frac{\partial\chi_0}{\partial r}\frac{\partial}{\partial\theta} - \frac{\partial\chi_0}{\partial\theta}\frac{\partial}{\partial r}\right)\nabla^2\chi_0 = 0 \tag{2.97}$$

subject to

$$\chi_0 = 0, \qquad \frac{\partial\chi_0}{\partial r} = \frac{1}{4}\sin\theta \qquad \text{on} \qquad r = 1. \tag{2.98}$$

Equation (2.97) is the steady, two-dimensional Navier Stokes equation, in which $R_s$ plays the role of the conventional Reynolds number. Lyne further solved equations in the limits of small and large $R_s$.

For small $R_s$, the problem reduces to a Stokes flow problem with the solution

$$\chi_0 = -\frac{1}{8}r(1-r^2)\sin\theta - \frac{R_s}{3072}r^2(1-r^2)^2\sin 2\theta + O({R_s}^2), \tag{2.99}$$

as $R_s \to 0$. This shows that the steady secondary streaming flow moves across the cross section from the outside to the inside of the wall. This is in the opposite direction to the secondary flow in a tube when the flow is driven by a steady axial pressure gradient. This is *inward centrifuging*, as illustrated in Figure 2.9. Lyne also verified this result experimentally.

When $R_s$ is large, the effect of viscosity is confined in a boundary layer of thickness of $O({R_s}^{-1/2})$ near $r = 1$. Lyne postulated that the fluid in the boundary layer, having started at $\theta = \pi$ and reached $\theta = 0$, meets the fluid from the other semicircle at $\theta = 0$. These combined fluids erupt across the cross section generating a cross-sectional internal layer of thickness of $O({R_s}^{-1/2})$. While the bulk of the core fluid is inviscid, the streamlines are closed resulting in uniform vorticities in the core and of opposite sign in the two regions. Since the vorticities are not continuous along the plane of symmetry($\theta = 0, \pi$), so to smooth out this discontinuity, an internal layer of thickness of $O({R_s}^{-1/2})$ forms along the plane of symmetry, as illustrated in Figure 2.10.

Siggers & Waters (2008) investigated the effect of finite curvature on the flow driven by a sinusoidal pressure gradient using a pseudospectral code. They identified three distinct

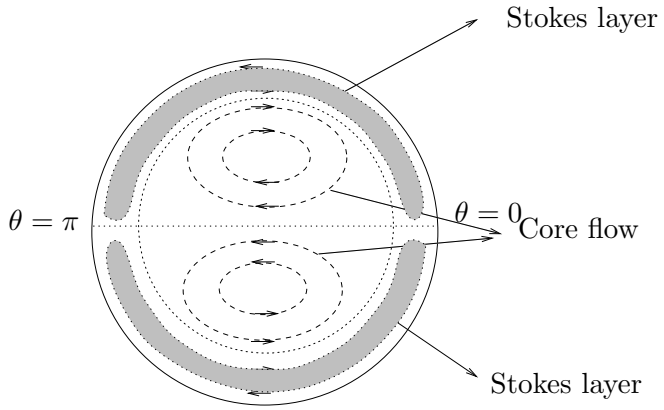



Figure 2.9: The diagram showing the secondary core flow at large $\alpha$, small $R_s$

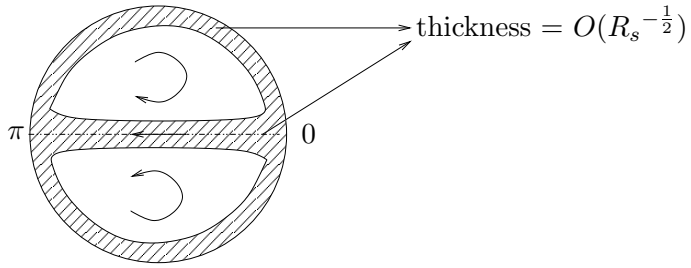



Figure 2.10: Sketch of the flow for large $\alpha$, and large $R_s$. The shaded region is the boundary layer region, and the unshaded region is the core flow.

classes of stable solution: (1) $2\pi-$periodic symmetric (branch 1); (2) $2\pi-$periodic and asymmetric (branch 2); and (3) asymmetric solutions that are not $2\pi-$periodic (branch 3), as shown in Figure 2.11. The vertical axis (not to scale) denotes the value of a solution property on a Poincaré section at time intervals of $2\pi$. The transition between the solutions is sensitive to the value of $\delta$. For example, for $\delta$ less than a certain value, the branch 1 solutions lose stability and undergo the transition to branch 2 solutions. Conversely, if $\delta$ greater than this value, the branch 1 solutions undergo the transition to branch 3 and when $R_s$ increases, they undergo further transitions to branch 2 solutions.

When $\alpha$ increases, the numerical solutions are in case (1). Figure 2.12 shows the periodic and symmetric solutions for $R_s = 300$, $\alpha = 20$ with $\delta = 0$ and $\delta = 0.3$. The boundary layer exists. As time increases, the vorticity tends to develop at the core. An increase in $\delta$ induces the thinner boundary layer at the inside of the bend.

### 2.4.2 Oscillatory flows with non-zero mean pressure gradient: oscillatory flows

From the physiological point of view, this case has been the center of the interest due to its practically realistic application since flow in large arteries are pulsatile with non-zero mean pressure gradient. For the aortic vessels, the typical flows have the mean $D$ from $300 - 500$, and for peak $D \approx 1500 - 2500$, $\alpha \approx 10 - 20$, and $R_s \approx 4000$ (Pedley, 1980). Due to the nonlinearity of the problem, the parameters $D, \alpha$ and $R_s$ can not be treated separately.

The most extensive work was given by Smith (1975) who analysed many different regimes. Nevertheless, conditions within blood vessels are not in the range of his pertur-

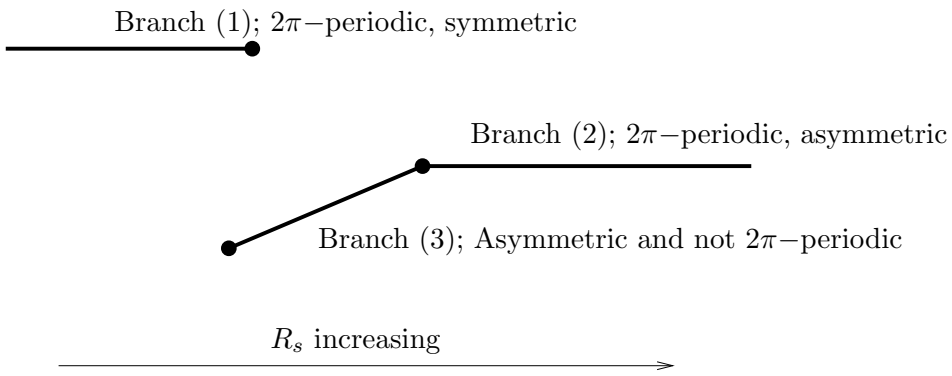



Figure 2.11: Sketch of three distinct classes of stable solutions and unstable solution branches are not presented when $\delta$ is greater than 0.7 (the critical value). The vertical axis (not to scale) denotes the value of a solution property on a Poincaré section at time intervals of $2\pi$. Reproduced from Siggers & Waters (2008).

bation analysis. The most physiologically relevant work has been made by Blennerhassett (1976), who studied the case in which $\alpha \to \infty$, and $D \lesssim R_s$.

He assumed that the thinnest boundary layer is the Stokes layer and then focused on the steady streaming flows at the core driven by the mean pressure gradient and slip velocity from the edge of the Stokes layer. His analysis was fairly similar to Lyne's calculation (as described in §2.4.1.2) except he added the steady component of the flow, $w_1$, into the core axial flow, *i.e.*

$$w = \alpha\sqrt{2R_s}\sin\tau + w_1 + O(\alpha^{-1}) \qquad \text{as} \qquad \alpha \to \infty, \tag{2.100}$$

the stream function again being written as

$$\psi \sim \psi_0 + \frac{1}{\alpha}\psi_1 + \cdots, \tag{2.101}$$

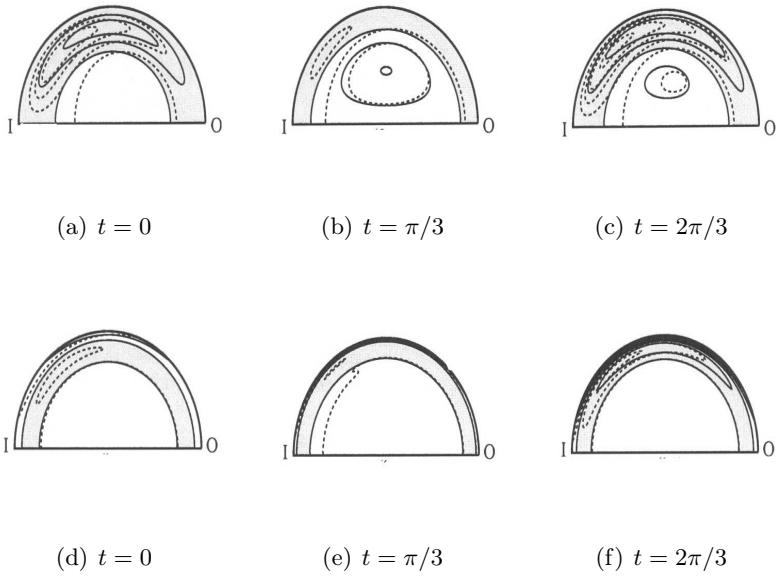
where $\psi_0$ is the steady part of $\psi$. He then took the limit $R_s \to \infty$, with $D = o(R_s)$. He used the same approach as in Lyne's analysis by letting $\psi_0 = R_s\chi$. His analytical result is similar to the purely oscillatory flow developed by Lyne, in which the uniform vorticities in the inviscid core regions are separated by a boundary layer of thickness of $O({R_s}^{-1/2})$ across the tube. Blennerhassett showed that if $w_1 = O(D/R_s)$, the solution of $w_1$ is not a single-valued function of position. Thus, he let $w_1 = O(D)$ so that $w_1$ in the core satisfies

$$\frac{\partial\chi_0}{\partial\theta}\frac{\partial w_1}{\partial r} - \frac{\partial\chi_0}{\partial r}\frac{\partial w_1}{\partial\theta} = 0. \tag{2.102}$$

By (2.15) and the definition of $\chi$, (2.102) can be written as

$$(\boldsymbol{u}\cdot\boldsymbol{\nabla})w_1 = 0, \tag{2.103}$$

and this implies that $w_1$ is constant on the secondary streamlines $\chi_0$ (Blennerhassett, 1976). However, the most important part of his work is his numerical results in which he solved directly the coupled equations (2.16)–(2.17) for various values of $D$ and $R_s$. For $D = o(R_s)$, as $D$ is small the effect of the steady component of the pressure gradient is fairly weak, so the secondary streaming flow at the core behaves in the same manner as in the purely oscillatory case. Figure 2.13 shows the secondary streamlines (left) and the contours of axial velocity (right) for various values of $R_s$.




(a) $t = 0$ (b) $t = \pi/3$ (c) $t = 2\pi/3$

(d) $t = 0$ (e) $t = \pi/3$ (f) $t = 2\pi/3$

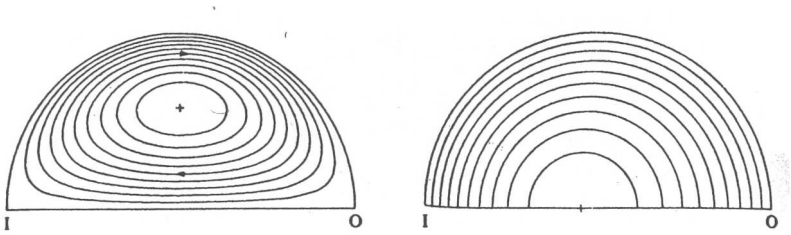
Figure 2.12: The streamlines (above) and the axial velocity contours (below) for $R_s = 300$, $\alpha = 20$ at time $t = 0, \pi/3, 2\pi/3$. The solid curves represent the solutions for $\delta = 0$, and dotted curves for $\delta = 0.3$. Reproduced from (Siggers & Waters, 2008).

There is no qualitative change in the secondary streamlines when $R_s$ varies. For small values of $R_s$, the maximum axial velocity is slightly shifted along the plane towards the inner wall. As $R_s$ increases, the axial velocity is advected towards the inside wall of the bend and swept round sideways as shown in Figure 2.13. Moreover, the maximum axial velocity comes off from the plane and tends to move to the center of the semicircle. As $R_s \to \infty$, the axial velocity contours appear to coincide with the secondary streamlines contours. This confirmed his asymptotic result, in which $w_1$ is constant on the secondary streamlines.

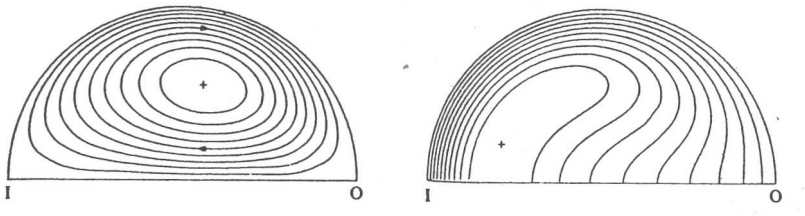
When $D = O(R_s)$, the numerical results showed some interesting features. He let $R_s = 30$, and (a) $D = 40$ and (b) $D = 160$. As shown in Figure 2.14, when $D$ is small, the secondary flow is directed inwards, and the maximum axial velocity takes place near the inner wall on the centre plane. As $D$ increases, the effect of steady pressure gradient becomes stronger. The core flow driven by the slip velocity at the edge of the Stokes layer moves outwards, and the peak axial velocity moves towards the outer wall.

Furthermore, Blennerhassett (1976) found that there exists a critical value of $R_s$ between 75 and 100 for any values of $D$. If $R_s$ exceeds this critical value, the most intriguing result is obtained. By plotting the graph of flow rate ratio $Q$ (the ratio betwen the flow rate in a curved tube and that in a straight tube at a given mean pressure gradient) against the Dean number $D$ when $R_s$ is fixed, an S-shaped portion appears, as shown in Figure 2.15. When $D$ gradually increases, $Q$ follows the lower branch. Once $D$ reaches the turning point $B$ where the slope of the curve becomes infinite, $Q$ jumps to the upper branch. Conversely, if $D$ begins from the large value of $D$ and is subsequently reduced, $Q$ will follow the upper branch, and immediately jump downwards to the lower branch when it reaches the turning point $E$ (Pedley, 1980).

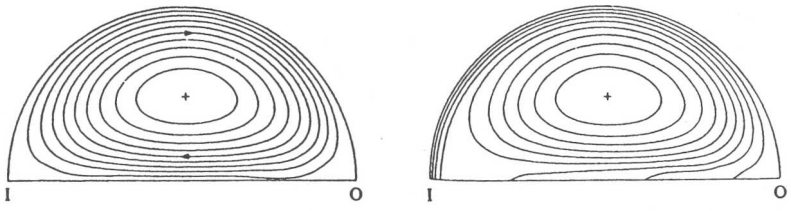
Figure 2.16 shows the flow patterns at fixed $D = 244$ and $R_s = 100$ on three branches of




(a)




(b)




(c)

Figure 2.13: Plots of secondary streamlines (left) and axial velocity contours (right) of the fluid flow driven by the oscillatory pressure gradient in which the steady component of the pressure gradient $D$ is much smaller than the secondary streaming Reynolds number $R_s$; (a) $R_s = 10$, (b) $R_s = 150$ and (c) $R_s = 1800$. I and O denote the inside and outside of the bend respectively. Reproduced from Blennerhassett (1976).

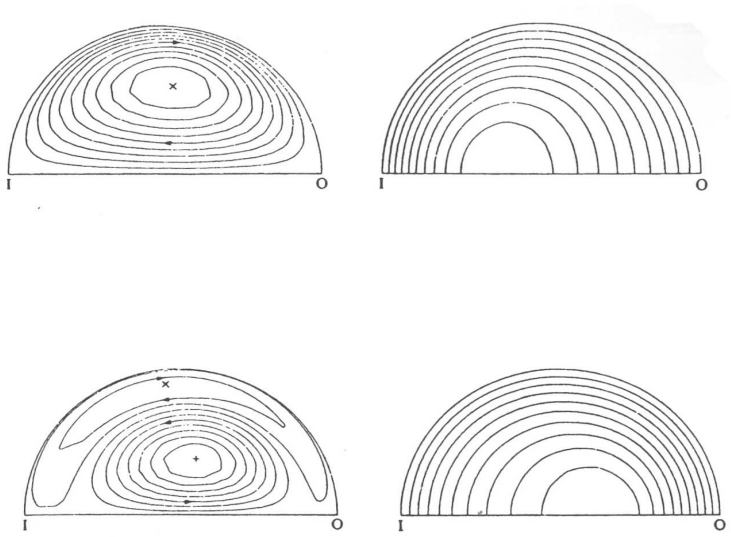



Figure 2.14: Illustration of secondary streamlines (left) and axial velocity contours (right) of the oscillatory flow. Here, (a) $D = 40$, (b) $D = 160$ for $R_s = 30$. I and O denote the inside and outside of the bend respectively. Reproduced from Blennerhassett (1976).

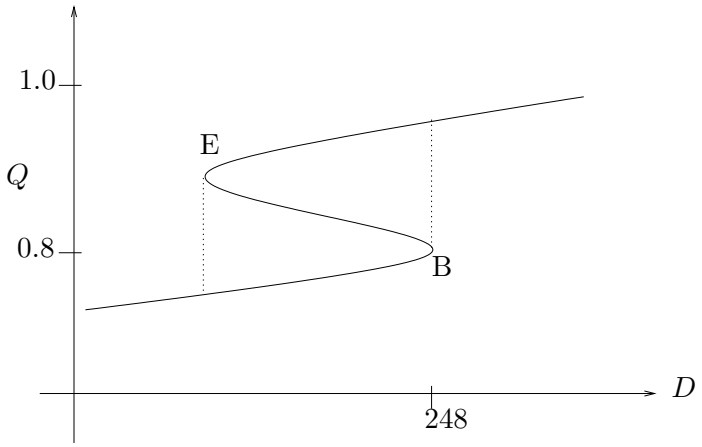
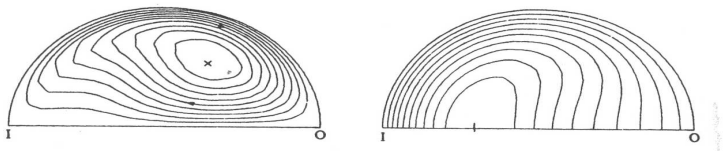


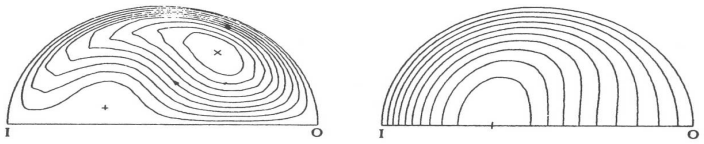

Figure 2.15: The S-shaped portion of the plot between of the flow rate ratio and $D$ at fixed $R_s = 100$. Reproduced from Blennerhassett (1976).

the S-shaped portion. Figure 2.16 (a) shows that the secondary flow corresponding to the lower branch is directed towards the inside of the bend which is similar to the flow driven by the purely oscillatory pressure gradient. Whereas the core flow corresponding to the upper branch behaves in a similar manner to the flow driven by the steady pressure gradient. The middle branch represents an intermediate type of flow which was not realised in practice.

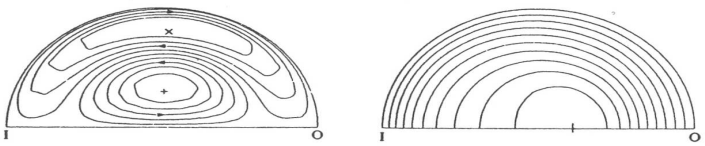
Siggers & Waters (2008) studied flows driven by oscillatory pressure gradients in pipes with finite curvature both analytically and numerically. The flow behaviour is determined by four dimensionless parameters: the curvature $\delta$; the Dean number $D$; the Womersley




(a)

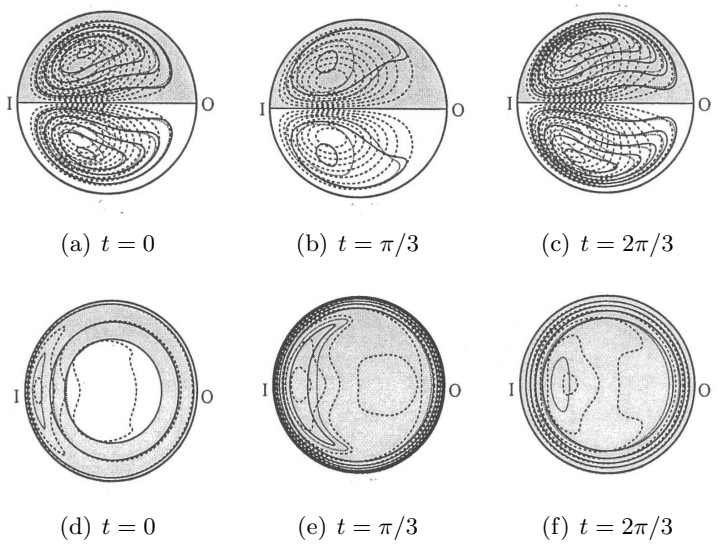



(b)




(c)

Figure 2.16: Illustration of secondary streamlines (left) and axial velocity contours (right) of the oscillatory flow. I and O denote the inside and outside of the bend respectively. (a) lower branch, (b) middle branch and (c) upper branch show the contours of streamline function and axial velocity on the S-shaped portion of the curve at fixed $R_s = 100, D = 244$. Reproduced from Blennerhassett (1976).




(a) $t = 0$ (b) $t = \pi/3$ (c) $t = 2\pi/3$

(d) $t = 0$ (e) $t = \pi/3$ (f) $t = 2\pi/3$

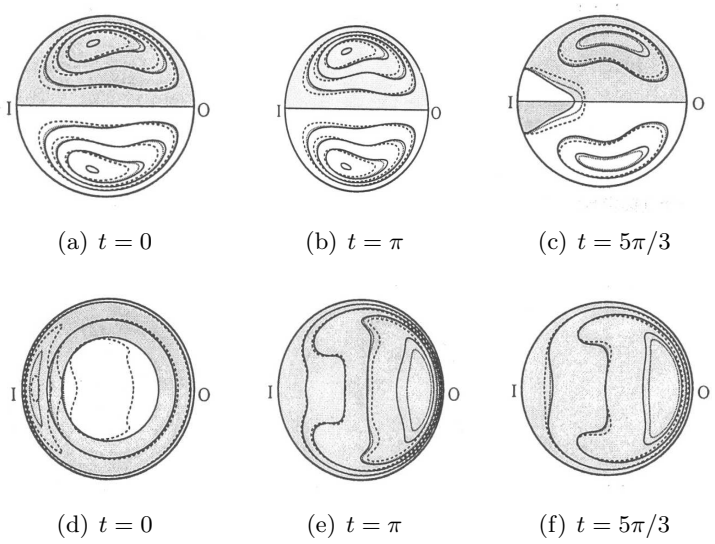
Figure 2.17: Illustration of secondary streamlines (above) and axial velocity contours (below) of the oscillatory flow for $D = 0, R_s = 50, \alpha = 10$. Solid lines, $\gamma = 0$; dotted lines, $\gamma = 0.1$; dashed lines, $\gamma = 0.3$ I and O denote the inside and outside of the bend respectively. Reproduced from Siggers & Waters (2008).

number $\alpha$; and the secondary streaming Reynolds number $R_s$.

They used regular perturbation techniques to find the series solution for small $\delta$, $D$ and $\alpha^3 {R_s}^{1/2}$ (an amplitude of the oscillatory component of the pressure gradient). They generalised Lyne's analysis by using matched asymptotic expansions for sinusoidal flow with large $\alpha$. For larger dimensionless parameters, a pseudospectral code was used to obtain both spatially symmetric and asymmetric results at some particular values of the governing parameters. At large $D$, the axial velocity contours become vertical and the axial vorticity in the streamlines is evident and approximately constant in the core. Moreover, the branch (2) and branch (3) solutions in Figure 2.11 are expected to converge to branch (1) as the effect of steady component dominates the time-dependent component of the pressure gradient. Figure 2.17 and 2.18 show the evolution of secondary streamlines and axial velocity contours.

## 2.5 Conclusion

The goal of this chapter is to gain an understanding of the importance of dynamic curvature on the steady/pulsatile flow patterns in an individual curved tube. A number of analytic work has been in reasonable agreement with directly relevant experiments and computations. We started by studying flows driven by steady pressure gradient in a weakly curved tube. The flow features, for example, the axial velocity profile distortions, the volume flux and the friction ratio, have been found to alter as the Dean number increases. As the Dean number continues to increase until it surpasses the critical value, the bifurcation of the flow appears and the number of vortexes in the cross section changing from 2 to 4. Nevertheless, our main focus is on the effects of dynamic curvature variation in wall shear stress which correlates with the location of atherosclerosis. The pulsatile flows studied in §2.4 are, however, believed to be more related to the pulsatile nature of the complex blood flow in




(a) $t = 0$ (b) $t = \pi$ (c) $t = 5\pi/3$

(d) $t = 0$ (e) $t = \pi$ (f) $t = 5\pi/3$

Figure 2.18: Illustration of secondary streamlines (above) and axial velocity contours (below) of the oscillatory flow for $D = 5000, R_s = 50, \alpha = 10$. Solid lines, $\gamma = 0$; dotted lines, $\gamma = 0.1$; dashed lines, $\gamma = 0.3$ I and O denote the inside and outside of the bend respectively. Reproduced from Siggers & Waters (2008).

arteries. Under pulsating conditions and zero mean flow rates, viscosity effects are limited close to the tube walls for high Womersley numbers. For small Womersley numbers, the flow patterns tend to behave analogous to steady flows.

The models that are most relevant to a vascular system, as far as this review is concerned, are done by Siggers & Waters (2008) who studied the case when the flow is driven by oscillatory pressure gradient with non zero mean in a finite curved tube. The stable solutions of this flow are qualitatively justified from the bifurcation structure, and the finite curvature leads to the substantial differences in wall shear stress.

It has been clear that computations become essential part of the research in this field due to the complexity of the flow behaviours when a range of parameters comes into consideration.

# Chapter 3

# Thin-film flows

The study of thin-film flows is important in view of their applicability to many situations in biology, engineering, industry and technology. Numerous publications have appeared in the literature on this topic, both theoretical and experimental. Examples of related applications range from the tear film on an eye (Braun & Fitt, 2003), soap bubbles (Howell, 1999) and drying paint (Howison et al., 1997). A wide range of thin film topics will be covered in this chapter. In particular, the derivation of thin film equation and its stability are of our interests because the models developed in chapter 5 are relied on these two topics. In addition, the Marangoni flows as well as the moving contact line problems will be explored despite their irrelevance to our present models in the thesis. However, both topics could be used to apply to the models in the future when the plaque can be treated as a viscous droplet and the surface tension gradient effects due to the components of the blood and the plaque can also be considered.

We will start by deriving the evolution equation for thickness of a thin film in §3.1. Then in §3.2, we will explore the work on thin film stability in both a straight and elastic tubes. In §3.3, the Marangoni effect will be studied, particularly, the effect of surfactant which is key ingredient in many biological systems. In §3.4, moving contact line problems will be discussed briefly and the conclusion of this chapter will be drawn in §3.5.

## 3.1 Derivation of thin liquid film equation

Consider a two dimensional thin liquid layer on an inclined plane with angle $\alpha$ to the horizontal plane. The fluid is modelled as an incompressible, Newtonian viscous fluid with dynamic viscosity $\mu$, and a constant density $\rho$. The Cartesian coordinate system $(x, y)$ is chosen with $x$ being distance down the line of greatest slope and $y$ being distance normal to the plane. We denote the fluid velocity and pressure by $\boldsymbol{u}(x, y, t) = (u, v)$ and $p(x, y, t)$, respectively. We assume that free surface of the thin liquid layer is $y = h(x, t)$, as shown in Figure 3.1. In our model system, the forces that drive the thin liquid film are surface tension, surface tension gradients and gravity.

We start with the dimensional incompressible Navier-Stokes equations (Ockendon & Ockendon, 1995),

$$\rho\left(\frac{\partial \boldsymbol{u}}{\partial t} + (\boldsymbol{u}\cdot\boldsymbol{\nabla})\boldsymbol{u}\right) = -\boldsymbol{\nabla}p + \rho\boldsymbol{g} + \mu\boldsymbol{\nabla}^2\boldsymbol{u}, \tag{3.1}$$

$$\boldsymbol{\nabla}\cdot\boldsymbol{u} = 0, \tag{3.2}$$

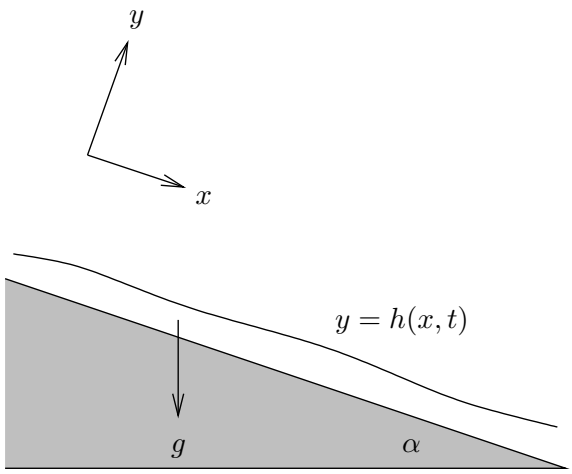



Figure 3.1: Schematic of a thin fluid film on the inclined substrate.

where $\boldsymbol{g}$ the gravitational acceleration. No-slip and no-flux conditions give

$$u = v = 0, \qquad \text{on} \qquad y = 0. \tag{3.3}$$

At the interface $y = h(x,t)$, we have the kinematic boundary condition

$$v = h_t + uh_x, \tag{3.4}$$

where subscripts $x$ and $t$ denote partial differentiation with respect to $x$ and $t$, respectively. We now describe the conditions which ensure continuity of stress at the interface. We assume that the stress exerted by the upper layer is zero. Let $\boldsymbol{t} = \hat{\boldsymbol{n}} \cdot \boldsymbol{T}$ be the stress vector, the force per unit area exerted by the fluid layer on the interface, where $\hat{\boldsymbol{n}}$ is the unit outward normal to the interface. The stress tensor $\boldsymbol{T}$ is written as $\boldsymbol{T} = -p\boldsymbol{I} + \mu\left(\boldsymbol{\nabla u} + (\boldsymbol{\nabla u})^T\right)$. Then the stress balance equation is given by

$$\hat{\boldsymbol{n}} \cdot \boldsymbol{T} = \boldsymbol{\nabla}_s \sigma - \sigma \hat{\boldsymbol{n}} (\boldsymbol{\nabla}_s \cdot \hat{\boldsymbol{n}}), \tag{3.5}$$

where $\boldsymbol{\nabla}_s$ is the tangential gradient operator which is defined by

$$\boldsymbol{\nabla}_s = \boldsymbol{\nabla} - \hat{\boldsymbol{n}} \frac{\partial}{\partial n}, \tag{3.6}$$

and $\sigma = \sigma_0 + \triangle\sigma(\sigma_1(x))$ is the surface tension with $\sigma_0$ constant, and $\sigma_1$ able to vary.

The jump in normal stress across the interface must balance the curvature force per unit area. By taking $\hat{\boldsymbol{n}}\cdot$ (3.5), it yields

$$\hat{\boldsymbol{n}} \cdot \boldsymbol{T} \cdot \hat{\boldsymbol{n}} = \sigma\kappa, \tag{3.7}$$

where $\kappa = -\nabla_s \cdot \hat{\boldsymbol{n}}$ is a surface curvature.
By taking $\hat{\boldsymbol{t}}\cdot$ (3.5), we find

$$\hat{\boldsymbol{n}} \cdot \boldsymbol{T} \cdot \hat{\boldsymbol{t}} = \nabla_s \sigma \cdot \hat{\boldsymbol{t}}. \tag{3.8}$$

The right hand side of (3.8) may result from gradients in temperature or chemical composition at the interface. The unit outward normal, $\hat{\boldsymbol{n}}$, and unit tangent, $\hat{\boldsymbol{t}}$, to the interface are given by

$$\hat{\boldsymbol{n}} = \frac{1}{(1+h_x^2)^{1/2}} \begin{pmatrix} -h_x \\ 1 \end{pmatrix}, \qquad \hat{\boldsymbol{t}} = \frac{1}{(1+h_x^2)^{1/2}} \begin{pmatrix} 1 \\ h_x \end{pmatrix}, \tag{3.9}$$

and the curvature is

$$\kappa = \frac{h_{xx}}{(1+h_x^2)^{3/2}}. \tag{3.10}$$

Hence, the free surface stress boundary conditions on $y = h(x,t)$ are given by

$$-p + \frac{2\mu}{1+h_x^2}\left(h_x^2\frac{\partial u}{\partial x} - h_x\left(\frac{\partial u}{\partial y} + \frac{\partial v}{\partial x}\right) + \frac{\partial v}{\partial y}\right) = \frac{(\sigma_0 + \triangle\sigma(\sigma_1(x)))h_{xx}}{(1+h_x^2)^{3/2}}, \tag{3.11}$$

$$-\frac{\mu}{1+h_x^2}\left[2h_x\left(\frac{\partial u}{\partial x} - \frac{\partial v}{\partial y}\right) + (h_x^2-1)\left(\frac{\partial u}{\partial y} + \frac{\partial v}{\partial x}\right)\right] = \frac{(\triangle\sigma)}{(1+h_x^2)^{1/2}}\left(\frac{\partial \sigma_1}{\partial x}\right). \tag{3.12}$$

### 3.1.1 Nondimensionalisation and scaling

By introducing the typical lengthscale $L$ along the film, and the velocity scale $U$. We then assume that the fluid forms a thin film of typical thickness $H$, and suppose that a small aspect ratio $\delta = H/L \ll 1$. The dimensionless variables are as follows:

$$x = Lx^*, \qquad y = \delta L y^*, \qquad u = Uu^*, \qquad v = \delta U v^*, \qquad t = \frac{L}{U}t^*, \qquad p = \frac{\mu U}{\delta^2 L}p^*. \tag{3.13}$$

We then obtain the dimentionless governing equations in component form (dropping asterisks on the dimensionless variables),

$$\delta^2 Re\left(\frac{\partial u}{\partial t} + u\frac{\partial u}{\partial x} + v\frac{\partial u}{\partial y}\right) = -\frac{\partial p}{\partial x} + St\sin\alpha + \delta^2\frac{\partial^2 u}{\partial x^2} + \frac{\partial^2 u}{\partial y^2}, \tag{3.14}$$

$$\delta^4 Re\left(\frac{\partial v}{\partial t} + u\frac{\partial v}{\partial x} + v\frac{\partial v}{\partial y}\right) = -\frac{\partial p}{\partial y} - St\delta\cos\alpha + \delta^4\frac{\partial^2 v}{\partial x^2} + \delta^2\frac{\partial^2 u}{\partial y^2}, \tag{3.15}$$

$$\frac{\partial u}{\partial x} + \frac{\partial v}{\partial y} = 0, \tag{3.16}$$

where $Re = \rho LU/\mu$ is the Reynolds number, and $St = \delta^2\rho g L^2/\mu U$ is the Stokes number. In order to find the size of $U$, we can set $St = 1$ so that $U = H^2\rho g/\mu$. The boundary conditions at the free surface $y = h(x,t)$ are

$$h_t + uh_x = v, \tag{3.17}$$

The normal and tangential stress balance at the interface $y = h(x,t)$ become

$$-p + \frac{2\delta^2}{1+\delta^2 h_x^2}\left(\delta^2 h_x^2\frac{\partial u}{\partial x} - h_x\left(\frac{\partial u}{\partial y} + \delta^2\frac{\partial v}{\partial x}\right) + \frac{\partial v}{\partial y}\right) = (C + \delta M\sigma_1(x))\left(\frac{h_{xx}}{(1+\delta^2 h_x^2)^{3/2}}\right) \tag{3.18}$$

$$2\delta^2 h_x\left(\frac{\partial u}{\partial x} - \frac{\partial v}{\partial y}\right) + (\delta^2 h_x^2 - 1)\left(\frac{\partial u}{\partial y} + \delta^2\frac{\partial v}{\partial x}\right) = (Mh_{xx})\left(\frac{\partial \sigma_1}{\partial x}\right)\sqrt{1+\delta^2 h_x^2}, \tag{3.19}$$

where $C = \delta^3\sigma_0/\mu U$ is the inverse Capillary number and $M = \delta^2\triangle\sigma/\mu U$ is the Marangoni number.

We obtain at leading order the quasi-steady lubrication equations

$$0 = -\frac{\partial p}{\partial x} + St\sin\alpha + \frac{\partial^2 u}{\partial y^2}, \tag{3.20}$$

$$0 = \frac{\partial p}{\partial y} + \delta St\cos\alpha, \tag{3.21}$$

$$0 = \frac{\partial u}{\partial x} + \frac{\partial v}{\partial y}. \tag{3.22}$$

The fluid flow is driven by surface tension (through the pressure gradient), gravity and surface shear. At leading order, the boundary conditions at the free surface $y = h(x,t)$ become

$$\begin{aligned} v &= \frac{\partial h}{\partial t} + u\frac{\partial h}{\partial x}, && (3.23)\\ p &= -Ch_{xx}, && (3.24)\\ \frac{\partial u}{\partial y} &= M\frac{\partial \sigma_1}{\partial x}, && (3.25) \end{aligned}$$

and on $y = 0$,

$$u = v = 0. \tag{3.26}$$

Integrating (3.21) with respect to $y$ and applying (3.24) gives

$$P = -\delta St\cos\alpha(y-h) - Ch_{xx}. \tag{3.27}$$

To derive an equation for $h(x,t)$, we first integrate equation (3.20) twice between $y = 0$ and $y = h(x,t)$, and using the boundary conditions (3.25) and (3.26) to obtain an expression

$$\begin{aligned} u &= (p_x - St\sin\alpha)\left(\frac{y^2}{2} - hy\right) + (M\sigma_{1,x})y,\\ &= (Ch_{xxx} - \delta St\cos\alpha h_x + St\sin\alpha)\left(hy - \frac{y^2}{2}\right) + M\sigma_{1,x}y. \end{aligned} \tag{3.28}$$

By integrating (3.22) and applying the kinematic boundary condition (3.23), it gives

$$\frac{\partial h}{\partial t} + \frac{\partial Q}{\partial x} = 0, \tag{3.29}$$

where $Q$ is the fluid flux defined by $Q = \int_0^h u\,dy$.
Substituting (3.28) into (3.29) leads to a fourth-order nonlinear parabolic equation

$$h_t + \left(\frac{h^3}{3}(Ch_{xxx} - \delta Sth_x\cos\alpha + St\sin\alpha) + \frac{M}{2}\sigma_{1,x}h^2\right) = 0. \tag{3.30}$$

Equation (3.30) governs the evolution of the thin-film depth due to the effect of surface tension, gravity and surface tension gradients. When $\alpha$ is large enough, the term $\delta Sth_x\cos\alpha$ is negligible compared with $St\sin\alpha$.

## 3.2 Thin film stability

### 3.2.1 Thin film stability

This section, we will focus on the stability of thin liquid flows lined on a cylindrical tube because they have been applied to various applications including lungs' airway (Gaver & Grotberg, 1990; Borgas & Grotberg, 1988) and industrial coating processes (Craster & Matar, 2006). We start this section by describing briefly some of the liquid properties that cause the flow generation.

Liquid molecules in a bulk attract one another in all directions resulting in a net force of zero. Liquid molecules near an air-liquid interface are balanced along the tangential

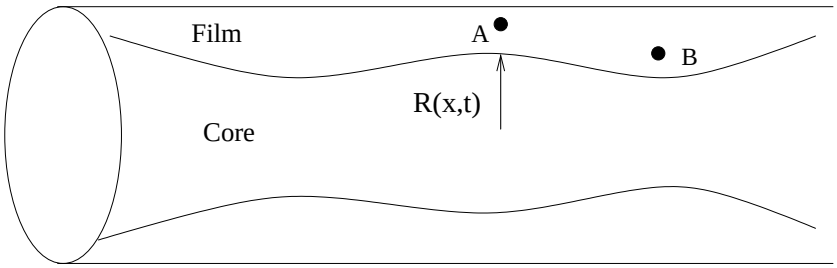



Figure 3.2: Thin film lining on a cylindrical tube.

direction, but the attractive force from liquid molecules in a bulk pull molecules at the air-liquid interface causing the interface to contract. The magnitude of the attractive force per unit length of a line on the interface is called surface tension $\sigma$, which has the units N/m.

The surface tension, $\sigma$, and the pressure difference across the surface, $\triangle p$, are related by the Young-Laplace equation

$$\triangle p = p_c - p_f = -\kappa\sigma, \tag{3.31}$$

where $p_c$ is the core pressure, $p_f$ the thin film pressure and $\kappa$ the curvature of the interface given by

$$\kappa = -\frac{1}{R\sqrt{1+R_x^2}} + \frac{R_{xx}}{(1+R_x^2)^{3/2}}, \tag{3.32}$$

where $R(x,t)$ is the radial position of the film surface, $x$ is the axial coordinate and $t$ is time.

If we suppose that a thin film undergoes a long-wavelength disturbance, the non-uniform mean curvature can be approximated such that

$$\kappa \approx -\frac{1}{R}, \tag{3.33}$$

so the Young-Laplace equation becomes

$$p_c - p_f = \frac{\sigma}{R}. \tag{3.34}$$

In Figure 3.2, the radius of the thin film at the point A is greater than at the point B, and so the pressure decreases from A to B. A surface-tension-driven flow will then drive the liquid from A to B, causing the flow instability at the point B. This phenomenon is called the *Rayleigh instability*. The example of Rayleigh instability is water droplets lining on spider's web, as shown in Figure 3.3. The liquid lining readjusts so that the new equilibrium system has the lower surface energy.

Goren (1962) was the first to investigate the dynamic stability of a cylindrical annular layer surrounding a wire, or coating the inside of a small tube subject to axisymmetric disturbances. He determined the wavelength of the fastest growing disturbance for both viscous and inviscid fluids. He found that the disturbance with wavelength $\lambda > 2\pi a$, where $a$ is a distance from the tube core to the air-fluid interface, gives instability. Goren also verified his theoretical predictions experimentally.

Hammond (1983) conducted a nonlinear stability of an axisymmetric thin viscous film coating the interior of a cylindrical rigid tube with different fluid at the core. He assumed



Figure 3.3: Liquid droplets on spider's web *http://www.serenejourney.com/2009/09/have-a-look-at-what-youve-been-missing.*

that the core fluid is much less viscous than the thin liquid film. He introduced $\epsilon H(x,t)$ as a thickness of the thin layer, where $0 < \epsilon \ll 1$, $x$ is the axial coordinate and $t$ is time. By applying the lubrication approximation, he derived the leading order evolution equation for interface disturbance such that

$$H_t + \frac{1}{3}(H^3(H_{xxx} + H_x))_x = 0. \tag{3.35}$$

Equation (3.35) is the thin-film equation (3.30) in a cylindrical tube with $B = \Sigma = 0$ and $\Gamma = 1$. The $H_{xxx}$ and $H_x$ terms originate from the axial and azimuthal components of the surface curvature.

To analyze the linear stability of the thin liquid film, Hammond set

$$H(x,t) = 1 + H_0 e^{\alpha t + ikx}, \tag{3.36}$$

where $\alpha$ is the growth rate and $k$ is the wave number. Substituting (3.36) into (3.35) gives

$$\alpha = \frac{1}{3}k^2(1 - k^2), \tag{3.37}$$

which implies that, for sufficiently long wavelength where $0 < k < 1$, the flow is unstable.

For the steady state system, (3.35) becomes

$$H^3(H_{xxx} + H_x) = 3Q, \tag{3.38}$$

where $Q$ is a constant film volume flux. If $Q \neq 0$, Hammond assumed that $H(x)$ is bounded by constant values. By integrating (3.38) twice, $H$ will be bounded below and above by functions that grow like $x^3$. This is inconsistent with the finite film-thickness assumption for all $x$. If $Q = 0$, the film can take the form

$$H = A + B\cos x, \tag{3.39}$$

where $A, B$ are constants. If a uniform film is disturbed by an axisymmetric perturbation, then the film redistributes into an unduloid family of axisymmetric wetting collars of axial

length greater than $2\pi$ (for which $A = B$), and lobes of axial length less than $2\pi$ (for which $A < B$). The case $A > B$ describes a neutrally stable disturbance of thin film. For a sufficiently short cylinder, as the collar pressure is less than the lobe pressure, this results in fluid drainage from a lobe to an adjacent stationary collar if the gab between them is not sufficiently large. Based on his numerical results, Hammond concluded that the collars are always stable.

Gauglitz & Radke (1988) predicted that when collars experience lobe drainage, they would reach the maximum volume where the stability limit occurs, and beyond this threshold value, the stable collars would become unstable and snap off to form a liquid bridge. They extended Hammond's analysis by including a higher term into the curvature term and applied the Young-Laplace equation for the curvature of the film interface to give more accurate solutions. They found numerically that when film thickness is greater than $0.12a$, where $a$ is a tube radius, the stable collars have enough fluid to form a bridge. The evolution is illustrated in Figure 3.4.

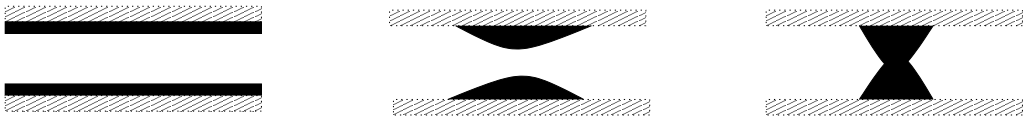


Figure 3.4: Diagram showing how a liquid bridge is formed .

Lister et al. (2006) investigated the long-time dynamics of Hammond's model for long cylinder lengths. Their numerical simulations showed that the collars can move sideways, over a lobe, and ultimately collide with other collars. Each collar moves in response to the difference in pressure in the film on either side of the collar. As the collar length is constant ($2\pi$), it leaves behind a new and smaller lobe as it moves. The collar gains volume as it slides, because the daughter lobe is found to have a smaller volume than the lobe consumed.

### 3.2.2 Thin film stability in an axisymmetric elastic tube

Motivated by a closure of small airways of the lung, Halpern & Grotberg (1992b) investigated a thin-walled elastic tube lined with a thin liquid film in an axisymmetric system with the constant exterior pressure. The coupled nonlinear evolution equations for the film thickness and wall deformation were derived, using lubrication theory and a modified expression for the interfacial curvature. They studied both linear and nonlinear dynamic stability for various parameter values. One of crucial parameters they focused on is $\Gamma$, the ratio of surface tension forces to elastic forces, given by

$$\Gamma = \frac{(1-\gamma^2)\sigma}{Eh_0}, \tag{3.40}$$

where $\gamma$ is the Poisson ratio of the wall material, $E$ is the Young's modulus, and $h_0$ is the wall thickness. The numerical solutions showed that when the wall elasticity increases, the time for bridge formation also increases. The physical explanation is that large wall elasticity induces the more shear resistance for the liquid to form a liquid bridge, and this results in a large time being taken for the lobes to reach the threshold volume for the instability threshold beyond which a liquid bridge is formed. An increase in $\Gamma$, due to either the larger surface-tension or smaller Poisson ratio of the wall, results in a smaller closure time. Roughly speaking, the mean surface tension can give rise to instability of the thin liquid film, while wall elasticity acts to stabilize the film.

The other important parameter in their analysis is the critical film thickness to tube radius ratio, $\epsilon_c$, which is dependent on the wall and fluid properties, for example, $\epsilon_c(\Gamma_c = 0) \approx 0.17$ and $\epsilon_c(\Gamma_c = 0.5) \approx 0.11$. An increase in $\epsilon_c$ induces faster closure times which is consistent with results for rigid tube, performed by Gauglitz & Radke (1988). This model may not be a suitable model of the lung airway because in practice the liquid lining collapses into a buckled, non-axisymmetric shape. For a comprehensive review see Grotberg & Jensen (2004).

### 3.2.3 Two thin liquid films

The airway surface fluid is present as a bilayer comprising a mucus layer and preciliary fluid layer (serous layer) which lies between the cellular surface and the mucus layer. Mucus is a non-homogeneous, viscoelastic fluid containing glycoproteins, and lipid. Mucus protects the epithelium from the inhaled foreign materials. In many respiratory diseases, mucus hypersecretion takes place and this excessive mucus must be removed, typically, by coughing. Cough clearance derives from the high velocity interaction between airflow and the mucus, resulting in wave formation in the mucus layer. The time taken for this clearance process is principally affected by the maximal forward velocity of the mucus and the depth of the serous layer (Stockley et al., 2007).

Moriarty & Grotberg (1999) investigated this thin bilayer by taking the serous fluid to be a Newtonian fluid and using a Kelvin-Voigt model for the mucus layer, meaning, the viscoelastic damping is proportional to the rate of deformation. The new parameter is defined by $K' = \sigma/dG'$, where $\sigma$ is the air-mucus surface tension, $G'$ is the elastic shear modulus of the mucus, and $d$ is a characteristic thickness of the bilayer. This parameter describes the ratio of surface tension to elastic-shear forces at the air-mucus interface. In this paper, the authors tried to understand the effect of the serous layer and the effect of surface tension on the dynamic instability of the overall system. They determined the instabilities by solving the linearized system to obtain a dispersion relationship and classifying the waves according to the activation energy of the coating and the work done by the coating. They found that, without surface tension at the air-mucus interface, the presence of the serous layer would cause the long-wave instabilities due to the Bernoulli forcing of the air flow. In contrast, for the short wavelengths, the instability is not affected by the the presence of this thin vicous layer, but depends on the air flow speed. When the flow speed is below the critical flow speed $U_c$, the system is stable because the elastic energy is greater than the work done by the kinetic exterior force.

Once the surface tension at the air-mucus interface is present, it acts to stabilize the system by stiffing the entire system and it raises the critical air speed required for instability. When the serous layer is present, the critical flow speed required to generate an instability is lower than in the system where the serous is absent.

## 3.3 The Marangoni effect

This effect describes the mass transfer along a fluid-fluid interface induced by the nonuniform distribution of surface tension $\sigma$, which drives the liquid from regions of low surface tension to regions of high surface tension. Typically, the value of surface tension $\sigma$ depends on both chemical composition and the temperature of the fluid at the interface.

The Marangoni effect was first observed and analyzed by Thomson (1877) through the so-called *tears of wine* effect. This phenomenon occurs especially with wine of a fairly high

ethanol content. After a glass of wine is swirled, a ring of clear wine droplets are established near the top of the glass and then fall back to the bulk of wine below, as shown in Figure 3.5.



Figure 3.5: Tears of wine *http://wine-scamp.com/2007/09/05/quit-staring-at-my-legs.*

Ethanol has a much lower surface tension than water and it evaporates faster than water. Consequently the concentration of wine near the top of the glass decreases more than that in the bulk. Hence the surface tension gradient forms, and this inhomogeneity leads to the generation of a force pulling the film upward. Hence thicker rims of ethanol-depleted wine are formed, resulting in wine droplets formation near the top of the glass. When the tear rim of the droplets become heavy, gravity is a dominant force causing them to move downwards. This process continues until the ethanol content becomes too low. This classic example shows how the Marangoni effect works in general.

The Marangoni effect has also been exploited in industrial processes. For instance, in drying process in the semiconductor industry, traditionally a spin drying technique is used by applying a centrifugal force to remove most of the liquid and the final stage is by using evaporation techniques to eliminate the rest of the liquid. However, the drawback of this technique is the existence of contaminant on the substrate surface. In contrast, Marangoni-driven drying can be carried out by putting a vapor source near the fluid film and once the wafer is withdrawn from the pool of water, a surface-tension gradient occurs and and the fluid is expelled as a result. There are some industrial processes that apply rather similar technique to this, details of which are reviewed by Oron et al. (1997) and Myers (1998).

A surfactant is an amphiphilic molecule consisted of two parts, one which is soluble in water and also in organic solvents (*a hydrophilic ionic head-group*), and one which is insoluble (*a hydrocarbon tail*), see Figure 3.6. Surfactant is a surface active agent which refers to the molecule's ability to adsorb at the liquid-gas interface. Under cetain circumstances, the surfactant molecules start to form complicated molecules called aggregates, so-called micelles. The micelle formation is an adsorption mechanism that reduces the free energy of the system. Nevertheless, for this to occur, the concentration of surfactant must be above a critical concentration which is called critical micelle concentration (CMC) (Holmberg et al., 2004).

From the biological point of view, surfactant is essential in the mammalian body system. It coats the interior of the pulmonary airway in order to retain lung compliance, and also

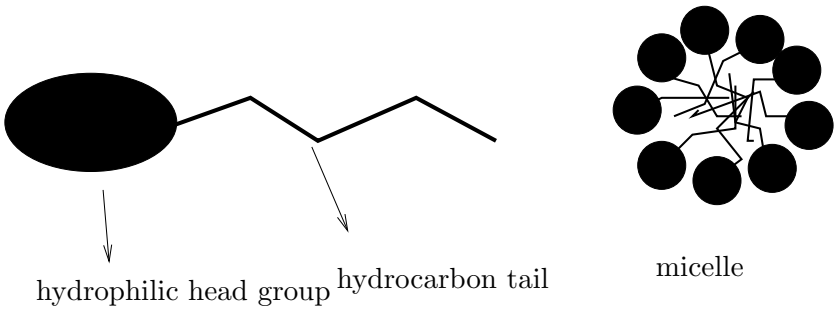



Figure 3.6: Schematic illustrations of surfactant.

prevent airway collapse as a result of large exterior forces.

In the last past decade, several papers have been published concerned with the development of Respiratory Distress Syndrome (RDS). The cause of the syndrome is due to the deficiency of surfactant in alveoli and can result in severe respiratory difficulties in prematurely born babies. The common treatment for this syndrome is to deliver synthetic surfactant into the respiratory tract. The dynamical interaction between this complex synthetic surfactant and the liquid lining on the lung is an intricate process involving the rapid distribution of a surfactant formulation to a liquid layer. The principal mechanism for the surfactant distribution can be modelled as the spontaneous monolayer spreading along the liquid layer.

When the surfactant solution spreads over a liquid film, it can give rise to the Marangoni flow. Here, we consider a liquid film with an initially uniform thickness $H$ with constant viscosity $\mu$, and the liquid is partially covered with a drop of surfactant. The surface tension at the air-liquid interface is defined by $\sigma_2$, and $\sigma_1$ defines the surface tension at the air-surfactant interface.

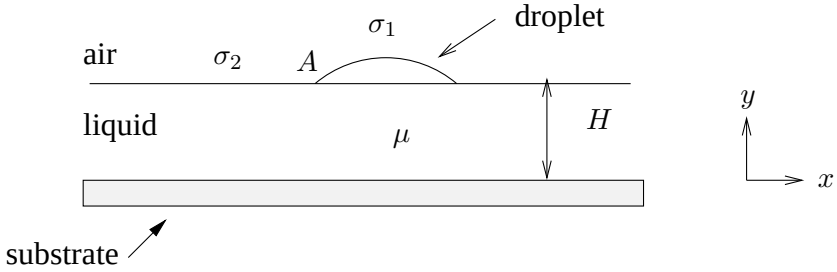



Figure 3.7: Diagram of two-dimensional surfactant droplet on a thin film layer above a rigid wall.

The spreading parameter, $S$, is used to characterize the equilibrium of the droplet and is defined by

$$S = \sigma_2 - \sigma_1. \tag{3.41}$$

In order for spreading to occur, the value of $S$ must be positive. In Figure 3.7, at the junction $A$ where the surfactant drop joins the liquid film, there exists a very high shear stress due to a large surface tension gradient at this point. This shear stress forces both the liquid film and surfactant to move towards regions of higher surface tension. This results in a spontaneous spreading of the surfactant drop over the liquid film, thereby reducing the surface energy of the entire film.

Borgas & Grotberg (1988) applied the lubrication approximation which assumes that the film thickness is much smaller than the extent of spreading, and adopted the equation of state which relates the surface tension to the local concentration of surfactant to derive a pair of couple nonlinear evolution equations for the liquid film thickness and surfactant concentration. Numerical solutions were obtained for a steady state problem. The results showed that, under the effect of convection only, the film height at the leading edge of the monolayer thickens discontinuously to twice its undisturbed value. When the surface diffusion is present, the shock-like structure of film thickness is smoothed out resulting in a continuous profile.

Gaver & Grotberg (1990) later extended the work by Borgas & Grotberg (1988) by investigating the effect of parameters such as the Peclet number $Pe$, the ratio of mass transport by convection to mass transport by diffusion. Hence

$$Pe = \frac{SH}{\mu D} = \frac{UL}{D}, \tag{3.42}$$

where $U$ is a characteristic velocity (by setting the Capillary number equal to 1), $L$ is a characteristic length scale of the convection process and $D$ is the surface diffusion. If $Pe \gg 1$, fluids are transported in the direction of flow with small diffusion normal to the interface. This causes a severe film deformation, with a large leading-edge slope and a thinning of the film in the region preceding the front, reduced spreading exponents and the surfactant concentration accumulation near the center of the drop. On the other hand, a decrease in $Pe$ results in smaller degrees of film deformation and surfactant concentration variation along the surface of the liquid film (Afsar-Siddiqui et al., 2003). The effect of $Pe$ is shown in Figure 3.8.

In thick regions, Marangoni convection and hydrostatic pressure gradients have the opposite effects to the liquid film. The Marangoni convection causes disturbances of the initially flat film. On the other hand, hydrostatic pressure gradients induce flows that act to stabilize the disturbed film to a uniform thickness. The Bond number $B$ is used to express the relationship between these two mechanisms and is defined by (Gaver & Grotberg, 1990)

$$B = \frac{\rho H^2 g}{S}, \tag{3.43}$$

where $\rho$ is a constant density and $g$ is a gravitational acceleration. On the other word, the Bond number relates gravitational forces to surface tension forces. As shown in Figure 3.9, an increase in $B$ leads to diminished surface tension gradients, while the spreading exponents and surfactant concentration gradients shows insignificant difference for different values of $B$. Flow reversal can exist when hydrostatic forces overcome the Marangoni convection. This flow reversal causes fluids to move from the thick regions to the thin regions, resulting in a relaxation of film thickness as shown in Figure 3.10.

Gaver & Grotberg (1992) also carried out an experiment to investigate the spreading behaviour of oleic acid on a thin glycerol film to investigate the effect of the Bond number by varying the film height. Their experimental results support their theoretical results (Gaver & Grotberg, 1990).

So far we have been focusing solely on the effect of insoluble surfactant. Models of soluble surfactant have also drawn some author's attention.

Halpern & Grotberg (1992a) considered a soluble surfactant spreading on a liquid film, which lies on a rigid substrate that is permeable to surfactant. For the case of soluble surfactant, the surfactant may diffuse across the air-liquid interface as well as along the

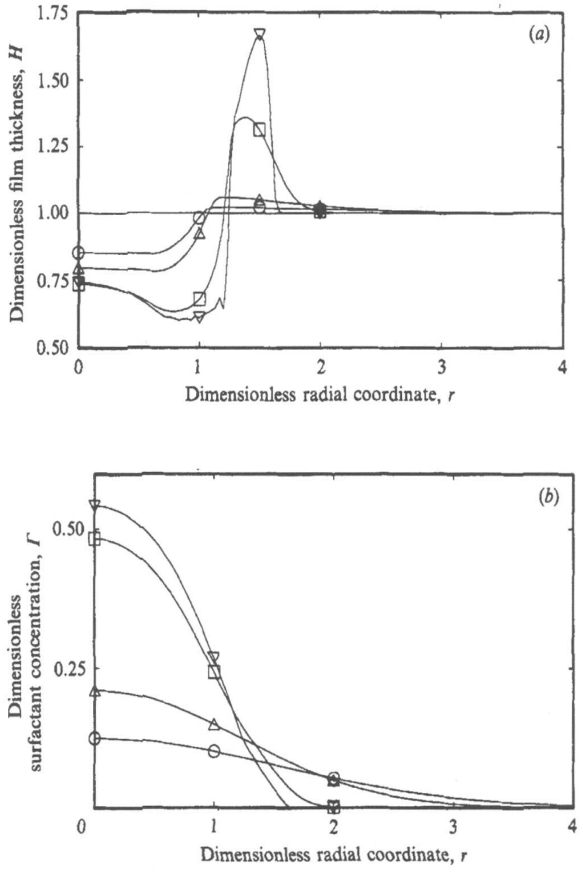



Figure 3.8: (a) Film thickness and (b) surfactant concentration profiles along the radial distance for ◯ $Pe$=0.5; △ $Pe$=1.0; □ $Pe$=10; ▽ $Pe$=100. The Bond number is held at constant at 0 at time $t = 0.5$. Reproduced from Gaver & Grotberg (1990).

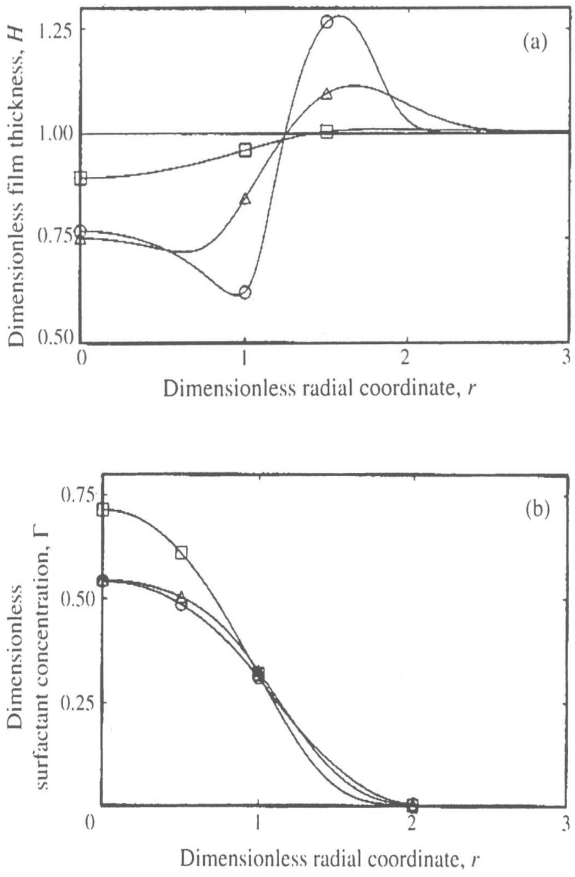



Figure 3.9: (a) Film thickness and (b) surfactant concentration profiles along the radial distance at time $t = 0.5$ for ◯ $B$=0.1; △ $B$=1.0; □ $B$=10.0. The Peclet number is held at constant at 10. Reproduced from Gaver & Grotberg (1990).

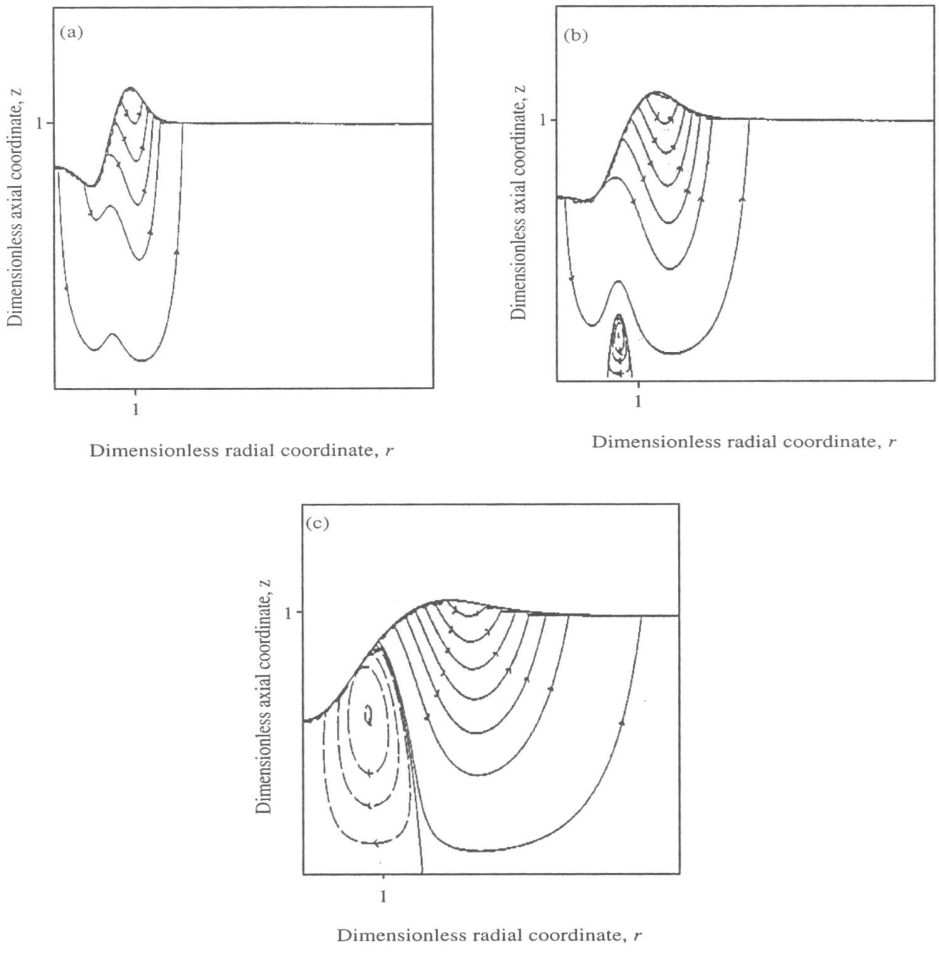



Figure 3.10: Streamlines of a velocity field (a) $t = 0.5$; (b) $t = 0.75$; (c) $t = 3.0$ for $Pe$=10.0, $B$=1.0. Reproduced from Gaver & Grotberg (1990).

interface. The adsorption of surfactant from the liquid film to the substrate depends on the film thickness, *i.e.*, surface tension at thin regions is lower than in thick regions. This surface-tension gradient in liquid layer induces a backflow in the region behind the moving front, as shown in Figure 3.11. This phenomenon is not observed in the insoluble surfactant case when the gravity is absent.

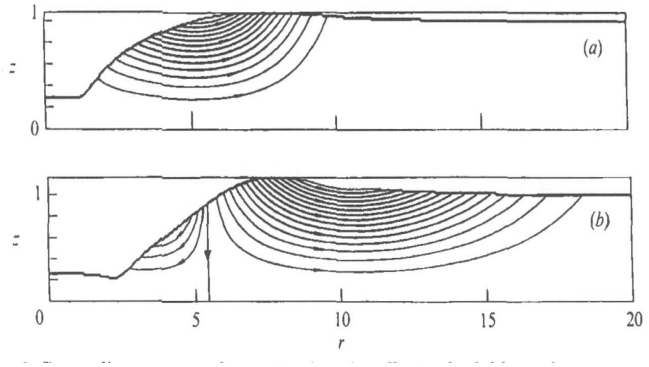



Figure 3.11: Streamlines showing the effects of soluble surfactant, without the gravitational effects, at (a) $t = 200$ and (b) $t = 1000$. Reproduced from Halpern & Grotberg (1992a).

## 3.4 Moving contact line

The problem of a viscous liquid spreading over a solid substrate is one of the major outstanding problems in fluid mechanics. One approach to this problem is by performing the investigation within the framework of the lubrication approximation in which we assume the height of the drop is small compared with its lateral extent. Accordingly, the Navier-Stokes equations subject to the no-slip condition reduce to a two-dimensional nonlinear fourth-order partial differential equation (3.30). However, the motion of the fluid interface and the behavior of the fluid in the vicinity of the contact line (three-phase-line) must be accounted for in the physical formulation.

Huh & Scriven (1971) showed that, under the classical no-slip boundary condition, the viscous stress and the rate of energy dissipation have non-integrable singularities in the neighborhood of the contact line. Shikhmurzaev (2006) gave the qualitative argument that, with the no-slip condition, the pressure is reduced in the neighborhood of the contact line. Consequently, the Capillary force from the normal-stress boundary condition acts to compensate the pressure difference in the air and in the liquid by bending the free surface toward the air. However, the effect of the no-slip condition is so strong causing an infinite Capillary force required to overcome the pressure difference. In the last past couples of decade, numerous authors have attempted to solve this difficulty. There are two remedies which have always been proposed: employing a slip boundary condition and employing a precursor film. Neverthesless, this moving-contact-line problem has still remained the topic of discussion among researchers. In this section, we will make a brief discussion. Further details can be found in de Gennes (1985).

### 3.4.1 Navier slip condition

Huh & Scriven (1971) first suggested that a local slip boundary condition would remove the infinite-force singularities and it has been proved that it does in fact alleviate the problem (Dussan V., 1976). This technique allows slip between the solid and the fluid. In the two-dimensional version of this model in the $(x, y)$-plane with the fluid in $y > 0$ and a rigid substrate at $y = 0$, the fluid velocity $u(x, y, t)$ parallel to the interface is proportional to the strain rate, *i.e.*

$$u = \lambda(h)\frac{\partial u}{\partial y} \qquad \text{on} \qquad y = 0, \tag{3.44}$$

where $\lambda(h)$ is a slip coefficient with units of length, which is small away from the contact line, where $h = O(1)$. Typically, $\lambda(h) = a(h^n)$ where $a$ is a small parameter (in general, of the order of molecular length scales), and $0 \leq n \leq 2$. Therefore, this condition will be neglected except in the immediate neighborhood of the contact line where $\partial u/\partial y$ is large. Greenspan (1978) used $\lambda(h) = a/3h$, while Hocking (1981) considered $n = 0$.

Once we substitute (3.44) into (3.45) instead of the no-slip condition, we have the modified thin liquid film equation

$$h_t + \left(\left(\frac{h^3}{3} + \lambda(h)h^2\right)(Ch_{xxx} - \delta Sth_x\cos\alpha + B\sin\alpha) + \frac{M}{2}h^2\sigma_{1,x}\right) = 0. \tag{3.45}$$

### 3.4.2 Precursor film

This model assumes the existence of a thin precursor film ahead of a moving contact line leading to the removal of singularity at the contact line. This model also allows the no-slip condition to be valid.

In the complete wetting situation, the properties of a liquid drop spreading on a solid substrate can be divided into macroscopic and microscopic properties. Near the centre of a small liquid drop, the long range forces play no role and the spreading is principally driven by macroscopic Capillary forces, while a larger drop, the main driving force is gravity, and the viscous force acts to resist its motion. Near the very edge of the drop, the liquid film becomes thin, and the long-range fluid/solid interactions are the only driving forces for the microscopic precursor film.

In the macroscopic aspects of the spreading kinetics of the drop, the spreading motion is decoupled from the spreading of precursor film which is governed by spreading coefficient $S$. In a quasi-steady state, the drop's shape evolves through the Young-Laplace equation and the velocity dependence of the apparent contact angle obeys a simple cubic power-law, known as Tanner's law (Kavehpour et al., 2003),

$$\theta \sim Ca^{1/3} \tag{3.46}$$

where $\theta$ is the apparent contact angle and $Ca = \mu U/\sigma$ is the Capillary number. Here $\mu$ and $\sigma$ are the constant viscosity and surface tension of the liquid and $U$ is the spreading velocity of the drop.

In the very edge of an advacing liquid front, the liquid thickness becomes small and we can no longer neglect the incorporation of the long-range forces. This is viewed as a microscopic region. The length of the precursor film is an increasing function of $S^{1/2}$ which implies that the precursor is longer and thinner on surfaces with larger $S$ ( higher free energy ) and its tip can no longer be described by hydrodynamic theories. But when the spreading

coefficient $S$ is small, the precursor is relatively thick and continuum theory applies (Gennes et al., 1990). To solve a problem analytically, the matching region is required to couple the macroscopic and microscopic regions, as shown in Figure 3.12.

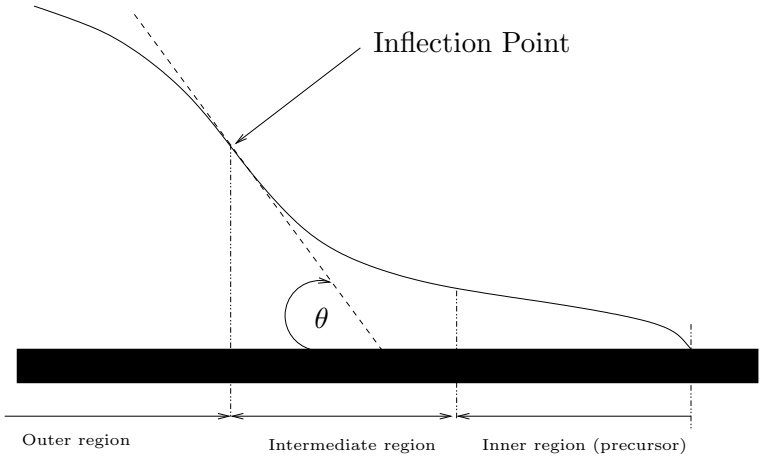



Figure 3.12: Diagram showing the precursor film advancing ahead of the fluid drop where $\theta$ is the apparent contact angle of the drop.

## 3.5 Conclusion

In this chapter, we study a diverse range of thin film flows. The general thin film equation based on the lubrication theory is derived. Thin film stability analyses in both rigid and elastic straight tubes are described. Stability analyses are essential to predict regions of low film thickness in the range where intermolecular forces can come into play, leading to thin film rupture. The basic approach is by using a linear analysis, however, it becomes generally invalid when the disturbances grow to the order of the film thickness.

A great deal of work on both soluble and insoluble surfactant spreading phenomena on thin liquid films has experience a surge of activity, partly due to the biomedical applications of surfactant replacement treatment in prematurely born baby. Early models used to describe flows in airways usually neglect the potentially important effects, such as, the non-uniformity of liquid lining thickness due to variations in airway wall curvature, some effects at bifurcations, and air frictions. These models are subsequently improved by including the presence of aqueous and mucus layers which is done by Moriarty & Grotberg (1999). Lastly, the violation of the no-slip condition in the neighborhood of the moving contact line is discussed, with the two main remedies for this singularity at the contact line.

# Chapter 4

# Thin liquid film on curved substrates

## 4.1 Introduction

Thin-film flows on curved substrates are fundamentally important to numerous diverse applications both in industry and natural processes. This has motivated the development of theoretical models of such flows to gain more understanding. To model such flows, the lubrication approximation of the Navier-Stokes equations is the starting point. There has been some work done both for stationary, and moving curved substrates (Van De Fliert et al., 1995; Ida & Miksis, 1998; Howell, 2003); however, we will study only thin film flows on a stationary curved substrate.

Schwartz & Weidner (1995) are considered to be the pioneers in this research by considering the two-dimensional model. Roy et al. (2002) developed a more complex model by considering the Navier-Stokes equations in a three-dimensional orthogonal curvilinear coordinate system in which the substrate is stationary. The derivation of the evolution equation is similar to the one in §4.1 except they included some higher-order corrections which effectively smooth out any possible singularities that may arise in the leading order hyperbolic equation (when the substrate curvature is large). Roberts & Li (2006) extended the models by Roy et al. (2002) by solving the full Navier-Stokes equations at higher Reynolds numbers. They derived the coupled partial differential equations for the film thickness and the averaged velocity, based on centre manifold theory which describes the long-time dynamics near a steady state resulting in a lower dimensional model. The effects of inertia, gravity, surface tension and substrate curvature are included. Their modified equations rely heavily on their computation where higher order terms are included. In this chapter, we will follow the steps to deriving the master equation governing thin-film flows over a stationary, curved substrate in §4.1, based on the papers by Howell (2003), Roy et al. (2002) and the book by Warsi (2006). In §4.2, some examples of flows on some particular curved substrates will be shown.

## 4.2 Derivation of the master thin-film equation

By introducing an orthogonal curvilinear coordinate system $(x_1, x_2, n)$ as follows and as illustrated in Figure 4.1, we parameterize the curved substrate by writing

$$\boldsymbol{r}_c = \boldsymbol{r}_c(x_1, x_2). \tag{4.1}$$

We define the unit vectors in the directions of the surface coordinates by

$$\boldsymbol{e}_1 = \frac{1}{a_1}\frac{\partial \boldsymbol{r}_c}{\partial x_1}, \qquad \boldsymbol{e}_2 = \frac{1}{a_2}\frac{\partial \boldsymbol{r}_c}{\partial x_2}, \tag{4.2}$$

and the unit normal by

$$\boldsymbol{n} = \boldsymbol{e}_1 \wedge \boldsymbol{e}_2, \tag{4.3}$$

where

$$a_1 = \left|\frac{\partial \boldsymbol{r}_c}{\partial x_1}\right|, \qquad a_2 = \left|\frac{\partial \boldsymbol{r}_c}{\partial x_2}\right|. \tag{4.4}$$

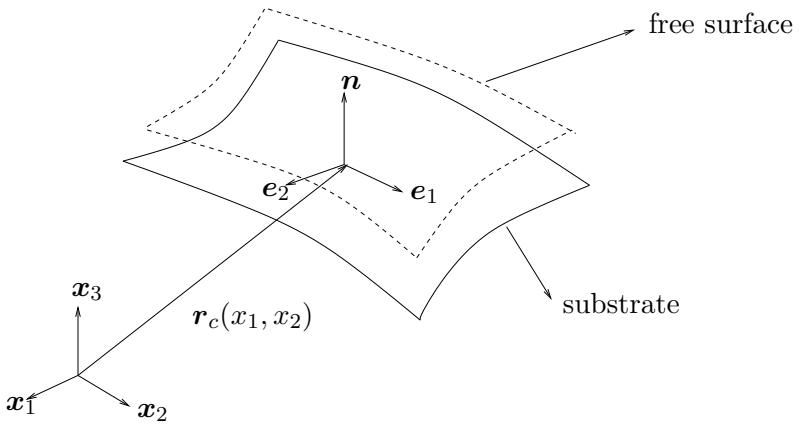



Figure 4.1: Schematic of a thin-liquid film over a stationary curved substrate.

The position vector of a point in the liquid is written as

$$\boldsymbol{r} = \boldsymbol{r}_c + n\boldsymbol{n}, \tag{4.5}$$

where $\boldsymbol{n} = \boldsymbol{n}(x_1, x_2)$. The scale factors are given by

$$\left|\frac{\partial \boldsymbol{r}}{\partial x_1}\right| = \quad l_1 = \quad a_1(1 - \kappa_1 n), \tag{4.6}$$

$$\left|\frac{\partial \boldsymbol{r}}{\partial x_2}\right| = \quad l_2 = \quad a_2(1 - \kappa_2 n), \tag{4.7}$$

$$\left|\frac{\partial \boldsymbol{r}}{\partial n}\right| = \quad l_3 = \quad 1, \tag{4.8}$$

where $\kappa_1$ and $\kappa_2$ are defined to be the principal curvatures of the substrate in the $x_1-$ and $x_2-$directions. The differential geometry of surfaces implies that (Ida & Miksis, 1998)

$$\frac{\partial \boldsymbol{n}}{\partial x_1} = -\kappa_1 a_1 \boldsymbol{e}_1, \qquad \frac{\partial \boldsymbol{n}}{\partial x_2} = -\kappa_2 a_2 \boldsymbol{e}_2, \tag{4.9}$$

and

$$\frac{\partial \boldsymbol{e}_1}{\partial x_1} = \frac{\partial \boldsymbol{e}_2}{\partial x_1} \wedge \boldsymbol{n} + \kappa_1 a_1 \boldsymbol{n}, \qquad \frac{\partial \boldsymbol{e}_2}{\partial x_1} = \boldsymbol{n} \wedge \frac{\partial \boldsymbol{e}_1}{\partial x_1}, \tag{4.10}$$

$$\frac{\partial \boldsymbol{e}_1}{\partial x_2} = \frac{\partial \boldsymbol{e}_2}{\partial x_2} \wedge \boldsymbol{n}, \qquad \frac{\partial \boldsymbol{e}_2}{\partial x_2} = \kappa_2 a_2 \boldsymbol{n} + \boldsymbol{n} \wedge \frac{\partial \boldsymbol{e}_1}{\partial x_2}. \tag{4.11}$$

The gradient, divergent and curl have respectively expressions (Selvadurai, 2000):

$$grad\phi = \frac{1}{l_1}\frac{\partial \phi}{\partial x_1}\boldsymbol{e_1} + \frac{1}{l_2}\frac{\partial \phi}{\partial x_2}\boldsymbol{e_2} + \frac{1}{l_3}\frac{\partial \phi}{\partial n}\boldsymbol{n}, \tag{4.12}$$

$$div\boldsymbol{A} = \frac{1}{l_1 l_2 l_3}\left[\frac{\partial}{\partial x_1}(l_2 l_3 A_1) + \frac{\partial}{\partial x_2}(l_1 l_3 A_2) + \frac{\partial}{\partial n}(l_1 l_2 A_3)\right], \tag{4.13}$$

$$curl\boldsymbol{A} = \frac{\boldsymbol{e_1}}{l_2 l_3}\left[\frac{\partial}{\partial x_2}(l_3 A_3) - \frac{\partial}{\partial n}(l_2 A_2)\right] + \frac{\boldsymbol{e_2}}{l_1 l_3}\left[\frac{\partial}{\partial n}(l_1 A_1) - \frac{\partial}{\partial x_1}(l_3 A_3)\right] + \frac{\boldsymbol{n}}{l_1 l_2}\left[\frac{\partial}{\partial x_1}(l_2 A_2) - \frac{\partial}{\partial x_2}(l_1 A_1)\right], \tag{4.14}$$

where $\phi$ is any scalar function and $\boldsymbol{A}$ is an arbitrary vector $\boldsymbol{A} = A_1\boldsymbol{e_1} + A_2\boldsymbol{e_2} + A_3\boldsymbol{n}$.

### 4.2.1 Governing equations and boundary conditions

The flow is governed by the Navier-Stokes equations for an incompressible Newtonian fluid of constant density $\rho$ and constant viscosity $\mu$. We denote the fluid pressure by $p(x_1, x_2, n, t)$ and the velocity field by $\boldsymbol{u}(x_1, x_2, n, t) = u_1\boldsymbol{e}_1 + u_2\boldsymbol{e}_2 + u_3\boldsymbol{n}$. The fluid flow is driven by constant surface tension $\sigma$ only. Note that the mean curvature of the thin film recieves a contribution from the curvature of the substrate because the film is thin.

$$\rho\left(\frac{\partial \boldsymbol{u}}{\partial t} + (\boldsymbol{u}\cdot\boldsymbol{\nabla})\boldsymbol{u}\right) = -\boldsymbol{\nabla}p + \mu\boldsymbol{\nabla}^2\boldsymbol{u}, \tag{4.15}$$

$$\boldsymbol{\nabla}\cdot\boldsymbol{u} = 0. \tag{4.16}$$

No-slip and no-flux conditions give

$$\boldsymbol{u} = \boldsymbol{0}, \qquad \text{on} \qquad n = 0. \tag{4.17}$$

At the interface $n = h(x_1, x_2, t)$, we have the kinematic boundary condition

$$u_3 = \frac{\partial h}{\partial t} + (\boldsymbol{u_i}\cdot\boldsymbol{\nabla})h, \qquad \text{for} \qquad i = 1, 2. \tag{4.18}$$

The tangential stress condition gives

$$\hat{\boldsymbol{n}}\cdot\boldsymbol{T}\cdot\hat{\boldsymbol{t}}_{\boldsymbol{1}} = \hat{\boldsymbol{n}}\cdot\boldsymbol{T}\cdot\hat{\boldsymbol{t}}_{\boldsymbol{2}} = 0, \qquad \text{on} \qquad n = h(x_1, x_2, t), \tag{4.19}$$

where $\hat{\boldsymbol{t}}_{\boldsymbol{1}}$ and $\hat{\boldsymbol{t}}_{\boldsymbol{2}}$ are independent tangential vectors to $n = h$ in the $x_1-$ and $x_2-$directions respectively, and $\hat{\boldsymbol{n}}$ is the unit normal to $n = h$. The stress tensor $\boldsymbol{T}$ has components $T_{ij}$

for $i, j = 1, 2, 3$ given as follows (Van De Fliert et al., 1995; Roy et al., 2002):

$$T_{11} = -p + \frac{2\mu}{l_1}\left(\frac{\partial u_1}{\partial x_1} + \frac{u_2}{l_2}\frac{\partial l_1}{\partial x_2} + u_3\frac{\partial l_1}{\partial n}\right), \tag{4.20}$$

$$T_{22} = -p + \frac{2\mu}{l_2}\left(\frac{\partial u_2}{\partial x_2} + \frac{u_1}{l_1}\frac{\partial l_2}{\partial x_1} + u_3\frac{\partial l_2}{\partial n}\right), \tag{4.21}$$

$$T_{33} = -p + 2\mu\frac{\partial u_3}{\partial n}, \tag{4.22}$$

$$T_{12} = \frac{\mu}{l_1 l_2}\left(l_1\frac{\partial u_1}{\partial x_2} - u_1\frac{\partial l_1}{\partial x_2} + l_2\frac{\partial u_2}{\partial x_1} - u_2\frac{\partial l_2}{\partial x_1}\right), \tag{4.23}$$

$$T_{13} = \mu\left(\frac{\partial u_1}{\partial n} - \frac{u_1}{l_1}\frac{\partial l_1}{\partial y} + \frac{1}{l_1}\frac{\partial u_3}{\partial x_1}\right), \tag{4.24}$$

$$T_{23} = \mu\left(\frac{\partial u_2}{\partial n} - \frac{u_2}{l_2}\frac{\partial l_2}{\partial y} + \frac{1}{l_2}\frac{\partial u_3}{\partial x_2}\right). \tag{4.25}$$

We shall use the tangential vectors

$$\hat{\boldsymbol{t}}_{\boldsymbol{i}} = \frac{\partial \boldsymbol{r}}{\partial x_i} = \frac{1}{c_i}\left(m_i \boldsymbol{e}_i + \frac{\partial h}{\partial x_i}\boldsymbol{n}\right), \tag{4.26}$$

where $m_i = a_i(1 - \kappa_i h)$ and $c_i$ is a normalization constant (for $i = 1, 2$). The unit normal vector, $\hat{\boldsymbol{n}}$, is given by

$$\begin{aligned}\hat{\boldsymbol{n}} &= \frac{\hat{\boldsymbol{t}}_{\boldsymbol{1}} \wedge \hat{\boldsymbol{t}}_{\boldsymbol{2}}}{|\,\hat{\boldsymbol{t}}_{\boldsymbol{1}} \wedge \hat{\boldsymbol{t}}_{\boldsymbol{2}}\,|}, \\ &= \frac{1}{c_3}\left(m_1 m_2 \boldsymbol{n} - m_2\frac{\partial h}{\partial x_1}\boldsymbol{e}_1 - m_1\frac{\partial h}{\partial x_2}\boldsymbol{e}_2\right),\end{aligned} \tag{4.27}$$

where $c_3$ is a constant of normalization. The normal stress condition is given by

$$\hat{\boldsymbol{n}} \cdot \boldsymbol{T} \cdot \hat{\boldsymbol{n}} = \sigma\kappa, \qquad \text{on} \qquad n = h, \tag{4.28}$$

where $\kappa$ is twice the mean curvature of the free surface.

### 4.2.2 Nondimensionalization and scaling

We assume the fluid layer has a typical length scale $L$ and a typical radius of curvature $a$. The thickness of fluid layer is assumed to be thin so that, if $\hat{h}$ is a typical thickness scale, and then $\delta = \hat{h}/L \ll 1$. We determine typical velocity and pressure scales from the normal stress boundary condition (4.28). The nondimensionalization of the equations and boundary conditions are as follows:

$$\begin{gathered} x_i = L x_i^*, \qquad i = 1, 2, \qquad n = \delta n^*, \\ u_i = \frac{\delta^2 \sigma L}{a\mu} u_i^*, \qquad i = 1, 2, \qquad u_3 = \frac{\delta^3 \sigma L}{a\mu} u_3^*, \\ \kappa = \frac{1}{a}\kappa^*, \qquad t = \frac{a\mu}{\delta^2\sigma} t^*, \qquad p = \frac{\sigma}{a} p^*. \end{gathered}$$

The incompressibility condition (4.16) becomes (dropping asterisks for convenience)

$$\frac{\partial}{\partial x_1}(l_2 u_1) + \frac{\partial}{\partial x_2}(l_1 u_2) + \frac{\partial}{\partial n}(l_1 l_2 u_3) = 0, \tag{4.29}$$

and the three momentum equations in a component form are:
$\boldsymbol{e}_1-$direction:

$$\delta^4 Re\left(\frac{\partial u_1}{\partial t}+\frac{u_1}{l_1}\frac{\partial u_1}{\partial x_1}+\frac{u_2}{l_2}\frac{\partial u_1}{\partial x_2}+u_3\frac{\partial u_1}{\partial n}+\frac{u_1u_2}{l_1l_2}\frac{\partial l_1}{\partial x_2}-\frac{u_2^2}{l_1l_2}\frac{\partial l_2}{\partial x_1}+\frac{u_1u_2}{\delta l_1}\frac{\partial l_1}{\partial n}\right)= -\frac{1}{l_1}\frac{\partial p}{\partial x_1}+\frac{1}{l_1l_2}\left[\delta^2\frac{\partial}{\partial x_1}\left(\frac{l_2}{l_1}\frac{\partial u_1}{\partial x_1}\right)+\delta^2\frac{\partial}{\partial x_2}\left(\frac{l_1}{l_2}\frac{\partial u_1}{\partial x_2}\right)+\frac{\partial}{\partial n}\left(l_1l_2\frac{\partial u_1}{\partial n}\right)\right], \quad (4.30)$$

$\boldsymbol{e}_2-$direction:

$$\delta^4 Re\left(\frac{\partial u_2}{\partial t}+\frac{u_1}{l_1}\frac{\partial u_2}{\partial x_1}+\frac{u_2}{l_2}\frac{\partial u_2}{\partial x_2}+u_3\frac{\partial u_2}{\partial n}+\frac{u_1u_2}{l_1l_2}\frac{\partial l_2}{\partial x_1}-\frac{u_1^2}{l_1l_2}\frac{\partial l_1}{\partial x_2}+\frac{u_2u_3}{l_2}\frac{\partial l_2}{\partial n}\right)= -\frac{1}{l_2}\frac{\partial p}{\partial x_2}+\frac{1}{l_1l_2}\left[\delta^2\frac{\partial}{\partial x_1}\left(\frac{l_2}{l_1}\frac{\partial u_2}{\partial x_1}\right)+\delta^2\frac{\partial}{\partial x_2}\left(\frac{l_1}{l_2}\frac{\partial u_2}{\partial x_2}\right)+\frac{\partial}{\partial n}\left(l_1l_2\frac{\partial u_2}{\partial n}\right)\right], \quad (4.31)$$

$\boldsymbol{n}-$direction:

$$\delta^6 Re\left(\frac{\partial u_3}{\partial t}+\frac{u_1}{l_1}\frac{\partial u_3}{\partial x_1}+\frac{u_2}{l_2}\frac{\partial u_3}{\partial x_2}+u_3\frac{\partial u_3}{\partial n}-\frac{u_1^2}{\delta^2 l_1}\frac{\partial l_1}{\partial n}-\frac{u_3^2}{l_2}\frac{\partial l_2}{\partial n}\right)=-\frac{\partial p}{\partial n}+ \frac{1}{l_1l_2}\left[\delta^4\frac{\partial}{\partial x_1}\left(\frac{l_2}{l_1}\frac{\partial u_3}{\partial x_1}\right)+\delta^4\frac{\partial}{\partial x_2}\left(\frac{l_1}{l_2}\frac{\partial u_3}{\partial x_2}\right)+\delta^2\frac{\partial}{\partial n}\left(l_1l_2\frac{\partial u_3}{\partial n}\right)\right], \quad (4.32)$$

where $Re=\rho L^2\sigma/a\mu^2$ is the Reynolds number.

At the interface $n=h(x_1,x_2,t)$, the kinematic boundary condition becomes

$$u_3=\frac{\partial h}{\partial t}+\frac{u_1}{a_1}\frac{\partial h}{\partial x_1}+\frac{u_2}{a_2}\frac{\partial h}{\partial x_2}. \quad (4.33)$$

The scaled components of the nondimensional stress tensor in the $(x_1,x_2,n)$ system are given by

$$\begin{aligned}
T_{11} &= -p+\frac{2\delta^2}{l_1}\left(\frac{\partial u_1}{\partial x_1}+\frac{u_2}{l_2}\frac{\partial l_1}{\partial x_2}+u_3\frac{\partial l_1}{\partial n}\right), && (4.34)\\
T_{22} &= -p+\frac{2\delta^2}{l_2}\left(\frac{\partial u_2}{\partial x_2}+\frac{u_1}{l_1}\frac{\partial l_2}{\partial x_1}+u_3\frac{\partial l_2}{\partial n}\right), && (4.35)\\
T_{33} &= -p+2\delta^2\frac{\partial u_3}{\partial n}, && (4.36)\\
T_{12} &= \frac{\delta^2}{l_1l_2}\left(l_1\frac{\partial u_1}{\partial x_2}-u_1\frac{\partial l_1}{\partial x_2}+l_2\frac{\partial u_2}{\partial x_1}-u_2\frac{\partial l_2}{\partial x_1}\right), && (4.37)\\
T_{13} &= \frac{\delta}{l_1}\left(l_1\frac{\partial u_1}{\partial n}-u_1\frac{\partial l_1}{\partial n}+\delta^2\frac{\partial u_3}{\partial x_1}\right), && (4.38)\\
T_{23} &= \frac{\delta}{l_2}\left(l_2\frac{\partial u_2}{\partial n}-u_2\frac{\partial l_2}{\partial n}+\delta^2\frac{\partial u_3}{\partial x_2}\right), && (4.39)
\end{aligned}$$

and the scaled tangential and normal unit vectors are given by

$$\begin{aligned}
\hat{\boldsymbol{t}}_{\boldsymbol{i}} &= \frac{1}{C_i}\left(a_1(1-\delta\kappa_i h)\boldsymbol{e}_i+\delta\frac{\partial h}{\partial x_i}\boldsymbol{n}\right), && (4.40)\\
\hat{\boldsymbol{n}} &= \frac{1}{C_3}\left(-\delta a_2(1-\delta\kappa_1 h)\frac{\partial h}{\partial x_1}\boldsymbol{e}_1-\delta a_1(1-\delta\kappa_2 h)\frac{\partial h}{\partial x_2}\boldsymbol{e}_2\right)\\
&\quad +\frac{1}{C_3}\left(a_1a_2(1-\delta h\kappa_1)(1-\delta h\kappa_2)\boldsymbol{n}\right), && (4.41)
\end{aligned}$$

where $C_i$ and $C_3$ are the constants of normalization, for $i = 1, 2$.

In lubrication theory, we assume that $\delta$, $\delta^2 Re \ll 1$. Thus, the leading-order governing equations are given by

$$\frac{1}{a_1}\frac{\partial p}{\partial x_1} = \frac{\partial^2 u_1}{\partial n^2}, \tag{4.42}$$

$$\frac{1}{a_2}\frac{\partial p}{\partial x_2} = \frac{\partial^2 u_2}{\partial n^2}, \tag{4.43}$$

$$\frac{\partial p}{\partial n} = 0, \tag{4.44}$$

since $l_i = a_i(1 - \delta\kappa_i y) \sim a_i$ for $i = 1, 2$.

At leading order, the boundary conditions at the free surface $n = h(x_1, x_2, t)$ become

$$u_3 = \frac{\partial h}{\partial t} + \frac{u_1}{a_1}\frac{\partial h}{\partial x_1} + \frac{u_2}{a_2}\frac{\partial h}{\partial x_2}, \tag{4.45}$$

$$p = -\kappa, \tag{4.46}$$

$$\frac{\partial u_1}{\partial n} = \frac{\partial u_2}{\partial n} = 0, \tag{4.47}$$

and on $n = 0$

$$\boldsymbol{u} = \boldsymbol{0}. \tag{4.48}$$

Integrating (4.29) with respect to $n$ from $n = 0$ to $n = h(x_1, x_2, t)$ and applying (4.45) together with the no-flux condition on the substrate gives

$$\begin{aligned} -\int_0^h \frac{\partial}{\partial x_1}(a_2 u_1)\, dn - \int_0^h \frac{\partial}{\partial x_2}(a_1 u_2)\, dn &= -\int_0^h \frac{\partial}{\partial n}(a_1 a_2 u_3)\, dn, \\ &= a_1 a_2 \frac{\partial h}{\partial t} + u_1 a_2 \frac{\partial h}{\partial x_1} + u_2 a_1 \frac{\partial h}{\partial x_2}. \end{aligned} \tag{4.49}$$

Since, by

$$-\frac{\partial}{\partial x_1}\int_0^h (a_2 u_1)\, dn = -\int_0^h \frac{\partial}{\partial x_1}(a_2 u_1)\, dy - a_2 u_1 \frac{\partial h}{\partial x_1}, \tag{4.50}$$

$$-\frac{\partial}{\partial x_2}\int_0^h (a_1 u_2)\, dn = -\int_0^h \frac{\partial}{\partial x_2}(a_1 u_2)\, dy - a_1 u_2 \frac{\partial h}{\partial x_2}. \tag{4.51}$$

We deduce that

$$a_1 a_2 \frac{\partial h}{\partial t} + \frac{\partial Q_1}{\partial x_1} + \frac{\partial Q_2}{\partial x_2} = 0, \tag{4.52}$$

where the fluxes are given by

$$Q_1 = \int_0^h a_2 u_1\, dn, \qquad Q_2 = \int_0^h a_1 u_2\, dn. \tag{4.53}$$

By (4.44), $p$ is independent of $n$ and from (4.46), it implies $p = -\kappa(x_1, x_2, t)$.

Solving equations (4.42) and (4.43) for $u_1$ and $u_2$, using (4.47) and the no-slip condition gives

$$Q_1 = -\frac{h^3}{3}\frac{a_2}{a_1}\frac{\partial p}{\partial x_1}, \tag{4.54}$$

$$Q_2 = -\frac{h^3}{3}\frac{a_1}{a_2}\frac{\partial p}{\partial x_2}. \tag{4.55}$$

Thus, using the condition (4.46), the governing equation for the film thickness $h$ is

$$\frac{\partial h}{\partial t} + \nabla_s \cdot \left( \frac{h^3}{3} \boldsymbol{\nabla}_s \kappa \right) = 0, \tag{4.56}$$

where $\nabla_s$ is the surface gradient operator, so that

$$\boldsymbol{\nabla}_s \kappa = \frac{\partial \kappa}{\partial x_1} \frac{\boldsymbol{e}_1}{a_1} + \frac{\partial \kappa}{\partial x_2} \frac{\boldsymbol{e}_2}{a_2}, \tag{4.57}$$

and

$$\boldsymbol{\nabla}_s \cdot (q_1 \boldsymbol{e_1} + q_2 \boldsymbol{e_2}) = \frac{1}{a_1 a_2} \left( \frac{\partial}{\partial x_1}(a_2 q_1) + \frac{\partial}{\partial x_2}(a_1 q_2) \right). \tag{4.58}$$

### 4.2.3 Substrate curvature

Howell (2003) expanded the expression $\kappa = \boldsymbol{\nabla}_s \hat{\boldsymbol{n}}$ to obtain

$$\kappa \sim (\kappa_1 + \kappa_2) + \delta({\kappa_1}^2 + {\kappa_2}^2)h + \delta \boldsymbol{\nabla}^2 h, \qquad \text{as} \qquad s \to 0 \tag{4.59}$$

and considered the following three distinguished limits.

#### 4.2.3.1 Small curvature

In this regime, the substrate is relatively flat so that the substrate curvatures are of the same order as the thin film curvature. Thus, plane Cartesian coordinates can be used. By rescaling $L/a = \delta$, the leading order of (4.59) is $\kappa_1 + \kappa_2 + \boldsymbol{\nabla}^2 h$. Therefore, the equation (4.56) becomes

$$\frac{\partial h}{\partial t} + \boldsymbol{\nabla} \cdot \left( \frac{h^3}{3} \boldsymbol{\nabla} (\hat{\kappa} + \boldsymbol{\nabla}^2 h) \right) = 0, \tag{4.60}$$

where $\hat{\kappa} = \kappa_1 + \kappa_2$. If the substrate is completely flat, (4.60) reduces to the thin-film equation for surface-tension-driven flow on a plane.

#### 4.2.3.2 Nearly constant curvature

When the mean curvature is approximately constant, we rescale the typical curvature scale $1/a$ such that $a = L$. Then the free surface curvature becomes

$$\kappa \sim 1 + \delta({\kappa^2}_1 + {\kappa^2}_2)h + \delta \boldsymbol{\nabla}^2 h. \tag{4.61}$$

The constant term on the right hand side may be absorbed into the pressure. To make the time-dependent term in (4.56) the same order as the curvature term, we can rescale $t$ such that

$$t = \frac{a\mu}{\delta\sigma} t^*, \tag{4.62}$$

to give (dropping asterisk)

$$\frac{\partial h}{\partial t} + \boldsymbol{\nabla}_s \cdot \left( \frac{h^3}{3} \boldsymbol{\nabla}_s ({({\kappa^2}_1 + {\kappa^2}_2)h + {\boldsymbol{\nabla}_s}^2 h}) \right) = 0. \tag{4.63}$$

#### 4.2.3.3 Large curvature

In this regime, the substrate curvature dominates other terms so that the governing equation takes the form

$$\frac{\partial h}{\partial t} + \boldsymbol{\nabla}_s \cdot \left( \frac{h^3}{3} \boldsymbol{\nabla}_s \hat{\kappa} \right) = 0, . \tag{4.64}$$

This is a hyperbolic equation which can be solved relatively easy for $\boldsymbol{r_c} = \boldsymbol{r_c}(x_1)$ or $\boldsymbol{r_c} = \boldsymbol{r_c}(x_2)$ using the method of characteristics (an example will be shown in §4.2). Howell (2003) analyzed the possibility of shock formation in which characteristic curves intersect leading to the system to have a multi-valued solution. The weak solution that requires less smoothness is found.

## 4.3 Examples of film flows on curved substrates

Schwartz & Weidner (1995) presented an analytical approach to the two-dimensional problem using a local orthogonal coordinate system $(s, n)$ where $s$ and $n$ are the coordinates tangential and normal to the substrate respectively. By including the effect of substrate curvature and applying the lubrication theory, the dimensionless evolution equation for the thickness of thin film is

$$\frac{\partial h}{\partial t} + \frac{\partial}{\partial s} \left[ \frac{h^3}{3} \frac{\partial}{\partial s} \left( \kappa + \frac{\partial^2 h}{\partial s^2} \right) \right] = 0, \tag{4.65}$$

where $\kappa$ is the substrate curvature. Note that the equation (4.65) is simply an example of §4.1.3.1 for a two-dimensional system when the substrate curvature is assumed to be small.

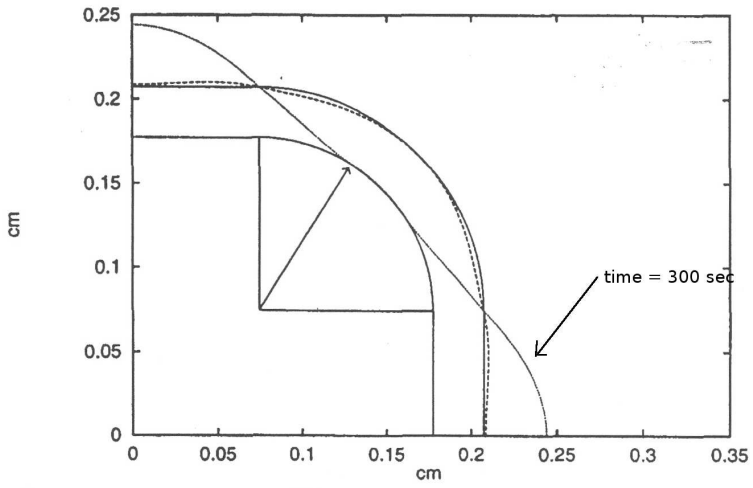



Figure 4.2: A coating flow on an outside of a corner at time 300 s. Reproduced from Schwartz & Weidner (1995).

Schwartz & Weidner (1995) used a finite-difference method to obtain numerical solutions to (4.65). Figure 4.2 illustrates the thinning of thin liquid film on an outside of a corner at later time. At time $t = 300$, the liquid film is thinned over a portion of the corner arc, and the film becomes thicknen when it is away from the corner arc.

To investigate the effect of substrate curvature qualitatively, we suppose that the flow is principally driven by substrate curvature gradient, *i.e.* the curvature variation caused by

the liquid-thin film is much smaller, *i.e.* $|\frac{\partial^2 h}{\partial s^2}| \ll \kappa$. Thus the equation (4.65) becomes

$$\frac{\partial h}{\partial t} + \frac{1}{3}\frac{\partial}{\partial s}(h^3 \kappa_s) = 0. \tag{4.66}$$

where the subscript $s$ denotes the partial differentiation with respect to $s$. The characteristic equations are

$$\frac{\mathrm{d}s}{\mathrm{d}t} = h^2 \kappa_s, \qquad \frac{\mathrm{d}h}{\mathrm{d}t} = -\frac{1}{3} h^3 \kappa_{ss}. \tag{4.67}$$

If the curvature has a local minimum at $s = s_0$, then

$$\kappa_s(s < s_0) < 0, \qquad \kappa_s(s > s_0) > 0, \tag{4.68}$$

results in $\kappa_{ss} > 0$. Solving (4.67) in the region of the minimum curvature gives

$$h(s,t) = (\kappa_{ss} t)^{-1/2} + C, \tag{4.69}$$

where C is a constant. This shows that the film thickness decreases as time increases at the point of a local minimum of the curvature. Figure 4.3 illustrates this result.

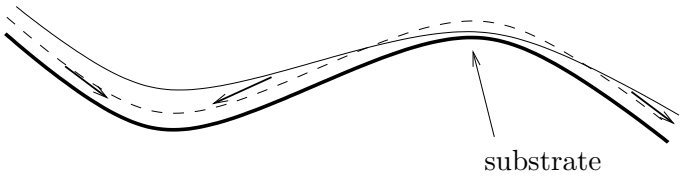



Figure 4.3: Schematic of a thin film evolution when the surface curvature is large.

Some examples of thin-film flows on a curved substrates will be presented as follows. We start by studying the dynamics of thin-film flows lining on a vertical cylinder. Quéré (1990) experimentally investigated an oil film a thick nylon fibre. The oil has constant surface tension $\sigma$ and density $\rho$. He found that if the oil film is perturbed and the film thickness exceeds a critical value $h_c$, given by

$$h_c \propto R^3 H^{-2}, \tag{4.70}$$

where $R$ the fibre radius and $H = (\sigma/\rho g)^{1/2}$ is the Capillary length, then small-amplitude waves on film can form Capillary drops triggered by the Rayleigh instability. Below $h_c$, the thin film saturates into solitary waves. His finding were theoretically studied by Kalliadasis & Chang (1994). They computed the solutions to a lubrication-type evolution equation for the film thickness and examined the critical conditions for the drop formation. Since the draining process is slow, the long-wave equation was solved using a matched asymptotic expansion which joins the Capillary outer region of the solitary wave to the thin-film inner region. They found $h_c = 1.68 R^3 H^{-2}$.

Roy et al. (2002) considered a torus that has a radius that extends from the centre of the hole to the centre of the torus tube $B$ and the radius of the torus tube $A$, as shown in Figure 4.4. An angle around the tube is defined by $\theta$ and around a rim of the torus by $\phi$. A thin liquid fluid is assumed to line outside the substrate.

The parametric equations for a torus are given by

$$\boldsymbol{r}_c(\theta,\phi) = (A + B\cos\theta)\cos\phi \boldsymbol{e_1} + (A + B\cos\theta)\sin\phi \boldsymbol{e_2} + B\sin\theta \boldsymbol{n}, \tag{4.71}$$

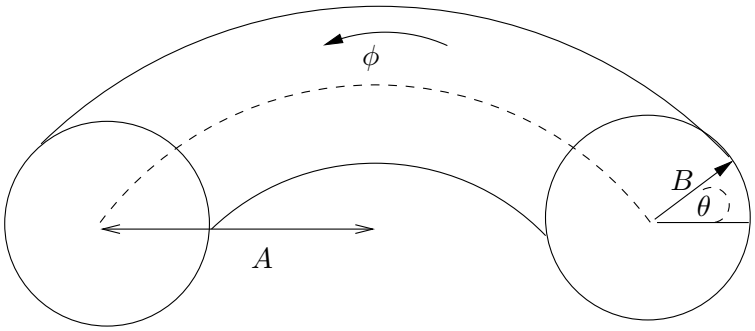



Figure 4.4: A sketch for a torus.

where

$$\boldsymbol{e_1} = \boldsymbol{e_\phi} = -\sin\phi\boldsymbol{i} + \cos\phi\boldsymbol{j}, \tag{4.72}$$

$$\boldsymbol{e_2} = \boldsymbol{e_\theta} = -\sin\theta\cos\phi\boldsymbol{i} - \sin\theta\sin\phi\boldsymbol{j} + \cos\theta\boldsymbol{k}, \tag{4.73}$$

$$\boldsymbol{n} = \cos\theta\cos\phi\boldsymbol{i} + \cos\theta\sin\phi\boldsymbol{i} + \sin\theta\boldsymbol{k}, \tag{4.74}$$

and $\phi$ and $\theta$ are in the interval $[0, 2\pi]$. The corresponding scale factors are

$$a_1 = A + B\cos\theta, \qquad a_2 = B. \tag{4.75}$$

Differentiating (4.74) with respect to $\phi$ and $\theta$ gives

$$\boldsymbol{n_\phi} = -\cos\theta\sin\phi\boldsymbol{i} + \cos\theta\cos\phi\boldsymbol{j}, \qquad \boldsymbol{n_\theta} = -\sin\theta\cos\phi\boldsymbol{i} - \sin\theta\sin\phi\boldsymbol{j} + \cos\theta\boldsymbol{k}. \tag{4.76}$$

Using (4.9), we then obtain the following principal curvatures and the mean curvature:

$$\kappa_1 = -\frac{\cos\theta}{A + B\cos\theta}, \qquad \kappa_2 = -\frac{1}{B}, \qquad \kappa = -\frac{1}{B}\frac{A + 2B\cos\theta}{A + B\cos\theta}. \tag{4.77}$$

From (4.77), the mean curvature of the torus is maximum at the inner rim where $\theta = \pi$, and is minimum at the outer rim $\theta = 0$ resulting in the higher pressure at the outer rim. Therefore, the fluid is expected to flow from the outer rim to inner rim causing the fluid to thicken around the inner rim and to thin around the outer. Roy et al. (2002) saught a periodic solution independent on $\phi$. Figure 4.5 illustrates the fluid coating the outside of the torus. However, if the fluid is assumed to be inside the tube, the curvature given by (4.77) has the opposite sign. Subsequently, the fluid flows from inner to outer (similar to the case studied by Jensen (1997)).

Jensen (1997) conducted a careful analysis of the thin liquid lining the interior of a cylindrical tube, with a weak dimensionless curvature ratio $\delta = a/R \ll 1$, where $a$ is the radius of the uniform circular cross-sectional tube, and $R$ is a radius of the circle, as illustrated in Figure 4.6. This flow structure is important biologically because most vessels within the body are not axially uniform, *e.g.* airways of the lungs, the blood vessels.

The orthogonal curvilinear coordinate system is used. Inertia and gravity are neglected, and the fluid flow is driven by surface tension. The fluid pressure at the inner wall is higher than the pressure at the outer wall. Therefore, azimuthal drainage takes place from the inner to the outer of the curved wall. The numerical results show that there is a thin transition region between inner and outer wall where the pressure drops dramatically. Over long times, the inner wall is treated as dry, and a fluid rivulet with zero contact angle

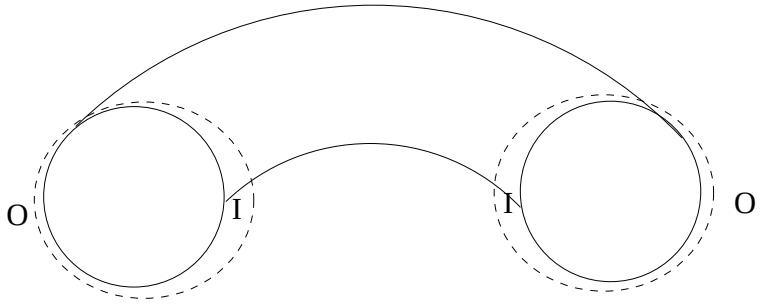



Figure 4.5: Evolution of thin flow on the outside of a torus for later time. $I$ and $O$ denote the inner and outer rim of the torus respectively.

develops at the outer wall, see Figure 4.7. Jensen (1997) examined the stability of this rivulet by applying an axial perturbation. The rivulet may be subject to the Rayleigh instability, causing an axial unduloid to develop if the fluid exceed a critical value. This axial unduloid is itself unstable and can break up into collars depending on the wavelength of the perturbation and the fluid volume.

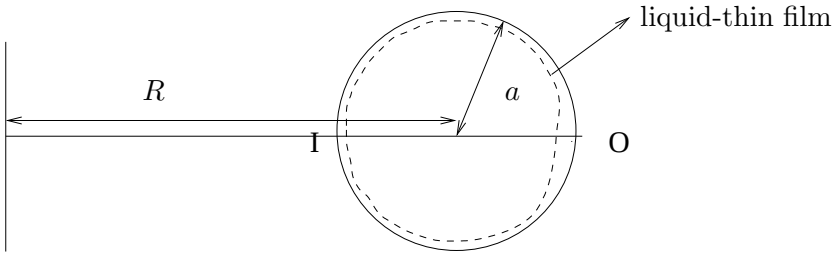



Figure 4.6: Schematic of a thin-liquid film (dashed line) flowing inside the curved tube where I and O denote the inside and outside of the bend respectively. Reproduced from Jensen (1997).

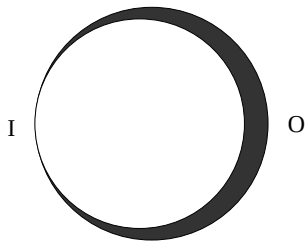



Figure 4.7: Liquid forming a rivulet with zero contact angle. I and O denote the inside and outside of the bend respectively.

## 4.4 Conclusion

We have shown the derivation of the general leading-order equation governing the fluid flow of thin liquid films over a stationary, curved substrate. We have then classified the substrate curvature into three regimes, based on Howell's analysis (Howell, 2003). The other

approach in this area (Roberts & Li, 2006; Roy et al., 2002) include some higher-order corrections causing the smoothness of any singularities developed due to the hyperbolic problem. Consequently, they can be solved easily by numerical simulations.

The centre manifold theory is a new intriguing technique applied in some literatures (Roberts & Li, 2006; Roy et al., 2002). We have also presented thin-film flow behaviours caused by substrate curvature. A torus structure, in particular, a weakly curved cylindrical tube is physiologically relevant to our research. The work done by Jensen (1997) showed that the effect of small curvature on the distribution of fluid lining on the interior of the tube causes slow drainage from the inner to the outer tube wall. The rivulets form over long time period and may break into isolated droplets when the fluid is subject to long-wavelength disturbances.

# Chapter 5

# A two-layer viscous fluids model

Two-layer flows in a confined channel often occur in nature and technology and have attracted many researchers. They play important roles in, for example, internal combustion engines, compound jets, distillation processes and the transportation of oil and gas in pipelines.

In this chapter, we aim to investigate a two-layer immiscible liquid-liquid system. This is motivated by the interaction between blood flow and an atherosclerostic plaque. In our model, we treat both blood and plaque as incompressible Newtonian fluids governed by the Navier-Stokes equations.

Our study in this chapter is organized as follows. In §5.1, a system of coupled evolution equations for two layer flows will be derived in the lubrication approximation, and we then assume the thickness of the lower layer to be much smaller than that of the upper layer, so that a single evolution equation for the thin film thickness is obtained. The applied pressure gradient acted on the fluid-fluid interface is a time-dependent function which resembles blood pressure in cardiovascular system.

In §5.2, the hydrodynamic behaviors of the thin film will be investigated by a linear stability analysis. In §5.3, the numerical simulations for steady and transient flows will be examined. Finally, concluding remarks are given in §5.4.

## 5.1 Two thin-film flows models

### 5.1.1 Introduction to the problem

As illustrated in Figure 5.1. We consider the two-dimensional flow of two immiscible incompressible fluids in the Cartesian coordinates $(x, y)$, the fluids being confined to the channel $0 < y < H$, where $H$ is a constant; the subscripts 1 and 2 on the pressure and velocity variables correspond to the lower and upper fluids respectively, with corresponding constant densities $\rho_i$ and dynamic viscosities $\mu_i$. The flows are governed by the incompressible Navier-Stokes equations. We suppose the usual no-slip and no-flux conditions on the walls. At the fluid-fluid interface $y = h(x, t)$, the continuity of the fluid velocities and the usual stress balance introducing surface tension are assumed. Gravity and additional body forces to the fluids are neglected in this model due to the minor effects in a cardiovascular system.

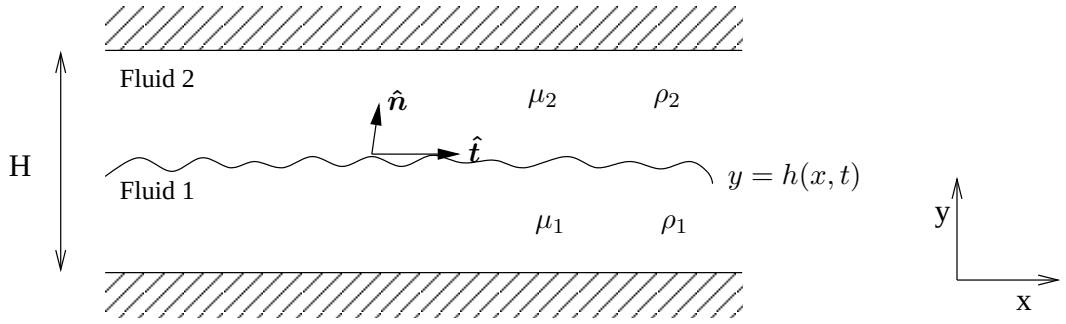



Figure 5.1: Sketch illustrating the two thin-film flows in the channel $0 < y < H$.

### 5.1.2 The governing equations and the boundary conditions

The incompressible Navier-Stokes equations in fluid $i$ (for $i = 1, 2$) are given by

$$\rho_i \left( \frac{\partial \boldsymbol{u}_i}{\partial t} + (\boldsymbol{u}_i \cdot \boldsymbol{\nabla})\boldsymbol{u}_i \right) = -\nabla p_i + \mu_i \boldsymbol{\nabla}^2 \boldsymbol{u}_i, \tag{5.1}$$

$$\boldsymbol{\nabla} \cdot \boldsymbol{u_i} = 0, \tag{5.2}$$

where $\boldsymbol{u}_i(x, y, t)$ is the velocity, $p_i(x, y, t)$ is the pressure, $\rho_i$ is the constant density and $\mu_i$ is the constant viscosity of fluid $i$.

The continuity of velocities at the interface is given by

$$u_1 = u_2, \qquad v_1 = v_2 \qquad \text{on} \qquad y = h(x, t). \tag{5.3}$$

At the interface $y = h(x, t)$, we have the kinematic boundary conditions (for $i = 1, 2$)

$$v_i = h_t + u_i h_x \qquad \text{on} \qquad y = h(x, t), \tag{5.4}$$

where subscripts $x, t$ denote partial differentiation with respect to $x, t$ respectively. We now derive conditions which ensure continuity of stress at the interface. We denote by $\hat{\boldsymbol{n}}$ the unit outward normal and by $\hat{\boldsymbol{t}}$ the unit tangent to the interface in the $x-$direction, *viz.*

$$\hat{\boldsymbol{n}} = \frac{1}{(1 + h_x^2)^{1/2}} \begin{pmatrix} -h_x \\ 1 \end{pmatrix}, \qquad \hat{\boldsymbol{t}} = \frac{1}{(1 + h_x^2)^{1/2}} \begin{pmatrix} 1 \\ h_x \end{pmatrix}. \tag{5.5}$$

The stress tensor in each of the fluids is given by

$$\boldsymbol{T}_i = -p_i \boldsymbol{I} + \mu_i \left( \boldsymbol{\nabla} \boldsymbol{u}_i + (\boldsymbol{\nabla} \boldsymbol{u}_i)^T \right). \tag{5.6}$$

The interfacial stress-balance equation is given by

$$\hat{\boldsymbol{n}} \cdot \boldsymbol{T}_2 - \hat{\boldsymbol{n}} \cdot \boldsymbol{T}_1 = -\sigma \kappa \hat{\boldsymbol{n}}, \tag{5.7}$$

where $\sigma$ is the constant surface tension and $\kappa$ is the curvature of the interface, which is given by

$$\kappa = \frac{h_{xx}}{(1 + h_x^2)^{3/2}}. \tag{5.8}$$

By taking the inner product of (5.7) with $\hat{\boldsymbol{n}}$ and $\hat{\boldsymbol{t}}$, we obtain the normal stress balance

$$\hat{\boldsymbol{n}} \cdot \boldsymbol{T}_2 \cdot \hat{\boldsymbol{n}} - \hat{\boldsymbol{n}} \cdot \boldsymbol{T}_1 \cdot \hat{\boldsymbol{n}} = -\sigma \kappa, \tag{5.9}$$

and the tangential stress balance

$$\hat{\boldsymbol{t}} \cdot \boldsymbol{T}_1 \cdot \hat{\boldsymbol{n}} = \hat{\boldsymbol{t}} \cdot \boldsymbol{T}_2 \cdot \hat{\boldsymbol{n}}. \tag{5.10}$$

Substituting (5.5) and (5.6) into (5.9) and (5.10) and rearranging, we obtain in component form the normal stress boundary condition

$$\begin{aligned} &-(p_1 - p_2) + \frac{2\mu_1}{1+h_x^2}\left(h_x^2\frac{\partial u_1}{\partial x} - h_x\left(\frac{\partial u_1}{\partial y} + \frac{\partial v_1}{\partial x}\right) + \frac{\partial v_1}{\partial y}\right) \\ &- \frac{2\mu_2}{1+h_x^2}\left(h_x^2\frac{\partial u_2}{\partial x} - h_x\left(\frac{\partial u_2}{\partial y} + \frac{\partial v_2}{\partial x}\right) + \frac{\partial v_2}{\partial y}\right) = \frac{\sigma h_{xx}}{(1+h_x^2)^{3/2}}, \end{aligned} \tag{5.11}$$

and the tangential stress boundary condition

$$\begin{aligned} &\frac{\mu_1}{1+h_x^2}\left(2h_x\left(\frac{\partial u_1}{\partial x} - \frac{\partial v_1}{\partial y}\right) + (h_x^2-1)\left(\frac{\partial u_1}{\partial y} + \frac{\partial v_1}{\partial x}\right)\right) \\ &= \frac{\mu_2}{1+h_x^2}\left(2h_x\left(\frac{\partial u_2}{\partial x} - \frac{\partial v_2}{\partial y}\right) + (h_x^2-1)\left(\frac{\partial u_2}{\partial y} + \frac{\partial v_2}{\partial x}\right)\right) \end{aligned} \tag{5.12}$$

both of which apply on the free boundary $y = h(x,t)$.

The no-slip and no-flux boundary conditions are given by

$$u_1 = v_1 = 0 \qquad \text{on} \qquad y = 0, \tag{5.13}$$

and

$$u_2 = v_2 = 0 \qquad \text{on} \qquad y = H. \tag{5.14}$$

### 5.1.3 Nondimensionalisation and scaling

By introducing the typical lengthscale along the film $L$, the vertical lengthscale $\bar{h}$ and the velocity scale $U$, we shall exploit the assumed small aspect ratio $\delta = \bar{h}/L$. Thus the following scalings are introduced:

$$\begin{gathered} x = Lx^*, \qquad y = \bar{h}y^*, \qquad t = \frac{L}{U}t^*, \\ u_i = Uu_i^*, \qquad v_i = \delta U v_i^*, \qquad h = \bar{h}h^*, \qquad p_i = \frac{\mu_2 UL}{\bar{h}^2}p_i^*, \end{gathered}$$

where $i = 1, 2$ and the asterisks denote dimensionless quantities. The dimensionless governing equations are given by (dropping asterisks because all quantities are now nondimensional)

$$\frac{\partial u_1}{\partial x} + \frac{\partial v_1}{\partial y} = 0, \tag{5.15}$$

$$\delta^2 Re\left(\frac{\rho}{\mu}\right)\left(\frac{\partial u_1}{\partial t} + u_1\frac{\partial u_1}{\partial x} + v_1\frac{\partial u_1}{\partial y}\right) = -\frac{1}{\mu}\frac{\partial p_1}{\partial x} + \delta^2\frac{\partial^2 u_1}{\partial x^2} + \frac{\partial^2 u_1}{\partial y^2}, \tag{5.16}$$

$$\delta^4 Re\left(\frac{\rho}{\mu}\right)\left(\frac{\partial v_1}{\partial t} + u_1\frac{\partial v_1}{\partial x} + v_1\frac{\partial v_1}{\partial y}\right) = -\frac{1}{\mu}\frac{\partial p_1}{\partial x} + \delta^4\frac{\partial^2 v_1}{\partial x^2} + \delta^2\frac{\partial^2 v_1}{\partial y^2}, \tag{5.17}$$

in fluid 1, and

$$\frac{\partial u_2}{\partial x} + \frac{\partial v_2}{\partial y} = 0, \tag{5.18}$$

$$\delta^2 Re \left( \frac{\partial u_2}{\partial t} + u_2 \frac{\partial u_2}{\partial x} + v_2 \frac{\partial u_2}{\partial y} \right) = -\frac{\partial p_2}{\partial x} + \delta^2 \frac{\partial^2 u_2}{\partial x^2} + \frac{\partial^2 u_2}{\partial y^2}, \tag{5.19}$$

$$\delta^4 Re \left( \frac{\partial v_2}{\partial t} + u_2 \frac{\partial v_2}{\partial x} + v_2 \frac{\partial v_2}{\partial y} \right) = -\frac{\partial p_2}{\partial y} + \left( \delta^4 \frac{\partial^2 v_2}{\partial x^2} + \delta^2 \frac{\partial^2 v_2}{\partial y^2} \right), \tag{5.20}$$

in fluid 2, where $\mu = \mu_1/\mu_2, \rho = \rho_1/\rho_2$, and the Reynolds number $Re = \rho_2 UL/\mu_2$.

The kinematic and no-slip boundary conditions (5.4), (5.13) and (5.14) become

$$v_i = h_t + u_i h_x, \qquad u_1 = u_2, \qquad v_1 = v_2 \qquad \text{on} \qquad y = h(x,t), \tag{5.21}$$

with

$$u_1 = v_1 = 0 \qquad \text{on} \qquad y = 0, \tag{5.22}$$

and

$$u_2 = v_2 = 0 \qquad \text{on} \qquad y = \hat{H}, \tag{5.23}$$

where $\hat{H} = H/\bar{h}$.

The normal stress condition (5.11) becomes

$$\begin{aligned} &-(p_1 - p_2) + \frac{2\mu}{1+\delta^2 h_x^2} \left( \delta^4 \left( h_x^2 \frac{\partial u_1}{\partial x} - h_x \frac{\partial v_1}{\partial x} \right) - \delta^2 \left( h_x \frac{\partial u_1}{\partial y} - \frac{\partial v_1}{\partial y} \right) \right) \\ &- \frac{2}{1+\delta^2 h_x^2} \left( \delta^4 \left( h_x^2 \frac{\partial u_2}{\partial x} - h_x \frac{\partial v_2}{\partial x} \right) - \delta^2 \left( h_x \frac{\partial u_2}{\partial y} - \frac{\partial v_2}{\partial y} \right) \right) = \frac{C h_{xx}}{(1+\delta^2 h_x^2)^{3/2}}, \end{aligned} \tag{5.24}$$

on $y = h(x,t)$. The dimensionless parameter

$$C = \frac{\delta^3 \sigma}{\mu_2 U} \tag{5.25}$$

is the inverse Capillary number. The tangential stress (5.12) condition becomes

$$\begin{aligned} &\frac{\mu}{1+\delta^2 h_x^2} \left( 2\delta^2 h_x \left( \frac{\partial u_1}{\partial x} - \frac{\partial v_1}{\partial y} \right) + (\delta^2 h_x^2 - 1) \left( \frac{\partial u_1}{\partial y} + \delta^2 \frac{\partial v_1}{\partial x} \right) \right) \\ &= \frac{1}{1+\delta^2 h_x^2} \left( 2\delta^2 h_x \left( \frac{\partial u_2}{\partial x} - \frac{\partial v_2}{\partial y} \right) + (\delta^2 h_x^2 - 1) \left( \frac{\partial u_2}{\partial y} + \delta^2 \frac{\partial v_2}{\partial x} \right) \right) \end{aligned} \tag{5.26}$$

on $y = h(x,t)$.

### 5.1.4 Derivation of averaged equations

For both $\delta \ll 1$ and $\delta^2 Re \ll 1$, we obtain at leading order the quasi-steady lubrication equations

$$\frac{\partial u_1}{\partial x} + \frac{\partial v_1}{\partial y} = 0, \qquad \frac{\partial p_1}{\partial x} = \mu \frac{\partial^2 u_1}{\partial y^2}, \qquad \frac{\partial p_1}{\partial y} = 0, \tag{5.27}$$

in fluid 1, together with

$$\frac{\partial u_2}{\partial x} + \frac{\partial v_2}{\partial y} = 0, \qquad \frac{\partial p_2}{\partial x} = \frac{\partial^2 u_2}{\partial y^2}, \qquad \frac{\partial p_2}{\partial y} = 0, \tag{5.28}$$

in fluid 2. The boundary conditions are given by

$$u_1 = v_1 = 0, \qquad \text{on} \qquad y = 0; \tag{5.29}$$

$$v_i = h_t + u_i h_x, \qquad u_1 = u_2, \qquad v_1 = v_2, \qquad \text{on} \qquad y = h(x,t) \tag{5.30}$$

$$\mu\frac{\partial u_1}{\partial y} = \frac{\partial u_2}{\partial y}, \qquad p_1 - p_2 = -Ch_{xx}, \qquad \text{on} \qquad y = h(x,t). \tag{5.31}$$

$$u_2 = v_2 = 0, \qquad \text{on} \qquad y = \hat{H}. \tag{5.32}$$

The fluid pressures of both layers are independent of y at leading order. Thus, the longtitudinal velocities of fluid 1, $u_1(x,y,t)$ and fluid 2, $u_2(x,y,t)$ are found by integrating (5.27) and (5.28) twice with respect to y, and applying the boundary conditions (5.29) and (5.32), giving

$$\mu u_1 = \frac{y^2}{2}\frac{\partial p_1}{\partial x} + A_1(x,t)y, \tag{5.33}$$

$$u_2 = \frac{\partial p_2}{\partial x}\left(\frac{y^2}{2} - \frac{\hat{H}^2}{2}\right) + A_2(x,t)(y - \hat{H}), \tag{5.34}$$

where $A_1(x,t)$ and $A_2(x,t)$ are to be determined. For convenience, we let

$$\mu\frac{\partial u_1}{\partial y} = \frac{\partial u_2}{\partial y} = \beta(x,t), \tag{5.35}$$

where $\beta(x,t)$ is to be determined, so that

$$A_1(x,t) = \beta(x,t) - h_1\frac{\partial p_1}{\partial x}, \tag{5.36}$$

$$A_2(x,t) = \beta(x,t) - h_1\frac{\partial p_2}{\partial x}.. \tag{5.37}$$

Since $u_1 = u_2$ on $y = h_1(x,t)$, we deduce that $\beta$ is given by

$$\beta = \left(\frac{\mu}{h_1 + \mu h_2}\right)\left[\frac{1}{2}\left(\frac{h_1^2}{\mu}\frac{\partial p_1}{\partial x} - h_2^2\frac{\partial p_2}{\partial x}\right)\right], \tag{5.38}$$

where $h_2 = \hat{H} - h_1$.
We obtain the cross-layer averaged conservation of mass expression for fluid 1 by integrating the continuity equation with respect to y, from 0 to $h_1(x,t)$, and then applying the kinematic condition (5.30), giving

$$\frac{\partial h_1}{\partial t} + \frac{\partial}{\partial x}\left(-\frac{h_1^3}{3\mu}\frac{\partial p_1}{\partial x} + \frac{\beta h_1^2}{2\mu}\right) = 0; \tag{5.39}$$

similarly, for fluid 2 we obtain the expression

$$\frac{\partial h_2}{\partial t} + \frac{\partial}{\partial x}\left(-\frac{h_2^3}{3}\frac{\partial p_2}{\partial x} - \frac{\beta h_2^2}{2}\right) = 0. \tag{5.40}$$

To sum up, for the five unknowns $h_1, h_2, p_1, p_2, \beta$, we have five equations, namely (5.39)-(5.40) together with

$$\beta = \left(\frac{\mu}{h_1 + \mu h_2}\right)\left[\frac{1}{2}\left(\frac{h_1^2}{\mu}\frac{\partial p_1}{\partial x} - h_2^2\frac{\partial p_2}{\partial x}\right)\right], \tag{5.41}$$

$$h_1 + h_2 = \hat{H}, \tag{5.42}$$

$$p_1 - p_2 = -C\frac{\partial^2 h_1}{\partial x^2}. \tag{5.43}$$

The thickness of the liquid layers evolve according to their own pressure gradients and the pressure difference at the interface between them. We note that the system (5.39)-(5.40) is unchanged upon swapping the subscripts 1 and 2, and replacing $\mu$ with $1/\mu$, as required.

### 5.1.5 The evolution equation governing the fluid behaviours at the interface

We consider the sublimit in which the lower layer is much thinner than the upper layer by writing $h_1 = \epsilon h, h_2 = \hat{H} - \epsilon h$, where $\epsilon \ll 1$. Substituting these expressions into (5.39) - (5.43), the thin film equation in the lower layer becomes

$$0 = \frac{\partial h}{\partial t} + \frac{\partial}{\partial x}\left(-\frac{\epsilon^2 h^3}{3\mu}\frac{\partial p_1}{\partial x} - \frac{\epsilon\beta h^2}{2\mu}\right), \tag{5.44}$$

while that in the upper layer becomes

$$0 = -\epsilon\frac{\partial h}{\partial t} + \frac{\partial}{\partial x}\left(-\frac{(\hat{H}-\epsilon h)^3}{3}\frac{\partial p_2}{\partial x} - \frac{\beta(\hat{H}-\epsilon h)^2}{2}\right), \tag{5.45}$$

where the shear stress of the free boundary

$$\begin{aligned}\beta &= \left(\frac{\mu}{\epsilon h + \mu(\hat{H}-\epsilon h)}\right)\left[\frac{1}{2}\left(\frac{\epsilon^2 h^2}{\mu}\frac{\partial p_1}{\partial x} - (\hat{H}-\epsilon h)^2\frac{\partial p_2}{\partial x}\right)\right], \\ &= -\frac{\hat{H}}{2}\frac{\partial p_2}{\partial x} + O(\epsilon),\end{aligned} \tag{5.46}$$

as $\epsilon \to 0$. Substituting (5.46) into (5.45) gives (correct up to O($\epsilon$))

$$0 = -\epsilon\frac{\partial h}{\partial t} + \frac{\partial}{\partial x}\left[-\frac{(\hat{H}-\epsilon h)^3}{3}\frac{\partial p_2}{\partial x} - \left(-\frac{\hat{H}}{2}\frac{\partial p_2}{\partial x}\right)\frac{(\hat{H}-\epsilon h)^2}{2}\right]. \tag{5.47}$$

We consider the leading order version of (5.47), which implies that

$$\frac{\partial p_2}{\partial x} = A(t), \tag{5.48}$$

where $A(t)$ is an arbitrary function of $t$. Now as $p_1 = p_2 - \epsilon C h_{xx}$, we substitute this into (5.44) to obtain

$$0 = \frac{\partial h}{\partial t} + \frac{\partial}{\partial x}\left(-A(t)\frac{\epsilon^2 h^3}{3\mu} + \frac{\epsilon^3 C h_{xxx} h^3}{3\mu} + A(t)\frac{\epsilon H h^2}{4\mu}\right). \tag{5.49}$$

In order to balancing all of the terms on the right-hand side. We must assume that

$$\frac{\epsilon^3 C}{\mu} = O(1), \qquad \frac{\epsilon A(t)}{\mu} = O(1), \tag{5.50}$$

as $\epsilon \to 0$. Thus, at the leading order, the thin-film equation governing the lower layer is given by

$$0 = \frac{\partial h}{\partial t} + \frac{\partial}{\partial x}\left(\frac{\Gamma}{3}h^3 h_{xxx} + \frac{M}{4}h^2\right), \tag{5.51}$$

where

$$\Gamma = \frac{C\epsilon^3}{\mu} = O(1), \qquad M = \frac{\epsilon \hat{H} A(t)}{\mu} = O(1). \tag{5.52}$$

The thin film equation given in (5.51) is governed by the Capillary effect and the pressure variation from the upper fluid.

Note that when the surface tension force term is negligible ($\Gamma = 0$), (5.51) reduces to

$$h_t + \frac{\partial}{\partial x}\left(\frac{Mh^2}{4}\right) = 0. \tag{5.53}$$

Let $t = 2T/M$, where $M$ is a constant, so (5.53) becomes the inviscid Burgers' equation which is in the form of a nonlinear first order partial differential equation

$$\frac{\partial h}{\partial T} + \frac{\partial}{\partial x}\left(\frac{h^2}{2}\right) = 0, \qquad -\infty < x < \infty \tag{5.54}$$

or equivalently $h_T + hh_x = 0$ with the initial data $h(x, 0) = f(x_0)$. The problem can be solved by the method of characteristics in which the characteristics are given by $x'(T) = h(x, T)$, where $'$ indicates the ordinary derivative. As $h(x, t) = f(x_0)$ is constant along each characteristic curve, so

$$x(t) = f(x_0)t + x_0. \tag{5.55}$$

So the characteristics are straight lines with slope $f(x_0)$, and it leads to the solution of the initial value problem $h(x, t) = f(x - ht)$. As the slope of the characteristics are not all the same, dependent on the initial data. So it is possible for the characteristics to intersect. This problem fails to have a classical solution as the coalescence of characteristics generatess a multivalued solution. Thus, a shock must be introduced to recover a physically relevant single-valued solution ( as described in Smoller (1994) ).

In the case when $\Gamma \ll 1$, we expect shock-type solutions for certain initial data in which rapid changes in $h$ are smoothed out by surface tension over narrow regions (Leveque, 2002). In §5.2, we will investigate the stability of the fluid-fluid interface equation (5.51).

## 5.2 Linear stability analysis

Physiologically speaking, the shear stress term in (5.51) comes from the effect a blood pressure gradient in cardiac cycle corresponding to the systolic and diastolic states. It is a periodic oscillation, so we can define $M(t) = B\sin(\alpha t)$, where $B$ is the amplitude of the oscillation giving rise to systolic and diastolic pressure and $\alpha = 2\pi f$, where $f$ is the pulse frequency. The initial (short time) evolution of the film profile is explained by a linearized equation when the disturbance amplitude is much smaller than the mean film thickness, see Figure 5.2. A typical form of the perturbed film thickness is written as

$$h = H_0 + H_1 \exp(\omega t + ikx), \tag{5.56}$$

where $H_0$ is an equilibrium solution, $Re(\omega)$ is the disturbance growth rate, $|H_1| \ll |H_0|$ is the amplitude of the disturbance and $k$ is the wave number; the imaginary part of $\omega$ corresponds to translation of the flow along the $x$ axis (corresponding to travelling wave solutions).

By plugging (5.56) into (5.51), we obtain the dispersion equation $\omega = -\Gamma {H_0}^3 k^4/3 + ikM(t)H_0/2$ which is implying that a uniform film profile is always stable. If we were to include gravity, in the case where the heavier fluid sits above the lighter fluid, the interface is unstable.

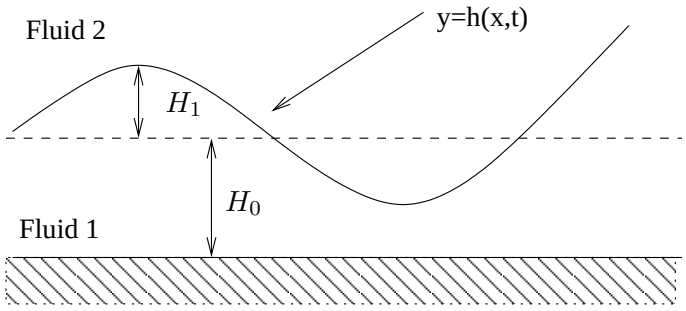



Figure 5.2: Schematic presentation of disturbance applied at the liquid-liquid interface.

## 5.3 Numerical schemes

Linear stability analysis is inadequate to capture all aspects of thin film dynamics. Therefore, the numerical simulation will be performed in the next section. Equation (5.51) is a fourth-order nonlinear diffusion equation, so it requires to impose the initial condition and 4 boundary conditions. We take our physical domain to be $x \in [a, b]$ and assume no flux and a pinned free surface at the boundaries, *viz*

$$h(a,t) = 1, \qquad q(a,t) = 0 \tag{5.57}$$

$$h(b,t) = 1, \qquad q(b,t) = 0, \tag{5.58}$$

where the flux $q = \Gamma h^3 h_{xxx}/3 + Mh^2/4$. In §5.3.1, the numerical scheme for (5.51) is shown. In §5.3.2, we then investigate the steady-state solutions in order to justify the consistency with the numerical results for the full time-dependent nonlinear equation (5.51).

### 5.3.1 Transient solutions

In this section, the numerical simulation of the evolution of the thin-film thickness $h(x,t)$ given by (5.51) will be presented. The method of lines is used. We first discretize the domain along the spatial variable $x$ into a system of nonlinear fourth-order ODEs. We denote by $H_i(t)$ the numerical approximation to the exact value $h_i(t)$.

The domain is subdivided into $N+1$ equally spaced mesh points, $x_0, x_1, ..., x_{N+1}$, where $x_i = a+(i-1/2)\triangle x$ for $i = 0, 1, ..., N, N+1$. We define the half-grid point $x_{i+1/2} = a+i\triangle x$ for $i = 0, 1, ..., N$, where $x_{1/2} = a$ and $x_{N+1/2} = b$, as shown in Figure 5.3. The flux $Q_{i+1/2}(t)$ is evaluated at the half-node $x_{i+1/2}$. The scheme can be written as

$$\frac{\mathrm{d}H_i}{\mathrm{d}t} = -\frac{Q_{i+\frac{1}{2}} - Q_{i-\frac{1}{2}}}{\triangle x}. \tag{5.59}$$

To find an expression for $Q_{i+1/2}$, we use finite difference methods to define

$$H_{\bar{x},i} = \frac{H_i - H_{i-1}}{\triangle x}, \tag{5.60}$$

$$H_{\bar{x}x,i} = \frac{H_{\bar{x},i+1} - H_{\bar{x},i}}{\triangle x}, \tag{5.61}$$

$$H_{\bar{x}x\bar{x},i} = \frac{H_{\bar{x}x,i} - H_{\bar{x}x,i-1}}{\triangle x}, \tag{5.62}$$

where a subscript $\bar{x}$ denotes a backward difference and a subscribt $x$ denotes a forward difference.

When $M$ in (5.51) is negligible, the fourth-order diffusion equation is degenerate since the diffusivity vanishes as $h \to 0$. One remarkable of this nonlinear equation is that even for the positivity of solutions is justified analytically, however, computations may still lead to false singularities (Zhornitskaya & Bertozzi, 2000). Standard finite difference schemes do not necessarily preserve the positivity of solutions. Thus, several schemes have been developed to resolve this problem. In this section, we use the method suggested by Zhornitskaya & Bertozzi (2000). The scheme is based on the idea of Lyapunov dissipation. To obtain a numerical approximation for $h^3$, Zhornitskaya & Bertozzi (2000) use the interpolation which is written as

$$H^3_{i+1/2} = \begin{cases} \frac{H_{i+1}-H_i}{G'(H_{i+1})-G'(H_i)} & \text{if } H_{i+1} \neq H_i \\ H_i^3 & \text{if } H_{i+1} = H_i \end{cases} \tag{5.63}$$

where $G(H_i)$ is a function satisfying $G''(H_i) = 1/{H_i}^3$. Thus, the discretization of the flux term is given by

$$Q_{i+\frac{1}{2}} = \frac{\Gamma}{3(\triangle x)^3}\left(\frac{2H_i^2 H_{i+1}^2}{H_i + H_{i+1}}\right)(H_{i+2} - 3H_{i+1} + 3H_i - H_{i-1}) + \frac{M(t)}{4}(H_{i+1}^2 + H_i^2). \tag{5.64}$$

For $M = 0$, using a central difference for the term proportional to $(h^2)_x$ in (5.51), the interpolation (5.63) leads to a scheme which is positivity preserving *i.e.*, the solution which is strictly positive for $t = 0$ retains this property for all $t > 0$.

To discretize the boundary conditions, we introduce two ghost points $x_0$ and $x_{N+1}$. The boundary conditions are evaluated at $x_{1/2}$ corresponding to $x = a$, and $x_{N+1/2}$ corresponding to $x = b$. Figure 5.3 shows our numerical scheme with one ghost point at each boundary.

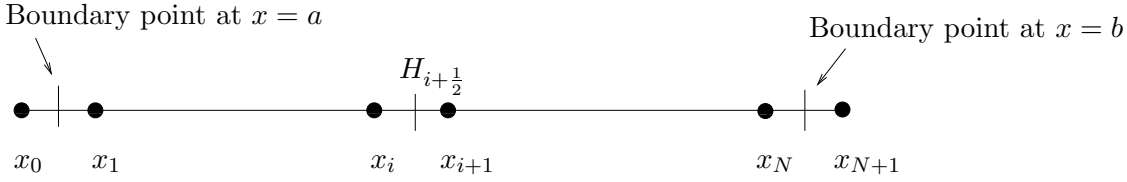



Figure 5.3: Diagram showing the finite-diffence scheme of the film evolution equations

The discretized boundary condition at $x = a$ becomes

$$1 = h(a,t) = \frac{h_0 + h_1}{2} + O(\triangle x) \qquad \text{as} \qquad \triangle x \to 0, \tag{5.65}$$

so $h_0 = 2 - h_1$. Similarly, $h(b,t) = 1$ requires $h_N = 2 - h_{N+1}$.

Now we have a system of $N+2$ coupled equations ($N$ equations from the interior points and 2 equations from boundary conditions). Once the discretization is complete, the next step is to solve the system of ODEs by using a built-in MATLAB solver. MATLAB has a number of built-in ODE solving routines. We choose ode15s, which is a solver for stiff problems and is based on the numerical differentiation formulas (NDFs). The code is shown in Appendix A and the default relative tolerance value is chosen to be accurate to within 0.0001%

When $\Gamma = 0$, (5.51) reduces to the inviscid Burgers equation (5.54), an equation known to produce shocks and hence steep gradients incompatible with the slow variation assumption. We introduce the Lax-Wendroff scheme which is used to solve hyperbolic partial differential equations (Tannehill et al., 1997).

In order to derive this finite difference scheme, a new grid definition must be introduced

$$x_i = a + i\triangle x, \qquad i = 0, 1, ..., N, \qquad \triangle x = \frac{b-a}{N}, \tag{5.66}$$

$$t^k = k\triangle t, \qquad k = 0, 1, ... \tag{5.67}$$

where the stability condition is given by $|\triangle t u_{\max}| \ll \triangle x$ (Tannehill et al., 1997). We have

$$H_i^{k+1} = H_i^k - \frac{\triangle t}{\triangle x}\frac{F_{i+1}^k - F_{i-1}^k}{2} \tag{5.68}$$

$$+\frac{1}{2}\left(\frac{\triangle t}{\triangle x}\right)^2 A_{i+1/2}^k (F_{i+1}^k - F_i^k) - A_{i-1/2}^k (F_i^k - F_{i-1}^k), \tag{5.69}$$

where $F = 0.5u^2$ and

$$A_{i+1/2}^k = \frac{H_{i+1}^k + H_i^k}{2}, \qquad A_{i-1/2}^k = \frac{H_{i-1}^k + H_i^k}{2}. \tag{5.70}$$

Here, we impose only one-end boundary condition, $h(a,t) = 1$. The code is presented in Appendix B.

### 5.3.2 Steady state solutions

The steady-state solution is obtained by neglecting the time-derivative term in (5.51). So (5.51) becomes

$$\frac{\partial}{\partial x}\left(\frac{\Gamma}{3}h^3 h_{xxx} + \frac{M}{4}h^2\right) = 0. \tag{5.71}$$

We then integrate (5.71) with respect to $x$, and the constant of integration on the right-hand side must be set to zero since there is no flux of fluid at the end points. Thus

$$\frac{\Gamma}{3}h^3 h_{xxx} + \frac{M}{4}h^2 = 0. \tag{5.72}$$

We need three boundary conditions in order to solve (5.72). We have $h(a,t) = 1$ and $h(b,t) = 1$. The other boundary condition is derived from the mass conservation law in which the total mass

$$\int_a^b h\, dx = m \qquad \text{where} \qquad m = \text{constant}, \tag{5.73}$$

is conserved. To solve (5.71) subject to the boundary conditions, we let $h = f_x$, where $f$ is a continuous arbitrary function. So (5.71) can be written as

$$\frac{\Gamma}{3}f_x f_{xxxx} + \frac{M}{4} = 0, \tag{5.74}$$

subject to $f_x(a) = 1, f_x(b) = 1$ and $f(b) - f(a) = m$. We set $f(a) = 0$ and $f(b) = m$. We will solve (5.72) with above boundary conditions by using a solver for boundary value problems (bvp4c) available in MATLAB. The bvp4c solver uses a collocation method for the solution of BVPs. The code is shown in Appendix C.

Note that when $M = 0$ in (5.72), the fluid-fluid interface profile must be in the form $h = 1 + A(x-a)(b-x)$, where $A$ can be found by using (5.73). In the case when $\Gamma = 0$, no solution exists with given boundary conditions.

### 5.3.3 Numerical results

The numerical results to the system described above are presented with varying parameters and time. In order to characterize the dynamics of the fluid-fluid interface, the flow response to shear forcing ( $M$ in (5.51)) will be examined first. Such forcing is provided in the simulations by prescribing sinusoidal disturbances at frequency $\alpha$, with an amplitude $B$ i.e. $M = B\sin(\alpha t)$.

The amplitude of the disturbances, $B$, affects the film distortion and steepening. The results for $B = 0, 1$ and 10 with the fixed values $\alpha = \pi$, $\Gamma = 1$ and the initial condition $h(x, 0) = 1 + 0.1\sin(\pi x)$ in the domain $x \in [0, 1]$ are presented. As can be seen in Figure 5.4, the steady state is reached simultaneously in the absence of shear effects and the fluid-fluid interface oscillates periodically with time and deforms slightly from the initial state for small values of $B$. As $B$ increases, more severe interface-profile distortion occurs.

When $B$ becomes significantly large, our code fails to converge at a critical time. The reasons are unclear. It might be because our numerical scheme is not efficient enough, or there exists singularities on the domain, or both. However, in the case of the inefficiency of the numerical scheme, the most likely reason is due to the discretization of the $(h^2)_x$ term in (5.51). Note that our numerical scheme conserves mass so there is no mass loss in the simulations.

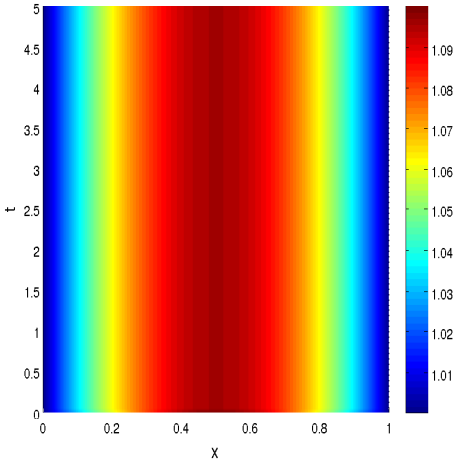
We attempted to solve such difficulties by applying the larger tolerance, but the problem still remains. We then turn our interest to the smoothing effect of surface tension by increasing the values of $\Gamma$. Several simulations have been performed by varying $\Gamma$. It is found that surface tension can have qualitatively and quantitatively significant effects on the flow as the fluid-fluid interface becomes less deformed and our code takes longer time to fail. A representative example is given in Figure 5.5 for $M(t) = 100\sin(\pi t)$ with the fixed initial condition $h(x, 0) = 1 + 0.1\sin(\pi x)$. The program stops running at $t = 0.24$ for $\Gamma = 1$ in which the interface approaches $h \approx 0.65$. In the case for $\Gamma = 5$, the program continues to run until $t = 3.07$.

The same qualitative behaviour is found on decreasing the frequency. During periods of cycle, the shear forcing with lower frequencies takes longer time to reach its maximum value than that with higher frequencies. The effect of the oscillation frequency is illustrated in Figure 5.6. At time $t = 1$, the fluctuation of the interface from its initial position is smaller for $\alpha = \pi/20$ than for $\alpha = \pi/5$.

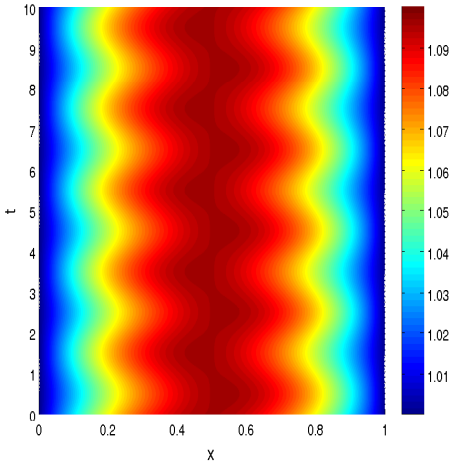
In order to proceed further with the possibility of interfacial breakup, we may need to enhance the transient results by investigating the steady state solutions. We examine different values of parameters and it is found that, in all cases, these transient solutions evolve to correspond exactly with their steady-state counterparts. As shown in Figure 5.7, when the constant mass $m = 1.065$, $\Gamma = 1$, $M = 10$ and the initial condition $h(x, 0) = 1 + 0.01\sin(\pi x)$ are held fixed, the interface profiles reach steady state at later times.

The effect of $M$ for steady state solutions are illustrated in Figure 5.8. This is in qualitative agreement with results for transient solutions in which large $M$ causes more distortion from the initial state.

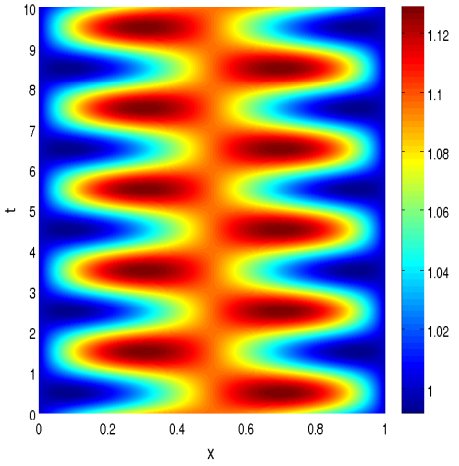
In the case when the fluid-fluid interface is primarily affected by large shear (large $M$), the steady state reaches the interfacial profile as shown in Figure 5.9. The negative value of interfacial height is found on some parts of the domain. It suggests that large shear forcing induced by the upper flow competes with the interfacial tension causes a severe interface deformation and eventually the rupture of the interface profile may occur. This is contrast to the linear stability analysis in which (5.51) is proven to be stable thoroughly. It




(a)

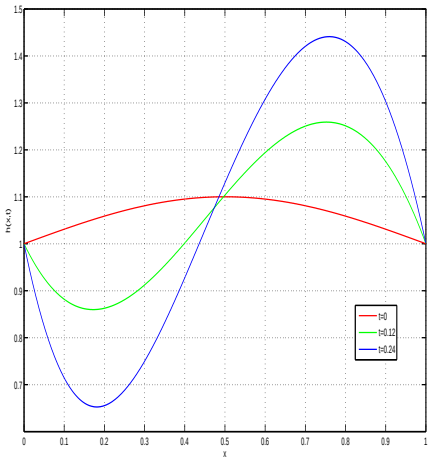



(b)

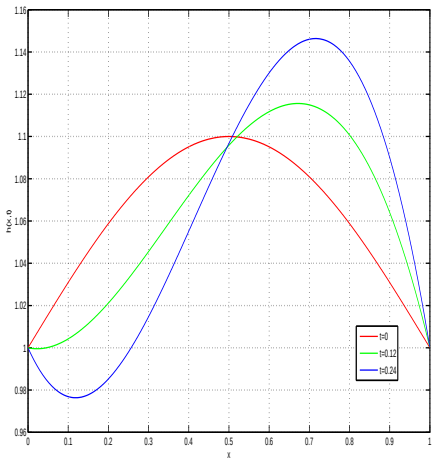



(b)

Figure 5.4: The effects of the oscillation speed when the forcing is $M(t) = B\sin(\pi t)$, where (a) $B = 1$ (b) $B = 10$, where $\Gamma = 1$ and $h(x, 0) = 1 + 0.1\sin(\pi x)$ are held fixed. The colour strip denotes the interfacial height. The colour strip represents the height of the fluid-fluid interface.

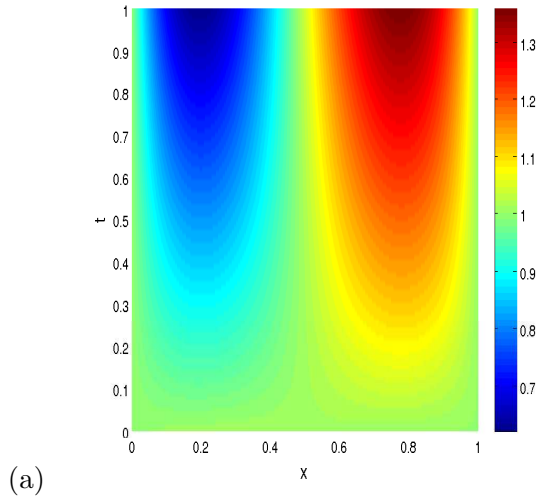



(a)

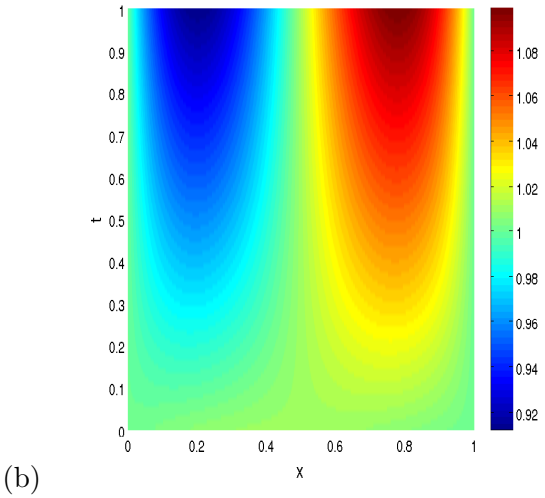



(b)

Figure 5.5: The fluid-fluid interface profile when the oscillatory forcing is $M(t) = 100\sin(\pi t)$ at $t = 0$ , 0.12, 0.24, where (a) $\Gamma = 1$, (b) $\Gamma = 5$.




(a)




(b)

Figure 5.6: The fluid-fluid interface when the oscillatory forcing is (a) $M(t) = 100\sin(\pi t/5)$, and (b) $M(t) = 100\sin(\pi t/20)$ $\Gamma = 1$ and $h(x,0) = 1 + 0.01\sin(\pi x)$. The colour strip represents the height of the fluid-fluid interface.

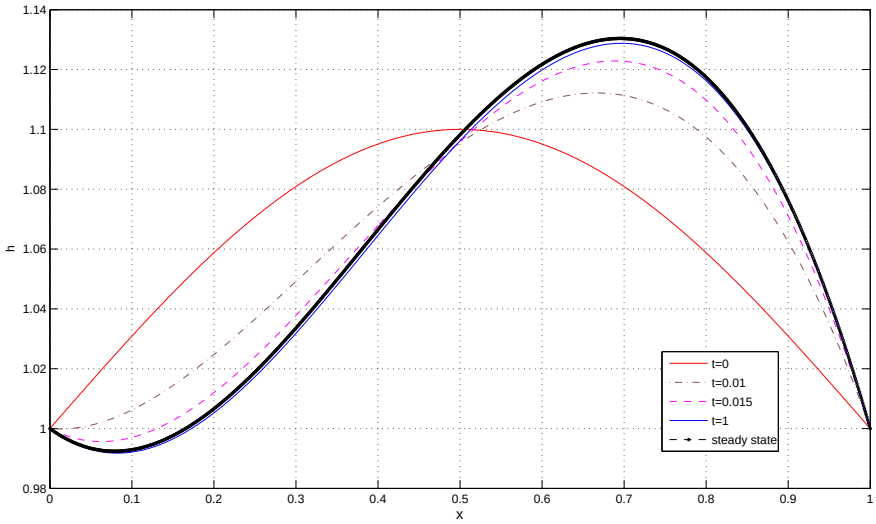



Figure 5.7: The interfacial profile, the progression of the transient solution towards the solution of the steady-state equation when $\Gamma = 1$ with $M = 10$ and the initial condition $h(x, 0) = 1 + 0.1\sin(\pi x)$.

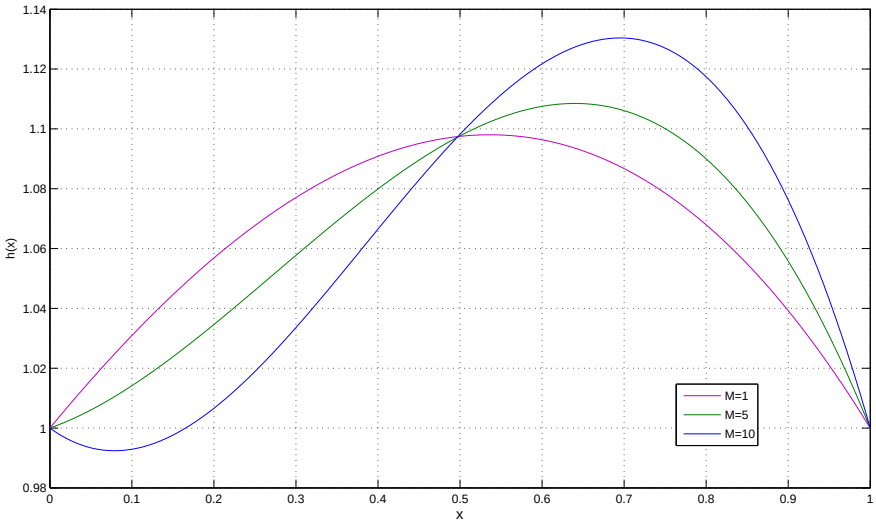



Figure 5.8: Steady-state solutions for a film under the surface tension $\Gamma = 1$ and different values of shear stress forcing $M$, with $m = 1.065$ and $h(x, 0) = 1 + 0.1\sin(\pi x)$.

is understandable since steady state investigates the long-time behaviours. After transient effects have died out, the large shear forcing maintains to implement the perturbed interfial profile.

Physically speaking, the high shear forces associated with the pressure gradient from the upper fluid layer are likely to damage the plaque stability and increase the possibility of a rupture.

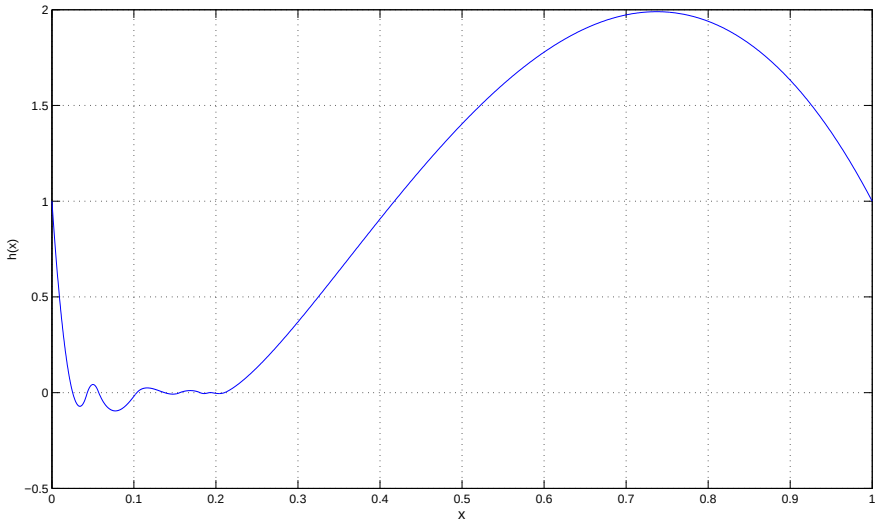



Figure 5.9: Steady-state solutions for a film under the surface tension $\Gamma = 1$, $M = 120$ with $m = 1.065$ and $h(x, 0) = 1 + 0.1\sin(\pi x)$.

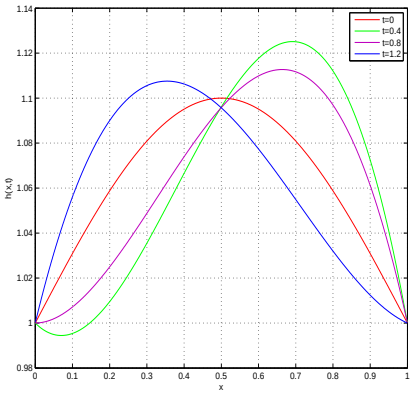
The behaviours of the interface can also depend markedly on the initial condition. Here, we examine the dynamics of the interface when the amplitude of the interface at the initial time is either small or large. As shown in Figure 5.10, when the fluid-fluid interface has a large amplitude at the start, the interface resists the effects of the oscillatory shear forcing and it results in a nearly stationary interface profile. In contrast, when the amplitude of the interface is initially small, the pressure gradient becomes dominant.

Lastly, when $\Gamma = 0$ for transient solutions, it has been shown in §5.1.6 that the dynamics is controlled by a Burgers-type equation. It is well known that solutions of inviscid Burger's equation develop discontinuities downstream after a finite amount of time even if the initial data is smooth. Figure 5.11 shows that the induced oscillations occur and the wave growth in the downstream is accompanied by pronounced steepening of the wave front with time, leading eventually to shock formation.

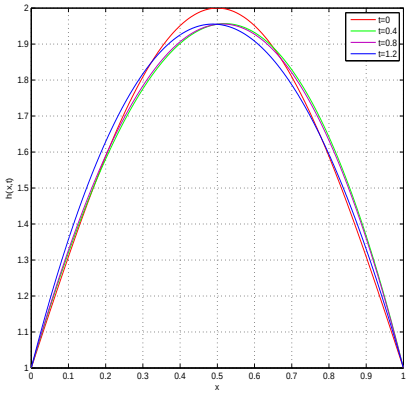
## 5.4 Conclusion

The bilayer immiscible fluid flows in a confined channel are modelled in this Chapter. The nonlinear evolution system are derived in §5.1.4. When $\mu_1 \ll \mu_2$, it is found that the fluid-fluid interface behaviours are determined by capillary effects only. In the physiological point of view, when the plaque becomes solid-like, the shear forcing influenced by blood flow has no effects on the plaque instability, resulting in the stability of plaque for all time. The lower liquid layer is then assumed to be much thinner than the upper liquid layer, and the nonlinear equation system in §5.1.4 is reduced to the evolution equation governing the fluid-fluid interface. Linear stability analysis shows that the interfacial profile is always stable due to capillary effects.

Numerical simulations are conducted under the effects of periodically oscillating shear forcing and surface tension. One remark from the numerical results for transient solutions is when the amplitude of the shear forcing induced by the upper flow becomes so large, our




(a)




(b)

Figure 5.10: The effect of the initial condition $h_0 = 1 + a\sin(\pi t)$ when (a) $a = 0.1$ (b) $a = 1$ at time $t = 0$ (red line), $3\pi/10$ (yellow line), $3\pi/5$ (green line), $\pi$ (blue line). $\Gamma = 1$ and $M(t) = 10\sin(\pi t)$.

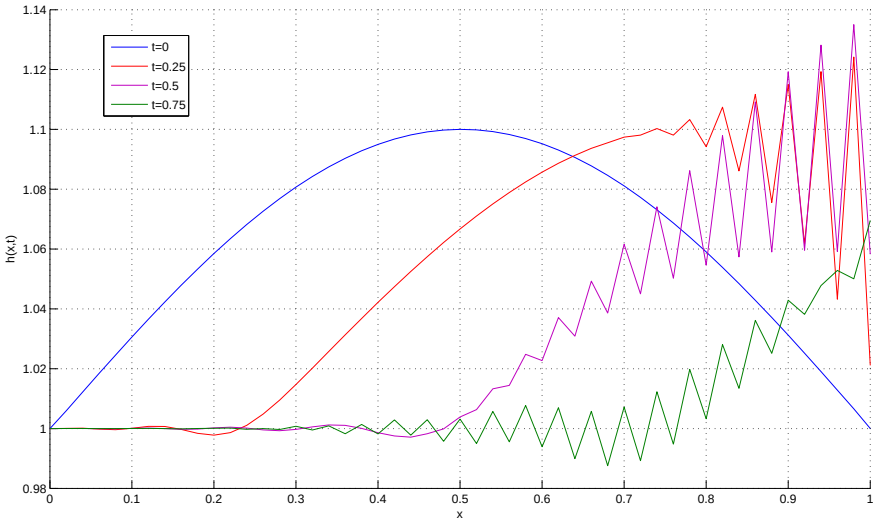



Figure 5.11: The burgers equation.

code fails to converge. Steady-state solutions show that the interfacial-profile rupture is possible. To delay the rupture time, either large surface tension or low frequencies of shear forcing can be imposed. In case of absence of surface tension, the shock may be formed.

# Chapter 6

# Conclusions and Future work

In this final chapter, we will briefly summarise and discuss the work we have done and some suggestions for possible further work will be presented.

## 6.1 Summary and discussion

As discussed in §1.5, various work that elucidates many of the pathways to help us understanding the underlying mechanisms in order to achieve our aimed model, the behaviour of blood flow in the vicinity of atherosclerotic plaque, are presented in Chapter 1-4 .

The formation of an atherosclerotic lesion is a direct biological response, as discussed in Chapter 1. Pathological examination of arteries reveals that the wall shear stresses, both circumferential and axial, are found to be an important factor in determining the region of the occurrence of atherosclerotic plaques which are likely to prevail at sites where the vessel is curved; bifurcates, or sudden change in flow geometry. Early plaques occur principally in regions of flow separation, low wall shear stress, and departure from unidirectional flow. Since the physiological features of real blood vessels are really complex, this leads to very complicated flow patterns. We therefore start by presenting work done on flows in curved tubes in Chapter 2.

The research in this field can be generally classified into three categories: theoretical studies, numerical computations and experimental studies. The analytical techniques that are usually used to solve the problems are the asymptotic methods, which are only possible when the parameters are small, as presented in §2.2 and §2.4. Flow visualizations can be conducted in numerical investigations to give both quantitative and qualitative descriptions of flow phenomena. Laboratory experiments to predict the flow behaviours in curved tubes are typically costly, time-consuming, and sometimes very difficult to carry out. Nevertheless, their results are fundamental to calibrate and validate both analytical and numerical findings.

As discussed in §2.1, the effect of the tube curvature generates a centrifugal force which induces a secondary flow, a pair of counter-rotating vortices in the tube cross-section. Under the steady conditions, this centrifugal force causes the peak axial velocity to increase and to be displaced away from the centre of curvature for large D, where D is the Dean number that is used to characterize the steady component of the axial pressure gradient. Typically, the limitation of low curvature ratio, $\delta \gg 1$ where $\delta = a/R$ and $a$ is the radius of the constant circular cross section and $R$ is the radius of curvature of the planar centerline, has been applied to most work in the field. In reality, the curvature ratio of arteries can not

generally be taken as low enough to neglect. It is found that incorporating finite curvature in stead of a weakly curvature, the qualitative features of the flow do not change, but the quantitative features, in particular the distribution of wall shear stress, are significantly altered for a steady case (Siggers & Waters, 2005).

The flow is more complicated for the pulsatile case than for the steady flows. The appearence of a new vortex pair over and above those in the steady case for oscillatory flow (zero mean) is first demonstrated by Lyne (1971). Nevertheless, pulsatile flows (nonzero mean) are the flow type in a cardiovascular system. They create a dynamic environment that raises many interesting and fundamental fluid questions. Answer to these questions can be used to predict many physiological applications, particularly of our interest, blood flows at sites of intimal thickening in arteries.

The most relevant work done so far is by Siggers & Waters (2008) who studied the unsteady flows with a finite curvature. In contrast to steady flow conditions, pulsatile flow generates a cyclically varying region, and a change in magnitudes and directions depends markedly on the range of parameters. A change in curvature, dependent on the relative importance of its steady- and oscillatory- components, results in a variation in wall shear stress over a cardiac cycle. The multiple solutions for a fixed collection of parameters are usually presented for pulsatile flows because general cases for any range of parameters are far too complex to investigate.

The numerical investigations remain crucial for the research in this field due to the asymmetric nature of solutions, especially for the pulsatile cases where a transition from subcritical to supercritical flows, or from the laminar to the turbulent flows in bifurcation studies are significantly dependent on the numerical simulation.

Chapter 3 is a review of work on thin film flows. Our aim is to highlight the substantial amount of literature dealing with models and analytic work related to our overarching model. We started with the derivation of the general evolution equation for thin film thickness. The stability of a thin film of liquid sheared by a gas at a core of an annular tube is described in §3.2. The well known Hammond equation suggests that the length of an annular thin film is the primary mechanical effect responsible for the thin film instability, reflecting mechanisms of energy transfer from the initial flow to the disturbed flow. The instability effect turns out to be more pronounced for a tube with a long length and the evolution of the thin film can be described by the theory of collars and lobes. Several features including the sliding and collision of lobes and collars arise because energy required to sustain collars and lobes to be stationary in the case of a short tube is released by a transfer of fluid from the thin film region between the adjacent collars. For thick films, nonlinearity effects in the relationship between film thickness and surface curvature are significant. The Capillary instability causes an occluding liquid bridge and the pressure exerted by the fluid on the tube wall is most compressive in the region where the liquid bridge being formed. Wall elasticity facilitates the formation of liquid bridge through the compliant collapse mechanism.

A great deal of work on the spreading of a surfactant-laden liquid drop is primarily motivated by a desire to achieve a fundamental understanding of the spreading process related to surfactant replacement therapy of prematurely born babies who suffer from respiratory distress syndrome (RDS) (Halpern & Grotberg, 1992a; Gaver & Grotberg, 1990; Borgas & Grotberg, 1988). As the surfactant drop spreads, the adsorbed surfactant molecules are subsequently redistributed along the air/liquid interface by convection and diffusion processes, leading to a non-uniform concentration distribution of surfactant along the interface. Convection leads to the surface deformation with a decrease in the local layer thickness right

under the surfactant drop, whereas diffusion attempts to restore the equilibrium surface concentration. The surfactant concentration and the film thickness, as well as the speed and uniformity of film coverage, are important factors that influence these two processes.

The contact line problem, which is still not understood at a basic physical level, is then discussed briefly in §3.4. Standard models introduce the slip condition which is also mathematically equivalent to assuming a precursor film preceding the main drop. Both models avoid singularities at the contact line by introducing adhoc parameters into the system. These parameters influence the main drop and also the characteristics of front instabilities.

The leading-order evolution equations governing thin-film flows over a stationary curved substrate are derived in Chapter 4, using a curvilinear coordinate system. The resulting thin-film evolution equations were considered in three possible distinguished limits, corresponding to the size of the substrate curvature (Howell, 2003). In the case for large substrate curvature, the governing equation is hyperbolic, resulting in the possibilities of singularities but we do not pursue the study in this thesis.

In §4.2, we review the methods used by authors to derive such flows as well as the examples of thin film flows on curved substrates. One example of our interest is flow on a torus, in particular work done by Jensen (1997) who investigated draining flows of liquid thin film lining inside a weakly curved tube. The formation of liquid structures are found on the tube's outer wall due to the higher pressure over there.

In Chapter 5, we develop a model of two-layer viscous fluids in a rigid channel. The nonlinear system governing the flow (5.39)-(5.43) is derived. In the case when the viscosity of the lower-layer fluid is much greater than that of the upper-layer fluid, the equation governing the interface profile is reduced to the one-layer thin film type equation. In §5.1.5, the equation of the fluid-fluid interface is derived when the lower fluid layer is assumed to be extremely thin. Linear stability analysis reveals that the interfacial disturbance is unaffected by shear, and the interfacial flow is always stable due to the Capillary effect. In §5.3, a numerical scheme is presented. The interface continuously moves in the direction of imposed shear and its height oscillates periodically with time. It is found numerically that large shear may cause the fluid-fluid interface rupture. In the absence of Capillary forces, the Burgers-type equation is obtained and it shows that the shock may be formed along the fluid-fluid interface. The problem can be relieved by either increasing surface tension or decreasing the frequency of shear forcing.

To sum up, the mechanisms involved in flows in the neighborhood of plaque are complex and difficult to study *in vivo*. In order to truly model such processes, a series of mathematical models is required. As we emphasized that the wall shear stresses are a key biological factor in provoking plaque, the study of the distributions of wall shear stress along curved tubes is of our particular interest. In addition, plaque is treated as a thin film. The work done by Jensen (1997) shows that fluid in a liquid lining in weakly curved tube redistributes along the circumference to form a thicker layer on the outside wall where the development of atherosclerosis lesion and intimal thickening are usually observed. There is nevertheless one remark here. This liquid drainage is caused by pressure gradients over vessel cross-section, whereas wall shear stresses reviewed in Chapter 2 are functions of the curvature ratio, the steady- and oscillatory-components of axial pressure gradients along the centerline. Therefore, apart from the pressure gradients over the vessel cross-section, there are many features must be included in the prediction of the prone location of plaque development in curved blood vessels.

Moreover, it is known that the most drastic complication of atherosclerosis occurs when

plaque ruptures, resulting in thrombosis. When the two-layer viscous fluids in a straight tube model is considered, it shows that thin film rupture preferentially tends to occur in areas with locally high local pressure. This thin film rupture can be prevented by either large surface tension or low frequencies of pressure gradients of the upper fluids, *i.e.* when either the effects of surface tension on a fibrous cap is strong or low frequencies of blood pressure are imposed, these can resist the plaque vulnerability and ultimately plaque rupture.

There are other mechanisms which can have significant effects on flows in the vicinity of atherosclerotic lesion. For example, the Marangoni flow model and the moving contact line problem describing lesion adhesion can be used to explain mass transfer flux from atherogenic constituents of plaque to blood stream. These can be addressed for future research.

## 6.2 Further work

In this section we will consider some possible directions in the further investigation of blood flows in both straight and curved vessels when atherosclerotic plaques are present.

- In chapter 5, we treated plaque as a thin viscous film. In reality, plaque has usually asymmetric geometry, with a rough, irregular surface. For simplicity, the stenosis geometry can be represented by a smooth mathematical function, and the cosine curve is commonly used Yakhot et al. (2005), *viz*

$$r(x) = \begin{cases} H - \frac{d}{2}[1 + \cos(\pi(x - x_1)/x_0)], & |x - x_1| \leq x_0 \\ H & \text{otherwise,} \end{cases} \tag{6.1}$$

  where $r(x)$ is the radius of a vessel in the stenotic region, $H$ is the radius of the vessel in the nonstenotic region, $x_1$ is the centre of the stenosis, and $x_0$ is the half length, see Figure 6.1.

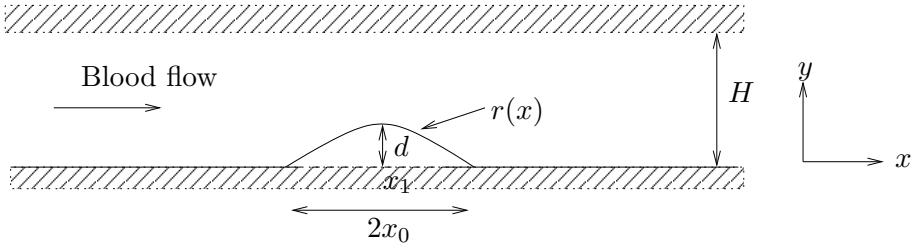



Figure 6.1: The geometry of a plaque in a stright rigid vessel.

  The unsteady, pulsatile nature of the flowing blood would be addressed. The change of hemodynamic factors, such as velocity, shear stress and pressure, may lead to the development and progression of plaque downstream of the original stenotic region.
- We can extend the previous model by considering flow in a stenosed, curved tube. This model would be able to predict the main characteristics of the physiological flows because plaques are usually found in curved and bifurcating regions. Several flow characteristics, such as wall shear stress, in-plaque flow, velocity and turbulence are expected to become more severe when the degree of stenosis is high for both models.
- Blood is normally treated as an incompressible Newtonian fluid. Nevertheless, in small vessels, blood behaves as a non-Newtonian fluid at low shear rate because the

characteristics of the red cells become dominant and exhibits shear thinning behaviour (James et al., 2005). The deformability of the arterial wall may also contribute to the blood flow behaviour.

Mathematical models are essential because they offer an alternative and non-invasive tool for obtaining realistic descriptions of complicated flows. The capability of describing the flow through constricted vessels in its early stage may be helpful in the development of diagnostic tools for the detecting of the onset of the disease before it becomes life-threatening.

# Appendix A

# MATLAB code for the two-layer thin-film model in Chapter 5.

```
function [x,t,h,m] = thinfilmkayoscillating
% Solves h_t + (a(h)(b(h,x)+h_xx)_x+c(h,x))_x = 0 on [0,L]
% BCs: h_x = a(h)(b(h,x)+h_xx)_x+c(h,x) = 0 at x = 0, L
% To run enter "[x,t,h,m] = thinfilmkay;"
% If positivity is lost, the integration should terminate.
%Written by James Oliver


%%%%%%%%%%%%%%%%%%%%%%%%%%%%%%%%%%%%%%%%%%%%%%%%%%%%%%%%%%%%%%%%%%%%%%%%%%%%%%%
% Grid definition
%%%%%%%%%%%%%%%%%%%%%%%%%%%%%%%%%%%%%%%%%%%%%%%%%%%%%%%%%%%%%%%%%%%%%%%%%%%%%%%

L       = 1;                % Domain length
N       = 1000;             % x-grid points
dx      = L/N;              % x-grid spacing
x       = dx*((1:N)-0.5)';  % Half-grid points
T       = 1.57;                % Maximum time
M       = 101;              % Output points t
tspan  = linspace(0,T,M);  % t-grid points
t1      = min(tspan);       % Initialize time tracking

%%%%%%%%%%%%%%%%%%%%%%%%%%%%%%%%%%%%%%%%%%%%%%%%%%%%%%%%%%%%%%%%%%%%%%%%%%%%%%%
% End grid definition
%%%%%%%%%%%%%%%%%%%%%%%%%%%%%%%%%%%%%%%%%%%%%%%%%%%%%%%%%%%%%%%%%%%%%%%%%%%%%%%


%%%%%%%%%%%%%%%%%%%%%%%%%%%%%%%%%%%%%%%%%%%%%%%%%%%%%%%%%%%%%%%%%%%%%%%%%%%%%%%
% Function handles (user defined)
%%%%%%%%%%%%%%%%%%%%%%%%%%%%%%%%%%%%%%%%%%%%%%%%%%%%%%%%%%%%%%%%%%%%%%%%%%%%%%%

Gamma = 1.0;
```

```
Mt   = 10;
fre   = 1 ;

a  = @(u,v) 2*Gamma/3*(u.*v).^2./(u+v);
b  = @(u)   0.*u;
c  = @(u,t) Mt*sin(fre*pi*t)*(u.^2)./4;

%%%%%%%%%%%%%%%%%%%%%%%%%%%%%%%%%%%%%%%%%%%%%%%%%%%%%%%%%%%%%%%%%%%%%%%%%%%%%%%
% End function handles
%%%%%%%%%%%%%%%%%%%%%%%%%%%%%%%%%%%%%%%%%%%%%%%%%%%%%%%%%%%%%%%%%%%%%%%%%%%%%%%


%%%%%%%%%%%%%%%%%%%%%%%%%%%%%%%%%%%%%%%%%%%%%%%%%%%%%%%%%%%%%%%%%%%%%%%%%%%%%%%
% Initial conditions
%%%%%%%%%%%%%%%%%%%%%%%%%%%%%%%%%%%%%%%%%%%%%%%%%%%%%%%%%%%%%%%%%%%%%%%%%%%%%%%
IA = 0.1;
IF = 1*pi;
v0      = 1.0+IA*sin(IF*x);

%%%%%%%%%%%%%%%%%%%%%%%%%%%%%%%%%%%%%%%%%%%%%%%%%%%%%%%%%%%%%%%%%%%%%%%%%%%%%%%
% End initial conditions
%%%%%%%%%%%%%%%%%%%%%%%%%%%%%%%%%%%%%%%%%%%%%%%%%%%%%%%%%%%%%%%%%%%%%%%%%%%%%%%


%%%%%%%%%%%%%%%%%%%%%%%%%%%%%%%%%%%%%%%%%%%%%%%%%%%%%%%%%%%%%%%%%%%%%%%%%%%%%%%
% Solution
%%%%%%%%%%%%%%%%%%%%%%%%%%%%%%%%%%%%%%%%%%%%%%%%%%%%%%%%%%%%%%%%%%%%%%%%%%%%%%%

options = odeset('RelTol',1e-6,'AbsTol',1e-6,'Stats','on',...
                 'JPattern',jpattern(N),'Events',@events);
disp('Using ode15s to time step.')
tic
[t,h,TE,YE,IE]   = ode15s(@f,tspan,v0,options);
toc

%%%%%%%%%%%%%%%%%%%%%%%%%%%%%%%%%%%%%%%%%%%%%%%%%%%%%%%%%%%%%%%%%%%%%%%%%%%%%%%
% End solution
%%%%%%%%%%%%%%%%%%%%%%%%%%%%%%%%%%%%%%%%%%%%%%%%%%%%%%%%%%%%%%%%%%%%%%%%%%%%%%%


%%%%%%%%%%%%%%%%%%%%%%%%%%%%%%%%%%%%%%%%%%%%%%%%%%%%%%%%%%%%%%%%%%%%%%%%%%%%%%%
% Report positivity & mass loss
%%%%%%%%%%%%%%%%%%%%%%%%%%%%%%%%%%%%%%%%%%%%%%%%%%%%%%%%%%%%%%%%%%%%%%%%%%%%%%%

if (numel(TE)>0)
    disp(['Positivity lost at x = ',num2str(x(IE(1))), ...
                          ' at t = ',num2str(TE(1)),'.'])
else
```

```
    disp('Solution remains positive.')
end

m   = sum(h,2)*(x(2)-x(1));
PML = 100*(abs(m(1)-m))/m(1);
disp(['Maximum mass loss = ',num2str(max(PML)),' percent.'])
disp('Plot using e.g. "surf(x,t,h); shading interp."')

figure(1)
set(gcf,'Color','w');
surf(x,t,h);
shading interp;
xlabel('x','FontSize',14)
ylabel('t','FontSize',14)
zlabel('h(x,t)','FontSize',14)
view([0 90])
colorbar


%plot(x,h(1,:),'red',x,h(50,:),'green',x,h(101,:),'blue')
%grid on


%%%%%%%%%%%%%%%%%%%%%%%%%%%%%%%%%%%%%%%%%%%%%%%%%%%%%%%%%%%%%%%%%%%%%%%%%%%%%%%
% End report positivity & mass loss
%%%%%%%%%%%%%%%%%%%%%%%%%%%%%%%%%%%%%%%%%%%%%%%%%%%%%%%%%%%%%%%%%%%%%%%%%%%%%%%


%%%%%%%%%%%%%%%%%%%%%%%%%%%%%%%%%%%%%%%%%%%%%%%%%%%%%%%%%%%%%%%%%%%%%%%%%%%%%%%
% Nested function f
%%%%%%%%%%%%%%%%%%%%%%%%%%%%%%%%%%%%%%%%%%%%%%%%%%%%%%%%%%%%%%%%%%%%%%%%%%%%%%%

function dudt = f(t,v)
% Print time to screen
if (t>t1)
    t1=t;
    disp(['t = ',num2str(t1)]);
else
end
% Extract data & apply boundary conditions
u          = zeros(N+2,1);
u(2:N+1)   = v(1:N);
u([1,N+2]) = 2-u([2,N+1]);
% Functions used at least twice
A          = zeros(N+1,1);
A(2:N)     = a(u(2:N),u(3:N+1));
B          = zeros(N+1,1);
B(2:N+1)   = b(u(2:N+1));
```

```
C          = zeros(N+2,1);
C(2:N+1)   = c(u(2:N+1),t);
Q    = zeros(N+1,1);
Q(2:N)    = A(2:N).*((B(3:N+1)-B(2:N))/dx ...
            +(u(4:N+2)-3*u(3:N+1)+3*u(2:N)-u(1:N-1))/dx^3) ...
            +(C(2:N)+C(3:N+1))/2;
% Flux
dudt    = (Q(1:N)-Q(2:N+1))/dx;
end

%%%%%%%%%%%%%%%%%%%%%%%%%%%%%%%%%%%%%%%%%%%%%%%%%%%%%%%%%%%%%%%%%%%%%%%%%%%%
% End nested function f
%%%%%%%%%%%%%%%%%%%%%%%%%%%%%%%%%%%%%%%%%%%%%%%%%%%%%%%%%%%%%%%%%%%%%%%%%%%%



%%%%%%%%%%%%%%%%%%%%%%%%%%%%%%%%%%%%%%%%%%%%%%%%%%%%%%%%%%%%%%%%%%%%%%%%%%%%
% Sparsity pattern S
%%%%%%%%%%%%%%%%%%%%%%%%%%%%%%%%%%%%%%%%%%%%%%%%%%%%%%%%%%%%%%%%%%%%%%%%%%%%
% To use uncomment and replace options with e.g.
% options = odeset('RelTol',1e-6,'AbsTol',1e-12,'Stats','on',...
%                  'JPattern',jpattern(N));
%%%%/%%%%%%%%%%%%%%%%%%%%%%%%%%%%%%%%%%%%%%%%%%%%%%%%%%%%%%%%%%%%%%%%%%%%%%%

function S = jpattern(N)
  S0 = ones(N,1);
  S  = spdiags([S0 S0 S0 S0 S0], -2:2, N, N);
end

%%%%%%%%%%%%%%%%%%%%%%%%%%%%%%%%%%%%%%%%%%%%%%%%%%%%%%%%%%%%%%%%%%%%%%%%%%%%
% End sparsity pattern S
%%%%%%%%%%%%%%%%%%%%%%%%%%%%%%%%%%%%%%%%%%%%%%%%%%%%%%%%%%%%%%%%%%%%%%%%%%%%



%%%%%%%%%%%%%%%%%%%%%%%%%%%%%%%%%%%%%%%%%%%%%%%%%%%%%%%%%%%%%%%%%%%%%%%%%%%%
% Event function
%%%%%%%%%%%%%%%%%%%%%%%%%%%%%%%%%%%%%%%%%%%%%%%%%%%%%%%%%%%%%%%%%%%%%%%%%%%%

function [value,isterminal,direction] = events(t,u)
% Locate the time when height passes through zero in a
% decreasing direction and stop integration.
value      = u;          % Detect height = 0
isterminal = ones(N,1);  % Stop the integration
direction  = -ones(N,1); % Negative direction only
end

%%%%%%%%%%%%%%%%%%%%%%%%%%%%%%%%%%%%%%%%%%%%%%%%%%%%%%%%%%%%%%%%%%%%%%%%%%%%
% End event function
```

```
%%%%%%%%%%%%%%%%%%%%%%%%%%%%%%%%%%%%%%%%%%%%%%%%%%%%%%%%%%%%%%%%%%%%%%%%%%%%

end                 % End main function
```

# Appendix B

# MATLAB code for the inviscid Burgers equation.

```
%%%%%%%%%%%%%%%%%%%%%%%%%%%%%%%%%%%%%%%%%%%%%%%%%%%%%%%%%%%%%%%%%%%%%%%%
%When Gamma=0, the equation is reduced to the inviscid burgers equation
%dh/dt+(M/4)d(F)/dx = 0, where F=0.5(h^2)
%Initial condition: h(x,0)=1+0.1sin(pi*x)
%boundary condition: u(0,t) = 1 (only one boundary condition is applied)
%Scheme: Lax-Wendroff method
%Written by Nawinda Chutsagulprom
%%%%%%%%%%%%%%%%%%%%%%%%%%%%%%%%%%%%%%%%%%%%%%%%%%%%%%%%%%%%%%%%%%%%%%%%

%%%%%%%%%%%%%%%%%%%%%%%%%%%%%%%%%%%%%%%%%%%%%%%%%%%%%%%%%%%%%%%%%%%%%%%%
%Grid definition
%%%%%%%%%%%%%%%%%%%%%%%%%%%%%%%%%%%%%%%%%%%%%%%%%%%%%%%%%%%%%%%%%%%%%%%%
jmax =50;
dx = 1/jmax;
x = 0:dx:1;
N=0;
Nx=size(x);
dt=0.001;
t=0;
tfinish=1;
lambda = dt/dx;
%%%%%%%%%%%%%%%%%%%%%%%%%%%%%%%%%%%%%%%%%%%%%%%%%%%%%%%%%%%%%%%%%%%%%%%%
%End grid definition
%%%%%%%%%%%%%%%%%%%%%%%%%%%%%%%%%%%%%%%%%%%%%%%%%%%%%%%%%%%%%%%%%%%%%%%%


%%%%%%%%%%%%%%%%%%%%%%%%%%%%%%%%%%%%%%%%%%%%%%%%%%%%%%%%%%%%%%%%%%%%%%%%
%Matrix definition
%%%%%%%%%%%%%%%%%%%%%%%%%%%%%%%%%%%%%%%%%%%%%%%%%%%%%%%%%%%%%%%%%%%%%%%%
A = zeros(Nx(2),Nx(2));
for i=2:Nx(2)-1
```

```
    A(i,i-1) = -0.5;
    A(i,i+1) = 0.5;
end

B = zeros(Nx(2),Nx(2));
for i=2:Nx(2)-1
    B(i,i+1) = 0.5;
    B(i,i) = 0.5;
end

C = zeros(Nx(2),Nx(2));
for i=2:Nx(2)-1
    C(i,i) = -1;
    C(i,i+1) = 1;
end

D = zeros(Nx(2),Nx(2));
for i=2:Nx(2)
    D(i,i) = 0.5;
    D(i,i-1) = 0.5;
end

E = zeros(Nx(2),Nx(2));
for i=2:Nx(2)
    E(i,i) = 1;
    E(i,i-1) = -1;
end
%%%%%%%%%%%%%%%%%%%%%%%%%%%%%%%%%%%%%%%%%%%%%%%%%%%%%%%%%%%%%%%%%%%%%%%
%End matrix definition
%%%%%%%%%%%%%%%%%%%%%%%%%%%%%%%%%%%%%%%%%%%%%%%%%%%%%%%%%%%%%%%%%%%%%%%




%%%%%%%%%%%%%%%%%%%%%%%%%%%%%%%%%%%%%%%%%%%%%%%%%%%%%%%%%%%%%%%%%%%%%%%
%Initial condition
%%%%%%%%%%%%%%%%%%%%%%%%%%%%%%%%%%%%%%%%%%%%%%%%%%%%%%%%%%%%%%%%%%%%%%%
u=ones(size(x))+0.1*sin(pi*x);

%%%%%%%%%%%%%%%%%%%%%%%%%%%%%%%%%%%%%%%%%%%%%%%%%%%%%%%%%%%%%%%%%%%%%%%
%End initial condition
%%%%%%%%%%%%%%%%%%%%%%%%%%%%%%%%%%%%%%%%%%%%%%%%%%%%%%%%%%%%%%%%%%%%%%%



%%%%%%%%%%%%%%%%%%%%%%%%%%%%%%%%%%%%%%%%%%%%%%%%%%%%%%%%%%%%%%%%%%%%%%%
%Solution and plot
%%%%%%%%%%%%%%%%%%%%%%%%%%%%%%%%%%%%%%%%%%%%%%%%%%%%%%%%%%%%%%%%%%%%%%%
while(t<tfinish)
```

```
    f_u = (u.^2)./2;
        u = u-lambda*(A*f_u')'+0.5*lambda*lambda*(((B*u').*(C*f_u'))'-((D*u').*(E*f_u'))
    u(1) = 1;

  hold on
    if (mod(N,250)==0)
        N
        plot(x,u)
        grid on
    end
    t=t+dt;
    N=N+1;
end
%%%%%%%%%%%%%%%%%%%%%%%%%%%%%%%%%%%%%%%%%%%%%%%%%%%%%%%%%%%%%%%%%%%%%%%%%%%
%End solution
%%%%%%%%%%%%%%%%%%%%%%%%%%%%%%%%%%%%%%%%%%%%%%%%%%%%%%%%%%%%%%%%%%%%%%%%%%%
```

# Appendix C

# MATLAB code for the steady-state solutions in Chapter 5.

```
%%%%%%%%%%%%%%%%%%%%%%%%%%%%%%%%%%%%%%%%%%%%%%%%%%%%%%%%%%%%%%%%%%%%%%%%%%%%%%%%
%Steady state solutions
%Gamma/3*(f_x f_xxxx)+M/4 =0 on [0,1]
%BCs: f_x(0)=f_x(1)=1.
%By a mass conservation, f(1)-f(0)=m, m=constant, so setting f(0)=0 and f(1) = m.
%Written by Nawinda Chutsagulprom
%%%%%%%%%%%%%%%%%%%%%%%%%%%%%%%%%%%%%%%%%%%%%%%%%%%%%%%%%%%%%%%%%%%%%%%%%%%%%%%%


%%%%%%%%%%%%%%%%%%%%%%%%%%%%%%%%%%%%%%%%%%%%%%%%%%%%%%%%%%%%%%%%%%%%%%%%%%%%%%%%
%Solution
%%%%%%%%%%%%%%%%%%%%%%%%%%%%%%%%%%%%%%%%%%%%%%%%%%%%%%%%%%%%%%%%%%%%%%%%%%%%%%%%
function sol=mat4ode
jmax  = 1000;
Ma    = 10;
Gamma = 1;
m     = 1.065;
solinit=bvpinit(linspace(0,1,jmax), @mat4init);
sol=bvp4c(@mat4,@mat4bc,solinit);
plot(sol.x,sol.y(2,:),'blue')
xlabel('x','FontSize',12)
ylabel('h(x)')
grid on
hold on



%%%%%%%%%%%%%%%%%%%%%%%%%%%%%%%%%%%%%%%%%%%%%%%%%%%%%%%%%%%%%%%%%%%%%%%%%%%%%%%%
%End solution
```

```
%%%
```

# Bibliography


Adler, M. (1934). Strömung in gekrümmten rohren. *Z. angew. Math. Mech.*, *5*, 257–275.

Afsar-Siddiqui, A. B., Luckham, P. F., & Matar, O. K. (2003). The spreading of surfactant solutions on thin liquid films. *Adv. Colloid Interface Sci.*, *106*(1-3), 183–236.

Austin, L., & Seader, J. (1973). Fully developed viscous flow in coiled circular pipes. *AIChE J.*, *19*(1), 85–94.

Belloni, F. L. (1999). Teaching the principles of hemodynamics. *Advan. Physiol. Edu.*, *277*(6), 187–202.

Benjamin, T. (1978). Bifurcation phenomena in steady flows of a viscous fluid. I. Theory. *Proc. R. Soc. Lond. A*, *359*(1696), 1–26.

Berger, S. A., Talbot, L., & Yao, L. S. (1983). Flow in curved pipes. *Ann. Rev. Fluid Mech.*, *15*(1), 461–512.

Blennerhassett, P. (1976). *Secondary motion and diffusion in unsteady flow in a curved pipe*. Ph.D. thesis, Imperial College, London.

Borgas, M. S., & Grotberg, J. B. (1988). Monolayer flow on a thin film. *J.Fluid Mech.*, *193*(1), 151–170.

Braun, R., & Fitt, A. (2003). Modelling drainage of the precorneal tear film after a blink. *Math. Med. Biol.*, *20*(1), 1–28.

Brown, D. (2002). *Cardiovascular plaque rupture*. Marcel Dekker Inc, 1 ed.

Brown, S., Miller, W., & Eason, J. (2006). *Exercise Physiology: Basis of Human Movement in Health and Disease*. Lippincott Williams & Wilkins, 1 ed.

Bui, Q., Prempeh, M., & Wilensky, R. (2009). Atherosclerotic plaque development. *Int J Biochem Cell Biol*, *41*(11), 2109–13.

Caro, C., Fitz-Gerald, J., & Schroter, R. (1971). Atheroma and Arterial Wall Shear Observation, Correlation and Proposal of a Shear Dependent Mass Transfer Mechanism for Atherogenesis. *Proc. R. Soc. Lond.*, *177*(46), 109–133.

Clark, L. V. (2004). *Trends in atherosclerosis research*. Nova Biomedical Books, 1 ed.

Cliff, W. (1976). *Blood vessels*. Cambridge University Press, 1 ed.

Collins, W. M., & Dennis, S. C. R. (1975). The steady motion of a viscous fluid in a curved tube. *Q. J. Mech. Appl. Math.*, *28*(2), 133–156.

Craster, R., & Matar, O. (2006). On the dynamics of liquid lenses. *J. Colloid Interface Sci.*, *303*(2), 503–516.

Daskopoulos, P., & Lenhoff, A. M. (1989). Flow in curved ducts: bifurcation structure for stationary ducts. *J. Fluid Mech.*, *203*(1), 125–148.

Davies, M. (1998). Coronary artery remodelling and the assessment of stenosis by pathologists. *Histopathology*, *33*(6), 497–500.

de Gennes, P. G. (1985). Wetting: statics and dynamics. *Rev. Mod. Phys.*, *57*(3), 827–863.

Dean, W. (1928). The streamline motion of fluid in a curved pipe. *Phil Mag.*, *7*, 673–695.

Dennis, S. C. R., & NG, M. (1982). Dual solutions for steady laminar flow through a curved tube. *Q. J. Mech. Appl. Math.*, *35*(3), 305–324.

Dussan V., E. B. (1976). The moving contact line: the slip boundary condition. *J. Fluid Mech.*, *77*(4), 665–684.

Eckardstein, A. (2004). *Atherosclerosis: Diet and Drugs*. Springer, 1 ed.

Fuster, V., Alexander, R., O'Rourke, R., Roberts, R., King, S., & Prystowsky, E. (2004). *Hurst's the heart*. McGraw-Hill Professional, 11 ed.

Gauglitz, P., & Radke, C. (1988). An extended evolution equation for liquid film brea-up in cylindrical capillaries. *Chem. Eng. Sci.*, *43*(7), 1457–1465.

Gaver, D. P., & Grotberg, J. B. (1990). The dynamics of a localized surfactant on a thin film. *J. Fluid Mech.*, *213*(1), 127–148.

Gaver, D. P., & Grotberg, J. B. (1992). Droplet spreading on a thin viscous film. *J. Fluid Mech.*, *235*, 399–414.

Gennes, P., Hua, X., & Levinson, P. (1990). Dynamics of wetting: local contact angles. *J. Fluid Mech.*, *212*, 55–63.

Goren, S. L. (1962). The instability of an annular thread of fluid. *J. Fluid Mech.*, *12*(02), 309–319.

Greenspan, D. (1973). Secondary flow in a curved tube. *J. Fluid Mech.*, *57*, 167–176.

Greenspan, H. P. (1978). On the motion of a small viscous droplet that wets a surface. *J. Fluid Mech.*, *84*(01), 125–143.

Grotberg, J. B., & Jensen, O. E. (2004). Biofluid mechanics in flexible tubes. *Ann. Rev. Fluid Mech.*, *36*(1), 121–147.

Halpern, D., & Grotberg, J. B. (1992a). Dynamics and transport of a localized soluble surfactant on a thin film. *J. Fluid Mech.*, *237*, 1–11.

Halpern, D., & Grotberg, J. B. (1992b). Fluid-elastic instabilities of liquid-lined flexible tubes. *J. Fluid Mech.*, *244*, 615–632.

Hammond, P. S. (1983). Nonlinear adjustment of a thin annular film of viscous fluid surrounding a thread of another within a circular cylindrical pipe. *J. Fluid Mech.*, *137*, 363–384.

Hirose, M., Kobayashi, Y., Mintz, G. S., Moussa, I., Mehran, R., Lansky, A. J., Dangas, G., Kreps, E. M., Collins, M. B., Stone, G. W., Colombo, A., Leon, M. B., & Moses, J. W. (2003). Correlation of coronary arterial remodeling determined by intravascular ultrasound with angiographic diameter reduction of 20 % to 60%. *Am. J. Cardiol.*, *92*(2), 141–145.

Hocking, L. M. (1981). Sliding and spreading of thin two-dimensional drops. *Q. J. Mech. Appl. Math.*, *34*(1), 37–55.

Holmberg, K., Jönsson, B., Kronberg, B., & lindman, B. (2004). *Surfactants and polymers in aqueous solution*. John Wiley & Sons Ltd, 2 ed.

Holzapfel, G. A., & Ogden, R. W. (2003). *Biomechanics of soft tissue in cardiovascular systems, Volume 2001*. SpringerWienNewYork, 1 ed.

Howell, P. (1999). The draining of a two-dimensional bubles. *J. Engrg. Math.*, *35*, 251–272.

Howell, P. (2003). Surface-tension-driven flow on a moving curved surface. *J. Engrg. Math.*, *45*(3), 283–308.

Howison, S., Moriarty, J., Ockendon, J. R., Terrill, E., & Wilson, S. (1997). A mathematical model for drying paint layers. *J. Engrg. Math.*, *32*(4), 377–394.

Huh, C., & Scriven, L. (1971). Hydrodynamic model of the steady movement of a solid/liquid/fluid contact line. *J. Colloid Interface Sci.*, *35*(1), 85–101.

Ida, M. P., & Miksis, M. J. (1998). The dynamics of thin films i: General theory. *SIAM J Appl Math.*, *58*(2), 456–473.

Ito, H. (1987). Flow in curved pipes. *Japan. Soc. Mech. Engrs Intl J.*, *30*, 543–552.

James, S., Kish, P., & Sutton, T. (2005). *Principles of bloodstain pattern analysis: Theory and Practice*. Taylor & Francis, 1 ed.

Jensen, O. E. (1997). The thin liquid lining of a weakly curved cylindrical tube. *J. Fluid Mech.*, *331*(1), 373–403.

Junqueira, L., & Carneiro, J. (2005). *Basic histology: text & atlas*. The McGraw-Hill Companies, 11 ed.

Kádár, A., & Glasz, T. (2001). Development of atherosclerosis and plaque biology. *Cardio. Surg.*, *9*(2), 109–121.

Kalliadasis, S., & Chang, H.-C. (1994). Drop formation during coating of vertical fibres. *J. Fluid Mech.*, *261*(1), 135–168.

Katritsis, D., Kaiktsis, L., Chaniotis, A., Pantos, J., Efstathopoulos, E. P., & Marmarelis, V. (2007). Wall shear stress: Theoretical considerations and methods of measurement. *Progr Cardiovasc Dis.*, *49*(5), 307–329.

Kavehpour, H. P., Ovryn, B., & McKinley, G. H. (2003). Microscopic and macroscopic structure of the precursor layer in spreading viscous drops. *Phys. Rev. Lett.*, *91*(19), 1–4.

Klabude, R. (2004). *Cardiovascular Physiology concepts*. Lippincott Williams and Wilkins, 1 ed.

Ku, D. N., Giddens, D. P., K., Z. C., & Glagov, S. (1985). Pulsatile flow and atherosclerosis in the human carotid bifurcation. Positive correlation between plaque location and low oscillating shear stress. *Arteriosclerosis*, *5*(3), 293–302.

Lehoux, S., & Tedgui, A. (2003). Cellular mechanics and gene expression in blood vessels. *J. Biomech.*, *36*(5), 631 – 643.

Leveque, R. J. (2002). *Finite volume methods for hyperbolic problems*. Cambridge University Press, 1 ed.

Levy, B. (1999). *Biology of the arterial wall*. Kluwer Academic, 1 ed.

Libby, P., Geng, Y. J., Aikawa, M., Schoenbeck, U., Mach, F., Clinton, S. K., Sukhova, G. K., & Lee, R. T. (1996). Macrophages and atherosclerotic plaque stability. *Current Opinion in Lipidology*, *7*(5), 330–335.

Lister, J., Rallion, J., King, A., Cummings, L., & Jensen, O. (2006). Capillary drainage of an annular film: the dynamics of collars and lobes. *J. Fluid Mech.*, *552*, 311–343.

Lyne, W. H. (1971). Unsteady viscous flow in a curved pipe. *J. Fluid Mech.*, *45*(1), 13–31.

Mackman, N. (2004). Role of tissue factor in hemostasis, thrombosis, and vascular development. *Arterioscler Thromb Vasc Biol.*, *24*(6), 1015–1022.

Malek, A. M., Alper, S. L., & Izumo, S. (1999). Hemodynamic shear stress and its role in atherosclerosis. *JAMA*, *282*(21), 2035–2042.

Marieb, E., & Hoehn, K. (2006). *Human anatomy and physiology*. Benjamin-Cummings, 7 ed.

McConalogue, D. J., & Srivastava, R. S. (1968). Motion of a fluid in a curved tube. *Proc. R. Soc. Lond. A*, *307*(1488), 37–53.

Miller, T. (2006). *Modern surgical care: physiologic foundations and clinical*. Informa Healthcare USA, 3 ed.

Mori, Y., & Nakayama, W. (1965). Study on forced convective heat transfer in curved pipes(1st report, laminar region). *Int. J. Heat Mass Trans.*, *8*, 67–82.

Moriarty, J. A., & Grotberg, J. B. (1999). Flow-induced instabilities of a mucus-serous bilayer. *J. Fluid Mech.*, *397*(1), 1–22.

Mullin, T., & Greated, C. A. (1980). Oscillatory flow in curved pipes. part 2. the fully developed case. *J. Fluid Mech.*, *98*(2), 397–416.

Myers, T. G. (1998). Thin films with high surface tension. *SIAM J. Appl Math.*, *40*(3), 441–462.

NHS (2009). Coronary heart disease.
URL `http://www.nhs.uk/conditions/coronary-heart-disease/Pages/Introduction.aspx`

Ockendon, H., & Ockendon, J. (1995). *Viscous Flow*. Cambridge University Press, 1 ed.

Oron, A., Davis, S. H., & Bankoff, S. G. (1997). Long-scale evolution of thin liquid films. *Rev. Mod. Phys.*, *69*(3), 931–980.

Pasterkamp, G., Falk, E., Woutman, H., & Borst, C. (2000). Techniques characterizing the coronary atherosclerotic plaque: influence on clinical decision making? *J. Am Coll Cardiol.*, *36*(1), 13–21.

Paszkowiak, J. J., & Dardik, A. (2003). Arterial wall shear stress: observations from the bench to the bedside. *37*, 47–57.

Pedley, T. (1980). *The fluid mechanics of large blood vessels*. Cambridge University Press, 1 ed.

Peterson, L. H., Jensen, R. E., & Parnell, J. (1960). Mechanical properties of arteries in vivo. *Circ. Res.*, *8*(3), 622–639.

Porth, C. (2006). *Essentials of pathophysiology: concepts of altered health states*. Lippincott Williams and Wilkins, 2 ed.

Premkumar, K. (2003). *The massage connection: Anatomy & Physiology*. Lippincott Williams & Wilkins, 2 ed.

Quéré, D. (1990). Thin films flowing on vertical fibres. *Europhys. Lett.*, *13*, 721–726.

Roberts, A. J., & Li, Z. (2006). An accurate and comprehensive model of thin fluid flows with inertia on curved substrates. *J. Fluid Mech.*, *553*(1), 33–73.

Roy, R., Roberts, A. J., & Simpson, M. E. (2002). A lubrication model of coating flows over a curved substrate in space. *J. Fluid Mech.*, *454*(1), 235–261.

Schwartz, L., & Weidner, D. (1995). Modeling of coating flows on curved surfaces. *J. Engrg. Math.*, *29*(1), 91–103.

Selvadurai, A. (2000). *Partial Differential Equations in Mechanics 1: Fundamentals, Laplace's Equation, Diffusion Equation, Wave Equation*. Springer, 1 ed.

Shaaban, A. M., & Duerinckx, A. J. (2000). Wall shear stress and early atherosclerosis: A review. *Am. J. Roentgenol.*, *174*(6), 1657–1665.

Sherwood, L. (2003). *Human Physiology: From cells to systems*. Brooks Cole, 5 ed.

Shikhmurzaev, Y. (2006). Singularities at the moving contact line. mathematical, physical and computational aspects. *Physica D*, *217*(2), 121–133.

Siggers, J., & Waters, S. (2005). Steady flows in pipes with finite curvature. *Phys. Fluids.*, *17*(7), 1–18.

Siggers, J. H., & Waters, S. L. (2008). Unsteady flows in pipes with finite curvature. *J. Fluid Mech.*, *600*(1), 133–165.

Smith, F. T. (1975). Pulsatile flow in curved pipes. *J. Fluid Mech.*, *71*(1), 15–42.

Smoller, J. (1994). *Shock waves and reaction-diffusion equations*. Springer, 2 ed.

Stary, H. C., Blankenhorn, D. H., Chandler, A. B., Glagov, S., Insull, J. r., W, Richardson, M., Rosenfeld, M. E., Schaffer, S. A., Schwartz, C. J., & Wagner, W. D. (1992). A definition of the intima of human arteries and of its atherosclerosis- prone regions. A report from the committee on vascular lesions of the council on arteriosclerosis, American Heart Association. *Circulation*, *85*(1), 391–405.

Stockley, R., Rennard, S., Rabe, K., & B.Celli (2007). *Chronic obstructive pulmonary disease*. Blackwell Publishing, 1 ed.

Tannehill, J., Anderson, D., & Pletcher, R. (1997). *Computational fluid mechanics and heat transfer*. Taylor & Francis Ltd., 2 ed.

Thim, T., Hagensen, M. K., Bentzon, J. F., & Falk, E. (2008). From vulnerable plaque to atherothrombosis. *J. Intern Med.*, *263*(5), 506–516.

Thomson, J. (1877). Experimental demonstration in respect to the origin of windings of rivers in alluvial plains, and to the mode of flow of water round bends of pipes. *Proc. R. soc. London Ser. A.*, *26*, 356–357.

Toschi, V., Gallo, R., Lettino, M., Fallon, J. T., Gertz, S. D., Fernandez-Ortiz, A., Chesebro, J. H., Badimon, L., Nemerson, Y., Fuster, V., & Badimon, J. J. (1997). Tissue factor modulates the thrombogenicity of human atherosclerotic plaques. *Circulation*, *95*(3), 594–599.

Truesdell, L. C., & Adler, R. J. (1970). Numerical treatment of fully developed laminar flow in helically coiled tubes. *AIChE J.*, *16*(6), 1010–1015.

Vallance, P., & Webb, D. (2000). *Vascular endothelium in human physiology and pathophysiology*. Harwood academic, 1 ed.

Van De Fliert, B. W., Howell, P. D., & Ockenden, J. R. (1995). Pressure-driven flow of a thin viscous sheet. *J. Fluid Mech.*, *292*(1), 359–376.

Van Dyke, M. (1978). Extended stokes series: laminar flow through a loosely coiled pipe. *J. Fluid Mech.*, *86*(1), 129–145.

Varnava, A. M., Mills, P. G., & Davies, M. J. (2002). Relationship Between Coronary Artery Remodeling and Plaque Vulnerability. *Circulation*, *105*(8), 939–943.

Voelker, R. (1998). Plaque rupture vs erosion. *JAMA*, *279*(20), 1599.

Ward, M. R., Pasterkamp, G., Yeung, A. C., & Borst, C. (2000). Arterial Remodeling : Mechanisms and Clinical Implications. *Circulation*, *102*(10), 1186–1191.

Warrell, D., Cox, T., & Firth, J. (2005). *Oxford textbook of medicine, Volume 3*. Oxford University Press, 4 ed.

Warsi, Z. (2006). *Fluid Dynamics: Theoretical and Computational Approaches*. Taylor & Francis, 1 ed.

Waters, S. (2007). Physiological flow patterns and their significance: Lecture note.

White, C. M. (1929). Streamline flow through curved pipes. *Proc. R. Soc. Lond. A*, *123*(792), 645–663.

Yakhot, A., Grinberg, L., & Nikitin, N. (2005). Modeling rough stenoses by an immersed-boundary method. *J. Biomech.*, *38*(5), 1115–1127.

Yanase, S., Goto, N., & Yamamoto, K. (1989). Dual solutions of the flow through a curved tube. *Fluid Dyn. Res.*, *5*(3), 191–201.

Zalosh, R. G., & Nelson, W. G. (1973). Pulsating flow in a curved tube. *J. Fluid Mech.*, *59*(4), 693–705.

Zaman, A. G., Helft, G., Worthley, S. G., & Badimon, J. J. (2000). The role of plaque rupture and thrombosis in coronary artery disease. *Atherosclerosis*, *149*(2), 251 – 266.

Zhornitskaya, L., & Bertozzi, A. L. (2000). Positivity-preserving numerical schemes for lubrication-type equations. *SIAM J. Numer. Anal.*, *37*(2), 523–555.